Luminescent Properties of Synthesized PbS Nanoparticle Phosphors

by

Mokhotjwa Simon Dhlamini
(MSc)

A thesis submitted in fulfillment of the requirements for the degree

PHILOSOPHIAE DOCTOR

in the

Faculty of Natural and Agricultural Sciences
Department of Physics

at the

University of the Free State

Promoter: Prof. H.C. Swart
Co-Promoter: Prof. J.J. Terblans

August 2008

Dedicated to the memory of the late

Phellemon Petrus Motaung

(1966 – 2004)

Acknowledgements

- I thank God for making impossible things possible for me to finish this study.
- I would like to express my deep and sincere gratitude to my promoter, *Prof. Hendrik C. Swart* for his guidance and support for the duration of the study. His wide knowledge and logical way of thinking have been of great value for me.
- I am grateful to my co-promoter, *Prof. J.J. Terblans* for his valuable advice in the characterization of the samples.
- I gratefully thank *Dr. Odireleng M. Ntwaeaborwa* for introducing me to nanoscience, and helping with preparation of the nanoparticle phosphors. Above all, I thank him for his advice in the organization of ideas.
- My heartfelt appreciation also goes to *Dr. James M. Ngaruiya* of Jomo Kenyatta University of Agriculture & Technology, Nairobi, Kenya, for his fruitful discussions and constructive comments in this research.
- I thank *Dr. R.E. Kroon* for helping me with the electron diffraction measurements and the analysis (pattern).
- I thank *Mr. H.D Joubert*, a PhD student in the department of Physics for helping me with least square fit for the removal of the SiO_2 background from the XRD spectrum.
- I thank all staff members and fellow students of the Department of Physics for their assistance and support.
- I owe my loving thanks to my wife *Thabang* and our daughter *Nonhlanhla.* They have lost a lot due to my research and without their encouragement and understanding it would have been impossible for me to finish this work. My special gratitude is due to my parents, brothers and sisters for their moral support.
- Many thanks to my former school teachers of *Metsimatsho Senior Secondary School* (*Thaba-bosiu*) for their inspiration and encouragement.
- I am grateful for the financial support from the *South African National Research Foundation, National Metrology Institute of South Africa, Council for Scientific and Industrial Research of South Africa* and the *University of the Free State.*

Abstract

Luminescent lead sulphide (PbS) nanoparticles embedded in an amorphous silica (SiO_2) matrix were synthesized at room temperature by a sol-gel process. The prepared nanocomposite materials were crushed into powders and annealed in air at 200°C. The chemical composition of the powders was analyzed with an energy dispersive x-ray spectrometer. Particle sizes, crystalline structure and morphology of the PbS nanoparticles were determined with transmission electron microscopy (TEM) and x-ray diffraction (XRD). The crystal particle sizes estimated from the XRD peaks and the TEM images were in the range of 10 to 50 nm in diameter.

The SiO_2:PbS powders were then irradiated with 325 nm (He-Cd) and 458 nm (Ar^+) lasers for photoluminescence (PL) measurement. PL spectra were obtained for pure SiO_2 as well as the encapsulated PbS nanoparticles at room temperature. Two strong broad bands, blue (450 nm) and yellow-orange (560 nm) from bulk SiO_2 and PbS nanoparticles, respectively, were observed. The PL data show a blue shift from the normal emission wavelength at ~ 3200 nm in bulk PbS to ~ 560 – 700 nm in nanoparticulate PbS powders. The blue-shift of the emission wavelengths is attributed to quantum confinement of charge carriers in the restricted volume of nanoparticles. Energy transfer from ZnO nanoparticles to PbS nanoparticles was also observed. The possible mechanism for the energy transfer is reported.

The powders were also subjected to prolonged 2 keV electron beam irradiation in a vacuum chamber at and different O_2 pressures ($5 \times 10^{-8} - 2 \times 10^{-7}$ Torr O_2). The cathodoluminescence (CL) was measured with Ocean Optics S2000 spectrometer, and showed the emission peak to be at a wavelength of 680 nm. Changes in the CL brightness and the corresponding change in the surface chemical composition were investigated with Ocean Optics S2000, Auger Electron Spectroscopy (AES) and X-ray Photoelectron Spectroscopy (XPS). The oxygen Auger peak-to-peak height decreased simultaneously with the CL intensity. XPS analysis on the degraded spot showed the development of characteristic SiO, SiO_x ($0<x<1$) and elemental silicon peaks on the low-energy side of the SiO_2 peak. The electron beam induced dissociation of SiO_2 into elemental silicon and oxygen resulted in oxygen desorbing from the surface at almost the same rate as the CL intensity was decreasing. The data suggest that a non-luminescent $PbSO_4$ was also formed on the surface. The degradation was less severe at higher oxygen pressures. All the measurements were done at room temperature.

Thin luminescent films of SiO_2:PbS were grown on Si(100) substrates at room temperature, 100°C, 200°C, 300°C and 400°C by the pulsed laser deposition (PLD) technique. Surface morphology and PL properties of samples were analyzed with scanning electron microscopy (SEM) and a 458 nm (Ar^+) laser respectively. The PL emission wavelength of the films was red-shifted from that of the powders at ~ 560 nm to ~ 660 nm. The PL emission of the films was less intense than that of the powders, although the intensity of some of the films was improved marginally by post-deposition annealing in air at 400°C. The increase in the PL intensity with an increase in the deposition temperatures was observed.

Key Words

Sol-gel, PbS nanoparticles, Cathodoluminescence, Degradation, Photoluminescence, Energy transfer

Acronyms

- CL – Cathodoluminescence
- AES – Auger electron spectroscopy
- APPHs – Auger peak-to-peak heights
- XPS – X-ray photoelectron spectroscopy
- XRD – X-ray diffraction
- TEM – Transmission electron microscopy
- SEM – Scanning electron microscopy
- EDS – Energy dispersive spectroscopy
- PLD – Pulsed laser deposition
- PL – Photoluminescence
- FED – Field emission display
- EtOH – Ethanol
- TEOS – Tetraethylorthosilicate
- QD – Quantum Dot

Table of Contents

Chapter 1: Introduction

Chapter 2: Semiconductor nanoparticles and thin films

Chapter 3: Experimental Research Techniques

Chapter 4: Sol - gel preparation of PbS nanoparticles incorporated in SiO_2 matrix

Chapter 5: Cathodoluminescence degradation of the SiO_2:PbS nanoparticulate powder phosphors

Chapter 6: Photoluminescence properties of SiO_2 surface passivated PbS nanoparticles

Chapter 7: Photoluminescence properties of powder and pulsed laser deposited PbS nanoparticles in SiO_2

Chapter 8: PbS concentration quenching in SiO_2 matrix and enhanced photoluminescence by an energy transfer from ZnO nanoparticles to PbS nanoparticles

Chapter 9: Summary and Conclusion

List of Figures

CHAPTER 1

INTRODUCTION

1.1. Background

Nanotechnology is defined as the creation and utilization of new materials, devices and systems at the molecular level – phenomena associated with atomic and molecular interactions. It is one of the interdisciplinary technologies which promise to have implications for health, wealth and peace in the upcoming decades [1,2]. It is also regarded as the meeting ground of the engineering, biology, physics, medicine and chemistry fields [3]. This technology is sought to be the primary driver of the 21st century and the new economy [1,2].

Knowledge in this new field of science is growing worldwide, leading to fundamental scientific advances. This will lead to dramatic changes in the ways that materials, devices, and systems are understood and created. Among the expected breakthroughs are an order of magnitude increase in computer efficiency, human organ restoration using engineered tissue, “designer” materials created from directed assembly of atoms and molecules and the emergence of entirely new phenomena in chemistry and physics [4]. Nanomaterials and most of the applications derived from them are still in an early stage of technical development. Much work still needs to be done in this newly born field of science.

Nanocrystalline materials are characterized by a microstructural length or grain size of up to 100 nm [5,6], and have distinctly different properties than bulk materials. The number of atoms or molecules on the surface of nanoparticle is comparable to that inside the particles, therefore nanoparticles can be used to develop materials with unique properties

[7]. It is reported that to meet the technological demands in the areas such as electronics, catalysis, ceramics magnetic data storage, structural components etc, the size of the materials should be reduced to the nanometer scale.

Recently, the synthesis of nanoparticles has become very important. Nanoparticles synthesized using different methods may have different internal structures that affect the properties of materials consolidated from them. One of the most critical characteristics of nanoparticles is their very high surface-to-volume ratio, i.e. large fractions of surface atoms. The large fractions of surface atoms together with ultra-fine size and shape effects make nanoparticles exhibit distinctly different properties from the bulk [5]. The percentage of surface atoms increases as the size of the nanoparticles is decreased. Controlling the size, shape and structure of nanoparticles is technologically important because of strong correlation between these parameters and optical, electrical, magnetic and catalytic properties [8,9].

In this study, attention is mainly focused to the nano-scaled phosphor particles. A phosphor is a luminescent material that emits light under some type of external stimulation which can be an electron beam or photons. They are usually in the form of powders but in some cases, thin films. The phosphor material can be doped intentionally with impurities to emit the desired wavelength of light. They are critical to the development and improvement of display technologies. The production of phosphor particles of smaller sizes is necessary for the realization of high resolution images, and therefore the development of phosphor fine particles with stronger emission intensities has been expected [10]. Phosphor particles of spherical morphology, submicrometer size, and narrow particle size distribution give higher particle packing densities than commercial products (3 – 5 μm in size) and are thus effective in the enhancement of luminescent efficiency [10]. Few investigations have been reported on luminescent properties of PbS nanoparticle phosphors synthesized by a sol-gel process. This method produces particles with a wide size and shape distribution.

PbS is a phosphor with a bulk band gap in the near infrared at 3200 nm (0.41 eV) [9,11,12,13]. Its emission and absorption lines are consequently broad, but by engineering its crystallite size, tunable emission can be obtained in a large spectral region ranging from the visible to the near infrared [9]. Strong luminescence was observed for PbS quantum dot (QD) doped glasses at the 1300 nm communications wavelength under pulsed laser excitation [14]. This observation has generated new interest in PbS QDs doped glasses as promising candidates compared to other materials for communications applications. Yang *et al.* [15] used sol-gel processing to embed PbS nanoparticles in a silica glass, producing PL emission peaks at wavelengths of 440 and 605 nm.

When the size of nanoparticles is on the order of the dimension of the Bohr exciton, unique physical and chemical properties appear because of the quantum confinement effect [16]. The blue shifting of spectral peaks as the particle size decreases has achieved special attention recently, because of the exciting scope of this effect in fabricating novel electronic devices and solar cells of better efficiency [17]. The band-gap of PbS nanoparticles are significantly blue-shifted from the near-infrared (IR) into the visible and near ultraviolet (UV) region with decreasing particle size compared to bulk counterpart [18]. As a consequence, they have a technological potential in the field of photoelectrochemical solar cells, catalysis, light emitting diodes, resonant tunneling devices, lasers, gas sensors, etc. [16].

Generally, when the mean size of phosphor particles becomes smaller (1 – 2 µm), their luminescent efficiency becomes lower, since surface defects become important with decreasing particle size and increasing surface area and this often reduces the emission intensities [10]. However, it was found that the emission intensity was increased by reducing the particle size of the phosphor $Y_2O_3:Eu^{3+}$ from 6 µm to 10 nm [10]. It is also reported that ZnS capping of CdS:Mn results in better photostability for the nanoparticles [19]. Therefore, capping of the PbS nanoparticle phosphors with SiO_2 was applied in order to minimize the surface effects and to improve their luminescent properties.

A serious obstacle to the development of field emission flat-panel displays is the lack of phosphors with high efficiency at an electron acceleration voltage near 1 kV [20]. This led to the realization of non-radiative energy transfer between nanoparticle phosphors via electronic interaction. The process involves the interaction between two separated luminescent centers, a sensitizer/energy donor and energy acceptor, where the energy is transferred from the donor to the acceptor.

The application of powder phosphors on screens raised some serious concerns which include debonding, outgassing and carbon contamination. All these can be eliminated by using thin film phosphors technology [21]. This has resulted in significant interest in the development of thin film phosphors for field emission and plasma-panel displays. Field-emission flat-panel displays require thinner phosphor layers that operate at lower voltages compared to the cathode ray tubes without sacrificing brightness or contrast [22]. Thin films, as opposed to the traditional discrete powder screens, offer the benefit of reduced light scattering, a reduction of material waste and the potential for fabricating smaller pixel sizes to enhance resolution [22].

1.2. Problem Statement

The development of new types of high resolution and high efficiency displays has created a need for phosphors with new or enhanced properties. High efficiency materials with fine particles are sought to allow the further development of these new displays [23,24]. It has also been reported that high definition displays require submicron particle sizes to maximize screen resolution and luminescence efficiency [19]. Current commercial processes for manufacturing phosphors use mechanical milling to control the particle size and result in particles that are larger than about 2 µm. Nanoparticles can be synthesized with sizes ranging from 2 to 100 nm and thus fulfill the size requirement without mechanical milling. A new class of luminescent materials, nano-sized phosphors, has demonstrated interesting properties such as high quantum efficiency for photoluminescence, ultra-fast recombination time and increased energy band gap for luminescence due to the tiny size of the particles [15,25,26]. A great deal of work done during recent years has laid a special emphasis on the nanocomposites consisting of nanoparticles embedded in dielectric matrices such as glasses and polymers. PbS is of considerable interest as a phosphor for luminescent displays [15].

Due to its narrow band gap (0.41 eV) and large Bohr exciton radius (18 nm), PbS appears to be a very good candidate, and the development of this phosphor could make a huge impact technological or otherwise. Cathodoluminescence (CL) and photoluminescence (PL) studies will be performed on the luminescent properties of the nanoparticle powder phosphors and thin films. The luminescent properties of nanoparticle phosphors are compared for application in field emission and plasma display technologies. A particular interest in these properties is at low accelerating voltages (equal or less than 2 keV).

1.3. Study Objectives

1. To synthesize PbS nanoparticle phosphor embedded in a SiO_2 matrix using sol-gel.
2. To investigate cathodoluminescence degradation of SiO_2:PbS phosphor.
3. To study photoluminescence properties of SiO_2:PbS powder phosphor.
4. To investigate photoluminescence properties of the thin luminescent SiO_2:PbS films as compared to the SiO_2:PbS powder.
5. To investigate energy transfer from ZnO nanoparticles to PbS nanoparticles both embedded in SiO_2 matrix.

1.4. Thesis Layout

Chapter 2 provides background information on nano-science, quantum confinement, fundamentals of phosphors and luminescence processes such as cathodoluminescence and photoluminescence. Detailed information on the sol-gel synthesis of nanoparticles and nano-phosphors is provided. Brief information on energy transfer in phosphors and cathodoluminescence degradation of phosphors is tabled. The pulsed laser deposition process for growing thin films is also discussed.

A summary of surface analysis techniques used in this study is provided in chapter 3. This includes a brief description on how each of these techniques works. Sol-gel synthesis of SiO_2:PbS nanoparticles is discussed in chapter 4. In chapter 5, cathodoluminescence degradation of the SiO_2:PbS powder phosphor is reported. Photoluminescence study of SiO_2:PbS nanoparticle phosphor is presented is chapter 6.

In chapter 7, photoluminescence properties of the SiO_2:PbS thin films grown by PLD process and powder phosphor are presented. Chapter 8 deals with energy transfer from ZnO nanoparticles to PbS nanoparticles embedded in SiO_2 matrix. A possible mechanism for energy transfer from one luminescent centre to another is presented.

Finally, in chapter 9, a summary of the thesis, concluding remarks and suggestions for possible future studies are presented.

References

[1] K.P. Chong, *J. Physics and Chemistry of Solids*, **65** (2004) 2.

[2] A.L. Rogach, A. Eychmuller, S.G. Hickey and S.V. Kershaw, *Reviews; Infrared emission*, www.small-journal.com, small 2007, **3** (4) 536.

[3] S.J. Fonash, *J. of Nanoparticle Research*, **3** (2001) 79.

[4] M.C. Roco and W.S. Bainbridge, Societal Implications of Nanoscience and Nanotechnology, (Springer, Boston) 2001.

[5] S.C. Tjong and H. Chen, *Materials Science and Engineering: Reports*, **45** (2004) 2.

[6] C.J. Murphy, *Material Science*, **298** (5601) (2002) 2139.

[7] S. Pratsims, Particle technology laboratory, www.ptl.ethz.ch, 2005.

[8] H. Zhang, D. Yang, X. Ma, Y. Ji, S.Z. Li, and D Que, *Materials Chemistry and Physics*, **93** (2005) 65.

[9] A. Martucci, J. Fick, Serge-Emile LeBlanc, M. LoCascio, A Hache, *J. of Non-Crystalline Solids*, **345&346** (2004) 639.

[10] T. Hirai, Y. Asada, I. Komasawa, *J. of Colloidal and Interface Science*, **276** (2004) 339.

[11] Y.J. Yang, L.Y. He, and Q.F. Zhang, *Electrochemistry Communications*, **7** (2005) 361.

[12] S. Chen, L.A. Truax, and J.M. Sommers, *Chem. Mater.*, **12** (2000) 3864.

[13] K.S. Babu, C. Vijayan, P. Haridoss, *Materials Research Bulletin*, **42** (2007) 996.

[14] J. Auxier, K. Wundke, Schulzgen, N. Peyghambarian, N.F. Borrelli, Lasers and Electro-Optics, 2000. (CLEO 2000). Conference on 7-12 May 2000 Page:385.

[15] P. Yang, C.F. Song, Meng Kai Lu, Xin Yin, Guang Jun Zhou, Dong Xu, Duo Rong Yuan, *Chemical Physics Letters*, **345** (2001) 429.

[16] K.K. Nanda, F.E. Kruis, H. Fissan, M. Acet, *J. Appl. Phys*, **91(4)** (2002) 2315.

[17] K.B. Jinesh, C.S. Kartha, K.P. Vijayakumar, *Appl. Surf. Sci*, **195** (2002) 263.

[18] H.Cao, G. Wang, S. Zhang, X. Zhang, *Nanotechnology*, **17** (2006) 3281.

[19] H. Yang, P.H. Holloway, *J. Chem. Phys*, **121** (2004) 7421.

[20] A.D. Dinsmore, D.S. Hsu, H.F. Gray, S.B. Qadri, Y. Tian, B.R. Ratna, *Applied Physics Letters*, **75(6)** (1999) 802.

[21] R.K. Singh, Z. Chen, D. Kumar, K. Cho, M. Ollinger, *Appl. Surf. Sci*, **197-198** (2002) 321.

[22] J. McKittrick, C.F. Bacalski, G.A. Hirata, K.M. Hubbard, S.G. Pattillo, K.V. Salazar, M. Trkula, *J. Am. Ceram. Soc*., **83** (5) (2000) 1241.

[23] L.L. Breecroft, K.C. Ober, *Chem. Mater*., **9** (6) (1997) 1302.

[24] L. Sun, C. Qiang, C. Liao, X. Wang, C. Yan, *Solid State Communications*, **119** (2001) 393.

[25] Myung-Han Lee, Seong-Geun Oh, and Sung-Chul Yi, J. *Colloid and Interface Sci.* **226** (2000) 65.

[26] R.N. Bhargava, *J. Lumin*., **70** (1996) 85.

CHAPTER 2

SEMICONDUCTOR NANOPARTICLES AND THIN FILMS

2.1. Introduction

Semiconductor quantum dots, also known as nanocrystals or nanoparticles, are a special class of materials whose crystals are composed of periodic groups of II-VI, III-V, or IV-VI materials. The most notable and interesting property of semiconductor nanoparticles is the distinct large magnitude change in optical properties as a function of particle size. The three-dimensional quantum-size effect, leading to an increase in band gap with a decrease in particle size, is well known for colloidal semiconductor sols where the individual colloidal particles are dispersed in a liquid or glass [1].

Narrow band gap semiconductor nano-crystals embedded in dielectric matrices were observed to behave as quantum boxes when their radii are smaller than their exciton Bohr radii, the circumstances under which their optical properties are strongly modified compared to bulk [2]. Bulk PbS (rock-salt crystal structure) is a direct band gap IV-VI semiconductor with a narrow band gap of ~ 0.41 eV [3,4] and a large exciton Bohr radius of ~18 nm at room temperature, which means the strong quantum confinement regime is easily obtained in PbS nanoparticles [5]. The size, shape, capping material and surface characteristics have strong influence on the optical properties of the PbS nanoparticles [3].

2.2. Particle size effects

2.2.1. Quantum confinement effect

Quantum confinement effect is defined as the increase in band gap of a semiconductor material as the particle size decreases. It is caused by localization of electrons and holes in a confined space resulting in observable quantization of the energy levels of the electrons and holes. The idea behind confinement is all about keeping electrons and holes trapped in a small area. For effective confinement, the particle sizes have to be less than 30 nm [6]. Quantum confinement comes in several forms which include 2-D (two dimensional) confinement, which is only restricted in one dimension, and the result is a quantum well (or plane), and these are what most lasers are currently built from. 1-D confinement occurs in nanowires and 0-D confinement is found only in the quantum dot. In nature 0-D confinement is found in atoms. A quantum dot exhibits 0-D confinement, meaning that electrons are confined in all three dimensions. So a quantum dot can be loosely described as an artificial atom [7,8] because of the discretization of conduction and valence bands caused by quantum confinement of charge-carriers. This achievement is very important since we can not readily experiment on regular atoms because they are too small and too difficult to isolate in an experiment. Quantum dots, on the other hand, are big enough to be manipulated by magnetic fields and can even be moved around [6]. Quantum confinement is vitally important for one thing, it leads to new electronic properties that are not present in today’s semiconductor devices. The density of states functions plotted against energy for bulk (3-D), 2-D, 1-D and 0-D are shown in figure 2.2.1. The continuous energy levels of the bulk and the discrete energy levels for quantum dots (0-D) are apparent in this figure.

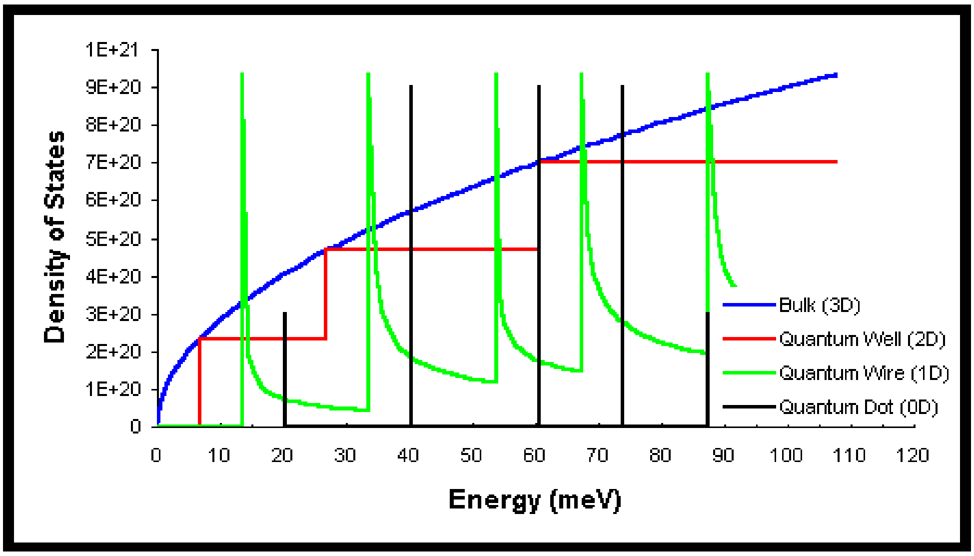

Figure 2.2.1. Density of states functions plotted against energy for bulk (3-D blue), quantum well (2-D red), quantum wire (1-D green) and quantum Dot (0-D black) [9].

In semiconductors, an electron-hole pair is created when an electron leaves the valence band and enters the conduction band due to excitation. An exciton is created when a weak attraction force (Coulombic force) between the hole and electron exists. It may be bound or moving in a crystal conveying energy. Luminescence may result from the recombination of the electron and the hole. Excitons have a natural physical separation that varies from semiconductor to semiconductor. This average separation distance is termed Exciton Bohr Radius. In bulk, the dimensions of the semiconductor crystal are much larger than the Excitonic Bohr Radius, allowing the exciton to extend to its natural limit [10]. The energy levels of a bulk semiconductor are very close together such that they are described as continuous, meaning that there is almost no energy difference between them, as shown in figure 2.2.2 (a) [11]. Since the band-gap of the bulk semiconductor is fixed, the transitions result in fixed emission frequencies.

However, if the sizes of a semiconductor particle are comparable or small enough that they approach the size of the material's bulk Exciton Bohr Radius, then the continuum states are broken down into discrete states [12] and can no longer be treated as continuous, meaning that there is a small and finite separation between energy levels as shown in figure 2.2.2 (b). This result in a large effective band gap and leads to an optical transition which is blue-shifted from that of bulk materials [12,13].

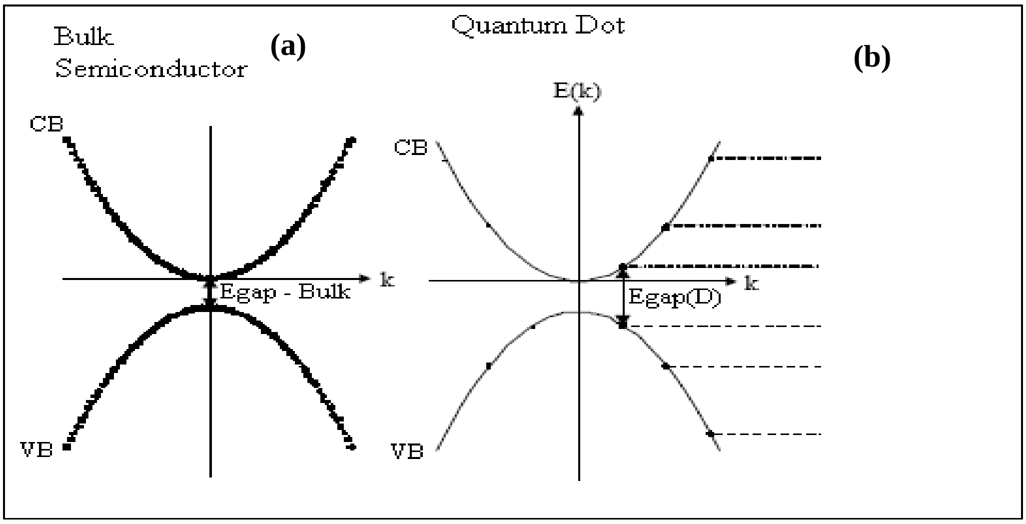

Figure 2.2.2. Energy Dispersion for the (a) 3-D bulk semiconductor case compared to that of the (b) 0-D Quantum Dot case [11].

The Bohr radius of the exciton (a_B) is given by the following equation [14]:

$$a_B = \frac{\hbar^2 \varepsilon}{e^2}\left[\frac{1}{m_e}+\frac{1}{m_h}\right], \tag{2.1}$$

where ε is the dielectric constant, $\hbar$ is the reduced Planck's constant, e is the electronic charge, and m_e and m_h are the electron and hole effective masses, respectively.

There are several approaches to understand and explain quantum confinement effects quantitatively. In this study, only three of them are discussed. The first approach is the effective mass approximation (EMA) model. It is known that for a free particle, delocalized electron waves follow a quadratic relationship between wave vector k and energy E:

$$E = \hbar^2 k^2 / 2m_e \tag{2.2}$$

where E is the energy of a particle, k is the wave vector and m is the effective mass. In the effective mass approximation, the above relationship is assumed to hold for an electron or hole in the periodic potential well of semiconductor, implying that the energy band is parabolic near the band gap. The size-dependent excitonic energy (band gap) shift of a nanocrystal with respect to bulk counterpart can thus be derived as

$$\Delta E_g = \frac{\hbar^2\pi^2}{2\mu R^2} - \frac{1.8e^2}{\varepsilon R} = \frac{\hbar^2\pi^2}{2R^2}\left[\frac{1}{m_e} + \frac{1}{m_h}\right] - \frac{1.8e^2}{\varepsilon R}; \qquad (\ 2.3)$$

where ΔE_g *(eV)* is the band gap shift of a nanocrystal compared to that of bulk, R is the radius of the nanocrystal, and μ is the reduced mass of an electron-hole pair ($\frac{1}{\mu} = \frac{1}{m_e} + \frac{1}{m_h}$). The first term represents the particle in a box quantum localization energy (confinement energy) with $1/R^2$ dependence and the second term represents the Coulomb interaction energy with 1/R dependence. The first excitonic transition (band gap) increases in energy with decreasing particle size. The variations of the theoretical and experimental conduction-valence band gap as a function of CdSe nanocrystal size are compared in figure 2.2.3. The EMA model is not quantitatively accurate as shown by the deviation from the experimental values, particularly for very small nano-crystals [14]. This breakdown of the EMA model for such smaller nanocrystals is because the eigenvalues of the lowest excited states are for a region of the energy band that is no longer parabolic [14].

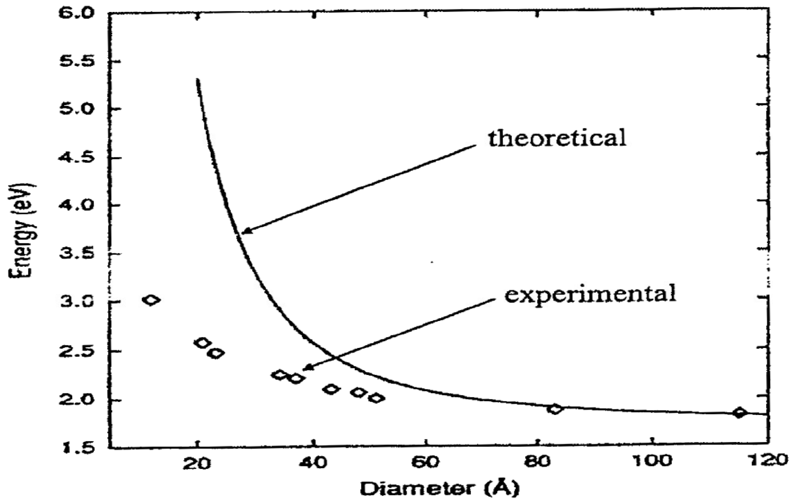

Figure 2.2.3. Variations of transition energy as a function of diameter for CdSe nanocrystal observed experimentally versus theoretically obtained using the simple effective mass approximation [14].

The second approach is the tight binding approximation model which can be understood as the opposite extreme of the nearly free electron model and regards the solid as an assembly of weakly interacting neutral atoms [15]. It basically considers the overlap of atomic orbitals in a bonded system as the source for corrections of the isolated atom picture [15]. It provides a real space picture of the electronic interactions and is extremely useful in the study of changes in band structure, the density of states, and related functions due to variations in the electronic configuration. This is well displayed in a three dimensional tight binding energy equation [16]:

$$E(k) = E_o^{'} + 4\gamma\left[\sin^2\left(\frac{k_x a}{2}\right) + \sin^2\left(\frac{k_y a}{2}\right) + \sin^2\left(\frac{k_z a}{2}\right)\right], \qquad 2.4$$

where *E(k)* is the band energy as a function of *k*, $E_o^{'}$ $(= E_v - \beta - 2\gamma)$ the energy at the bottom of the band and 4γ is the bandwidth. Figure 2.2.4 illustrates the comparison between the experimental and theoretical band gap as a function of PbS nanocrystal size

[2]. From the figure it can be seen that the model is also not accurate enough in the small size regime as in the case of effective mass approximation.

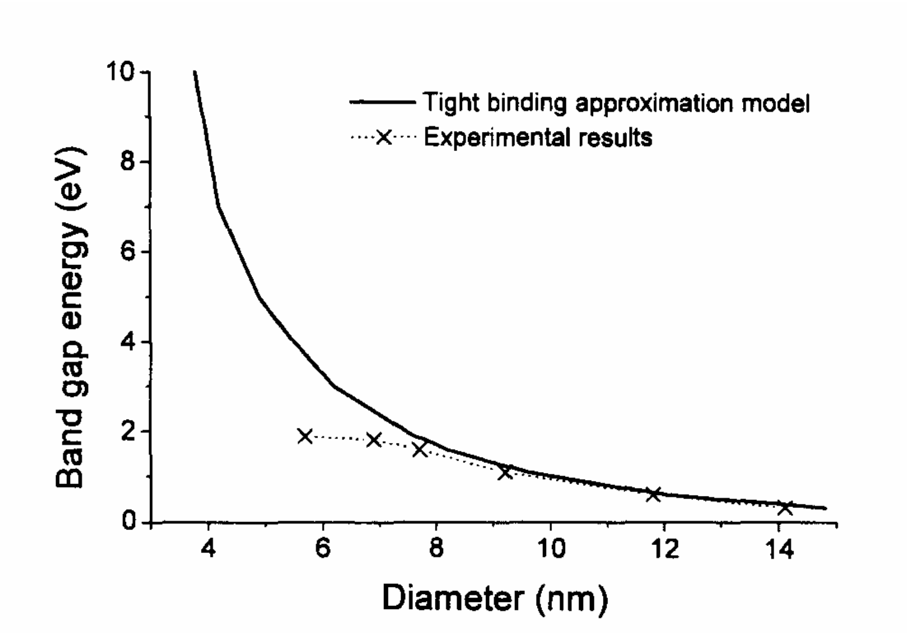

Figure 2.2.4. The energy shifts for various PbS diameters observed experimentally versus theoretically obtained using the tight binding approximation model [2].

Figure 2.2.5 illustrates quantitatively the third approach which uses a linear combination of atomic orbitals-molecular orbitals (LCAO-MO) theory. This approach provides a natural framework to understand the evolution of clusters from molecules to bulk and the size dependence of the band gap. In the diatomic limit, the atomic orbitals of the two individual atoms are combined, producing two (bonding and anti-bonding) molecular orbitals. In this approach, nanometer-sized semiconductor nanocrystals are described as very large molecules. As the number of atoms increases, the number of sets of atomic orbitals increases, evolved from an incomplete, discrete energy band structure to continuous bands. The highest occupied molecular orbital (HOMO) and lowest unoccupied molecular orbital (LUMO) form the quantum states at the top of the valence band and the bottom of the conduction band, respectively [14]. The size of nanocrystals place them intermediate between the atomic/molecular and extended bulk crystalline descriptions and properties. The energy difference between the HOMO and LUMO (band gap) increases and the bands split into discrete energy levels with a decreasing number of atoms due to reduced mixing of atomic orbitals. Unlike the effective mass and tight binding approximation models, the LCAO-MO theory provides a good method to calculate the energy structure of even the smallest semiconductor nanocrystals.

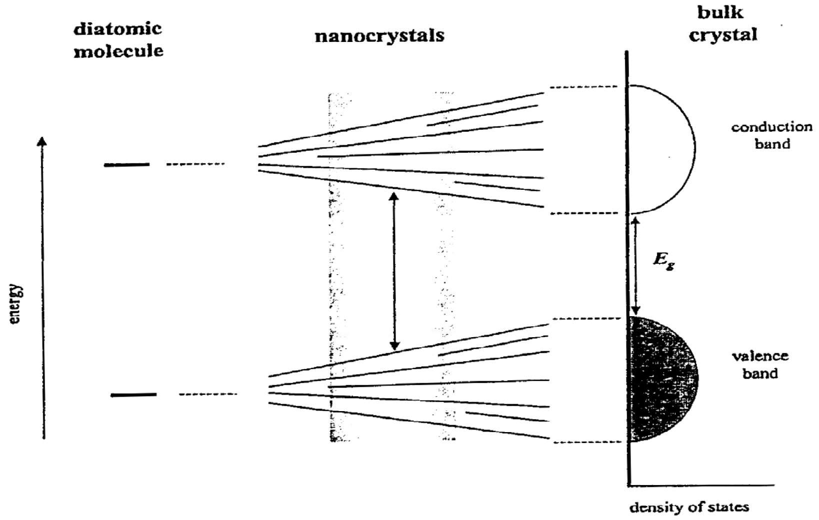

Figure 2.2.5. Evolution of molecular orbitals into band: from diatomic molecules to crystals [14].

Practically, Van Dijken at al [17] studied the relationship between the energy band-gap and the particle size of the ZnO nanocrystalline particles. They observed a shift in both conduction (e) and valence (h) bands edges with the decrease in particle size ($\frac{1}{m_e{}^*R^2}$ and $\frac{1}{m_h{}^*R^2}$, respectively), as shown in figure 2.2.6. The dashed line represents the energetic position of a trapped charge carrier. The two possibilities for trap emission are recombination of a delocalized electron with a deeply trapped hole (a) and recombination of a delocalized hole with a deeply trapped electron (b).

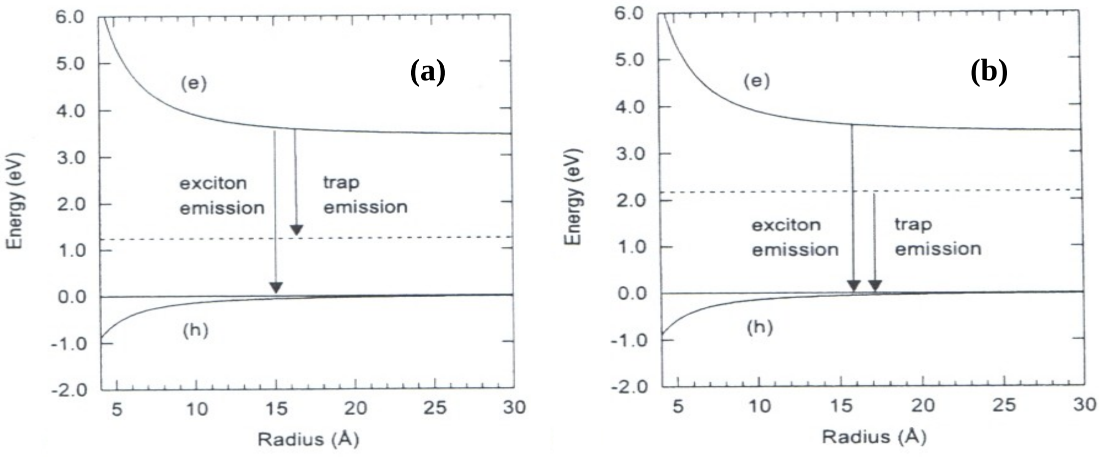

Figure 2.2.6. Schematic representation of the band-gap dependency on particle size and the possibilities for trap emission in nanocrystalline ZnO particles [17].

However, due to the fact that the surface related non-radiative recombination dominates in the strong confinement, the practical photonic applications of these nanocrystals are reported lacking [18,19]. Steps to be taken in order to eliminate or minimize the non-radiative recombination are explained in detail in the next section.

2.2.2. Surface effects

At the surface of a pure semiconductor, substantial reconstructions in the atomic positions occur, and it is nearly inevitable that there exist energy levels (surface states) within the energetically forbidden gap of the bulk solid [14,20] arising from the surface non-stoichiometry, unsaturated bonds, etc. These surface states act as traps for electrons or holes and manifest themselves as a degradation of the electrical and optical properties of the material. In some cases the surface states can also be involved in radiative transition. The relatively large surface to volume ratio in semiconductor nanoparticles results in strong influence of the surface states on their optical properties [21] and with decreasing particle size, the fraction of the surface molecules aggregates increases [5]. This leads to imperfect surface which can act as traps for photogenerated electrons and holes. Surface atoms have fewer bonds in comparison to the atoms in the bulk because of the loss in nearest neighbors. They tend to find new equilibrium positions to balance the forces, resulting in surface reconstruction and defects [22]. The search for new optical materials with strong optical nonlinear behavior has motivated experiments with surface chemical modification [21].

For example; lead sulfides (chalcogenides) have a narrow band gap (~ 0.41 eV) and exceptionally large exciton Bohr radii (~ 18 nm) which make them susceptible to charge carrier quantum confinement effects over a broad range of nanocrystal sizes (≤18 nm) [23]. For many years this prevented PbS nano-crystals from producing high yields of photoluminescence, as most of the energy was lost through non-radiative processes. However, there have been several successes recently in producing highly luminescent PbS nano-crystals by either overcoating with a higher band gap material (CdS) or by the attachment of ligands such as oleic acid to the surface – a chemical process called passivation [24].

Passivation is the chemical process by which the surface atoms are bonded to another material of a much larger band gap, in such a way as to eliminate all the energy levels inside the forbidden band gap. This can be achieved in several ways which include nanocrystals suspended as colloidal particles in liquid, nanocrystals formed in a matrix such as glass or polyethylene film, nanocrystals in cages such as zeolites [25] and individual nanocrystals coated with a passivating layer such as methacrylic acid [18].

However, these coated or matrix based encapsulated nano-crystals have found limited applications due to the inherent difficulty in the passivation of the individual nanocrystalline surface. Bhargava [18] reported the introduction of impurity in a quantum dot to further decrease the contribution of the surface-related nonradiative recombination. It was reported that by introducing an impurity in a quantum dot confined structure, the dominant recombination route can be transferred from the surface states to the impurity states. If the impurity induced transition can be localized, the radiative efficiency of the impurity-induced emission increases significantly.

Surface passivation by organic molecules consists of coordination between capping molecules and anionic or cationic surface atoms. Apart from contributing to surface passivation, organic capping agents also increase the solubility of nanocrystals in specific solvents and prevent the agglomeration of nanoparticles. However problems with organic capping, of which one arises in matching the organic ligands with surface atoms of the crystallites. Most organic capping molecules are conical or distorted in shape, and large and bulky [14]. Thus, the coverage of capping molecules on the surface atoms is limited by steric effects, depending on the curvature of the surface. It is generally difficult to simultaneously passivate both anionic and cationic surface sites by organic capping, i.e., there are always some dangling bonds on the surface. Another disadvantage of organic capping is instability. The bonding at the interface between capping molecules and surface atoms is generally metastable, leading to the failure of bonding and further degradation upon the exposure to UV or visible light [14].

However, there has been interest in the possibility of passivating nanocrystals with an inorganic shell. In this way, the lattice matching between core and shell is important for the epitaxial growth of shell layer on the surface of core crystal. Growth of inorganic epitaxial shells on core nanocrystals can generate novel nanocrystal systems where the surface-related defect states are eliminated by simultaneously passivating dangling bonds at both anionic and cationic surface sites. Furthermore, since the core material may be passivated by an inorganic material of wider band gap, a potential step (or band offset potential) of several tenths of an eV at the interface could reduce the probability for charge carriers to reach the surface, i.e., charge carriers are confined in the core material.

This combination could lead to both photostability as well as improved luminescence efficiency. The most efficient energy transition would be from the highest probability of electron/hole wave function overlap into the core due to carrier confinement, and of the recombination of these carriers away from the non-radiative traps/defects associated with nanocrystal surface. Furthermore, the confinement of charge carriers into the core material by potential barriers makes the charge carriers less accessible to surface states. PbS quantum dots have been fabricated in zirconium hosts, porous TiO_2 electrodes, polymers hosts, and glass hosts. Large blue-shifts and discrete characteristics of quantum confinement of carriers have been obtained for the PbS quantum dots in glass hosts [13].

Another interesting property that will manifest in low dimensional structure is dielectric confinement effect. When organic molecules capped on semiconductor nanoparticles have a relatively smaller dielectric constant than that of the nanoparticles, the electric force lines emerging from charged particles within semiconductor nanoparticles pass through the surrounding medium, the screening effect is reduced and the Coulombic interaction between charged particles is enhanced [12]. Fernee et al [26] reported that for PbS nano-crystals in the strong quantum confinement regime, proper surface passivation should be extremely important as both charge carriers should strongly interact with the surface due to the quantum confinement. Quantum confinement effects, as well as dielectric confinement effect tailors the optical properties of semiconductor nanoparticles.

2.2.3. Melting temperatures

The melting temperatures of nano-crystals strongly depend on the crystal size and are substantially lower than the bulk melting temperature [22]. This has received considerable attention since Takagi in 1954 experimentally demonstrated that ultra-fine metallic nanoparticles melt below their corresponding bulk melting temperature [27]. The dependency of melting temperatures (T_m) on the particle size has been well established both experimentally and theoretically. It is now known that the melting temperatures of all low-dimensional crystals including metallic, organic, and semiconductor depend on their sizes. For free standing nanoparticles, the melting temperature decreases as its size decreases [27,28,29]. It was also observed that for substrate-supported nanoparticles with relatively free surface, the melting temperature decreases with decreasing particle size [30].

In contrast, the existing experimental evidence for the embedded nanoparticles revealed that the melting temperature can be lower than the bulk melting point for some matrices while the same nanoparticle embedded in some other matrices can exhibit superheating to temperatures higher than the bulk melting point [30]. Experimental results revealed that the enhancement or depression of the melting temperature of the embedded nanoparticles depends on the amount of epitaxy between the nanoparticles and the embedding matrix. If the interfaces are coherent or semi-coherent, an enhancement of the melting point is present, otherwise a depression of melting point occurs [27]. For the superheating of nanoparticles embedded in a matrix, a model has been developed according to which the superheating is possible if the diameter of the constituent atoms of the matrix is smaller than the atomic diameter in the nanoparticles [30]. Furthermore, Nanda et al [30] reported that superheating is possible when nanoparticles with lower surface energy are embedded in a matrix with a material of higher surface energy.

The melting temperature of nanoparticle and their corresponding bulk is described by the following expression;

$$T_m(r)/T_m(\infty) = \exp[-(\alpha-1)/(r/r_o-1)], \tag{2.4}$$

where $T_m(r)$ and $T_m(\infty)$ are the melting temperatures of the nanoparticles with radius r and corresponding bulk crystals, respectively, r_o denotes a critical radius at which all atoms of the particle are located on its surface. α is defined as the ratio of the mean square displacement (msd) of atoms on the surface and that in the interior of crystals. It is clear from (2.4) that $T_m(r)$ function depends on α. If $\alpha>1$, $T_m(r)/T_m(\infty)<1$, $T_m(r)$ decreases as r decreases. When $\alpha<1$, $T_m(r)/T_m(\infty)>1$ imply that $T_m(r)$ increases as r increases. For crystals with free surfaces, such as free-standing particles, particles or thin films deposited on substrates, and nanowires in porous glasses, msd of the surface is larger than that of the interior atoms of the nano-crystals and $\alpha>1$. α and r_o are defined as; $\alpha = [2S_m(\infty)/(3R)] + 1$ and $r_o = (3-d)h$. By substituting α and r_o, equation (2.4) may be written as:

$$T_m(r)/T_m(\infty) = \exp\{-2S_m(\infty)/[3R(r/r_o-1)]\}. \tag{2.5}$$

When nano-crystals are embedded in the matrix, their surface atoms are no longer free-standing and α could be smaller than one due to the interaction on the interfaces between the embedded nano-crystal and the matrix. Tjong et al [31] studied the melting temperature of gold nanoparticles, and observed a dramatic decrease from 1063 to ~ 300 ^{o}C for diameters smaller than 5 nm.

2.3. Methods of synthesis of nanoparticles

A number of methods to synthesize semiconductor nano-crystals have been employed and these include hydrothermal synthesis [32], hydroxide precipitation, chemical bath [33], solid state reactions, spray pyrolysis, laser-heated evaporation, combustion synthesis and the sol-gel technique [34]. Among these methods, sol-gel processing offers many advantages which include low processing temperature, high purity, molecular level homogeneity and more flexibility in the components of the glass [35,36,37]. Due to its advantages, the sol-gel approach was used in this study, and it is discussed in detail in the next subsection.

2.3.1. Sol-gel process

The sol-gel process is defined as a wet chemical route for the synthesis of colloidal dispersions (sols) of inorganic and organic-inorganic hybrid materials, particularly oxides and oxides-based hybrid at relatively low temperatures. The sols are subsequently converted into viscous gels (sol-gel transition) [38]. At the transition, the solution or sol becomes a rigid, porous mass through destabilization, precipitation, or supersaturation. Sols are dispersions of colloidal particles in a liquid [39] and colloids are solid particles with diameters of 1 – 100 nm. The sol becomes a gel when it can support stress elastically. A gel is an interconnected, rigid network with pores of submicrometer dimensions and polymeric chains whose average length is greater than a micrometer [40]. The gels are usually dried at room temperature to form powders. In the sol-gel process, grain growth occur at the same time as agglomeration such that it becomes difficult to differentiate between primary particles which consist of small grains or crystallites, and secondary particles which are agglomerates of primary particles [41]. Figure 2.3.1 shows the primary particles of about 2 nm in diameter that agglomerate in secondary particles of about 6 nm.

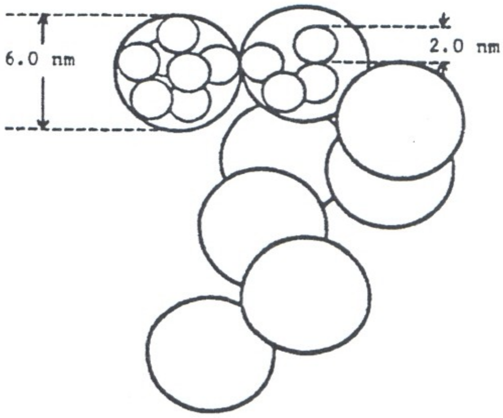

Figure 2.3.1. Schematic representation of primary and secondary particles in alkoxide gel [39].

The crystal growth technique in gels has become very important because it is straightforward and can be used at room temperature, in similar conditions to those under which crystal grow naturally [40]. Thus, it enables the incorporation of organic elements into inorganic materials without deterioration of their functionality. The sol-gel processing is particularly useful in making complex metal oxide, temperature sensitive organic-inorganic hybrid materials, and thermodynamically unfavorable or metastable materials [35]. The use of the sol-gel method has attracted great scientific interest in the recent years for making advanced materials and for designing devices with very specific properties [42].

Interest in the sol-gel processing of inorganic ceramic and glass materials began as early as the mid 1800s with Ebelman and Graham's studies on silica gels [39]. These early investigators observed that the hydrolysis of tetraethylorthosilicate (TEOS), under acidic conditions yielded SiO_2 in the form of a glass-like material. For a period from the late 1800s through to the 1920s, gels became of considerable interest to chemists stimulated by the phenomenon of Liesgang Rings formed from gels. In the 1950s and 1960s, the potential for achieving very high levels of chemical homogeneity in colloidal gels was realized to synthesize large number of novel ceramic oxide composition that could not be made using traditional ceramic powder methods. One unique feature of the sol-gel process is the ability to go all the way from the molecular precursor to the product, thus allowing better control of the whole process [42].

Typical sol-gel processing consists of hydrolysis of precursors. The versatile precursors for the sol-gel synthesis of oxides are metal alkoxides, but organic and inorganic salts are also often used [42,43]. The alkoxide used most often to synthesize SiO_2 is TEOS, which is the product of the reaction of $SiCl_4$ and ethanol [26,38]. Precursors may be dissolved in organic or aqueous solvents and catalysts are often added to promote hydrolysis and condensation reactions. A silica gel may be formed by network growth from an array of discrete colloidal particles or by formation of an interconnected 3-D network by the simultaneous hydrolysis and polycondensation of an organometallic precursor. A liquid alkoxide precursor such as $Si(OR)_4$, where R may be CH_3, C_2H_5, or C_3H_7 is hydrolyzed by mixing with water to form hydrated silica and alcohol as shown below.

Hydrolysis:

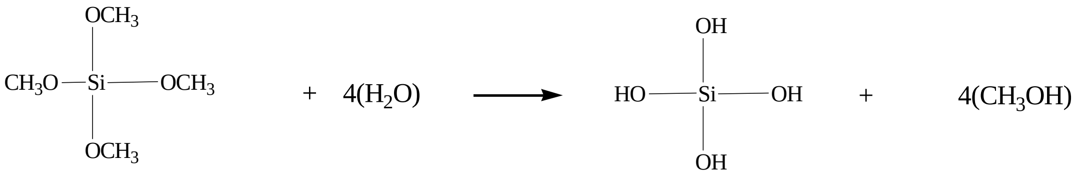

$$CH_3O-\overset{\overset{OCH_3}{|}}{\underset{\underset{OCH_3}{|}}{Si}}-OCH_3 \quad + \quad 4(H_2O) \longrightarrow HO-\overset{\overset{OH}{|}}{\underset{\underset{OH}{|}}{Si}}-OH \quad + \quad 4(CH_3OH)$$

The hydrated silica tetrahedral interacts in a condensation reaction forming $\equiv Si-O-Si\equiv$ bonds and water as shown below. The intermediate products that exist as a result of partial hydrolysis include SiOH groups called silanols, and $Si(OC_2H_5)$, called an ethoxy group. A condensation can occur between a silanol and ethoxy group to form a bridging oxygen or siloxane group Si-O-Si [38]. Condensation results in the formation of nano-scale clusters of metal oxides or hydroxides, often with organic groups embedded or attached to them. These organic groups may be due to incomplete hydrolysis or introduced as non-hydrolysable organic ligands. The nano-scale clusters size, along with the morphology and microstructure of the final product can be tailored by controlling the hydrolysis and condensation reactions.

Condensation:

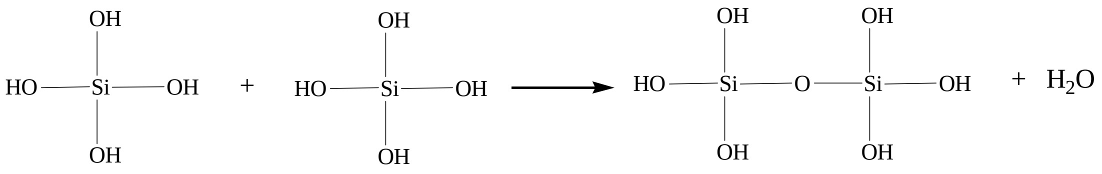

Linkage of additional $\equiv Si-OH$ terahedra occurs as a polycondensation reaction and eventually results in a SiO_2 network. The H_2O (in condensation) and alcohol (in hydrolysis) expelled from the reaction remains in the pores of the network.

Polycondensation:

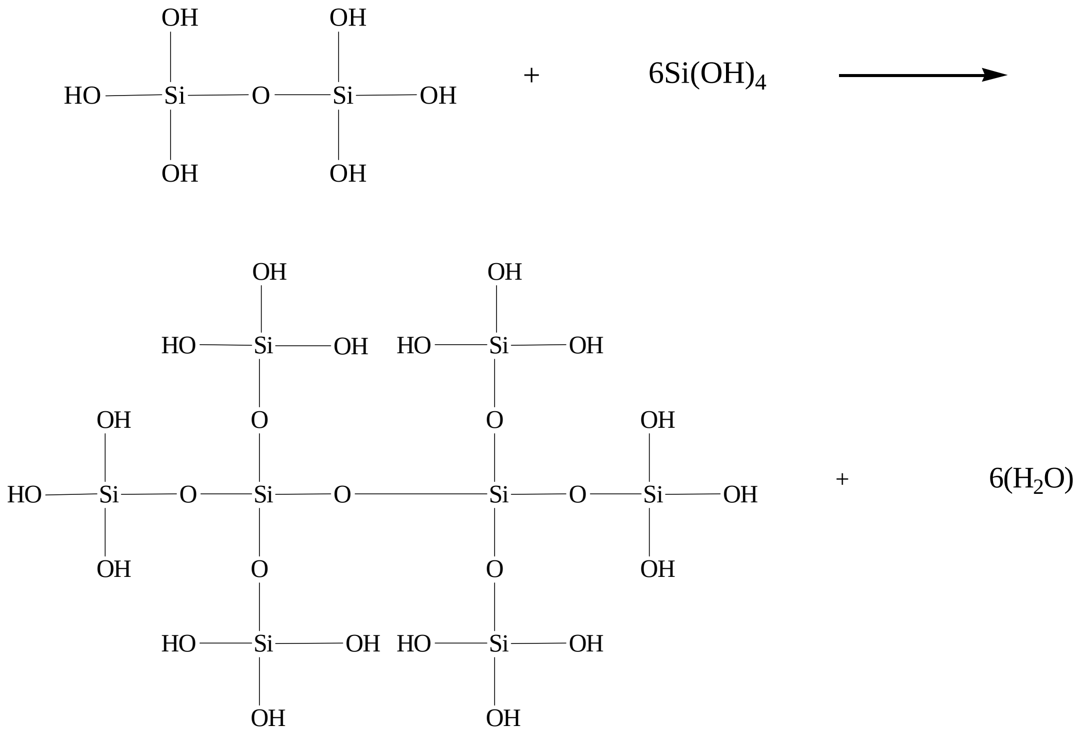

The overall equation for the formation of SiO_2 as a result of condensation reactions is given by:

$$Si(OC_2H_5)_4 + 2H_2O \rightarrow SiO_2 + 4C_2H_5OH \ .$$

The kinetics of the reaction is impracticably slow at room temperature, often requiring several days to reach completion. For this reason, acid or base catalysts are added to the solution. Acid catalysts can be any protic acid such as HCl, HNO_3 etc. Basic catalysis usually uses ammonia or ammonium fluoride. Aerogels prepared with acid catalysts often show more shrinkage during drying and may be less transparent than base catalyzed aerogels. Under acidic conditions, the structures are mostly linear with a low degree of cross-linking while for basic conditions, characteristic of branched polymers with high degree of cross-linking was observed. This is clearly shown in figure 2.3.2 below.

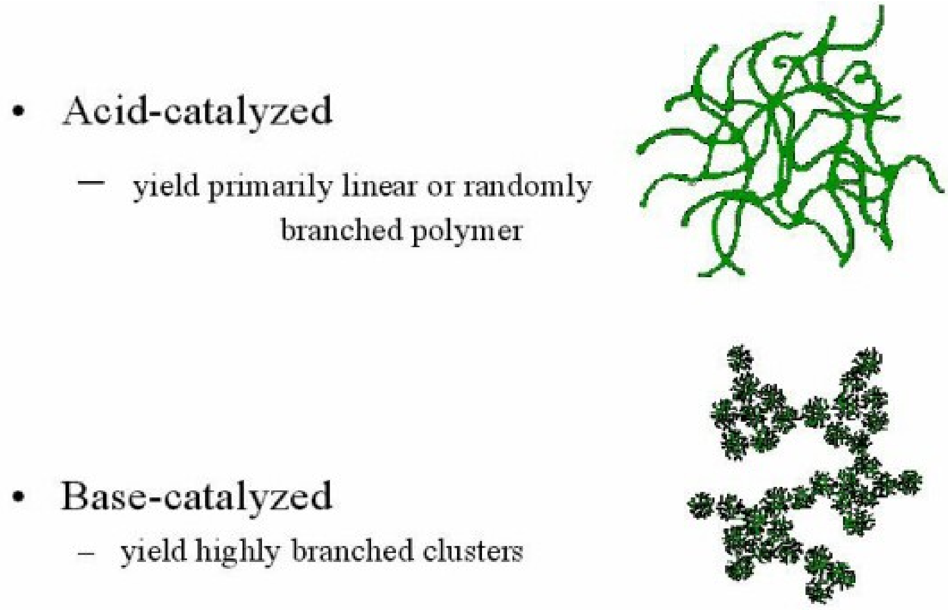

- Acid-catalyzed
  - yield primarily linear or randomly branched polymer
- Base-catalyzed
  - yield highly branched clusters

Figure 2.3.2. Summary of acid/base sol-gel conditions [44].

Despite the chemical equation shown, the mole ratio of water to TEOS is a particularly useful number for predicting the behavior of solution. When the mole ratio (R) is increased while maintaining a constant solvent: silicate ratio, the silicate concentration is reduced. This in turn reduces the hydrolysis and condensation rates, and results in longer gel times. This behavior is apparent in figure 2.3.3. The most concentrated solution with ethanol: TEOS = 1, has the shortest gel time, while the most dilute solution with ethanol: TEOS = 3 takes the longest time to gel. The ratio of ethanol to TEOS is equally useful, and when omitted makes the estimation of oxide content in the solution difficult. Klein [38] reported the linear increase in gel time from the concentrated to dilute solutions. By careful control of sol preparation, monodispersed nanoparticles of various oxides, including complex oxides, organic-inorganic hybrids, and biomaterials can be synthesized. The key issue here is to promote temporal nucleation followed with diffusion controlled subsequent growth.

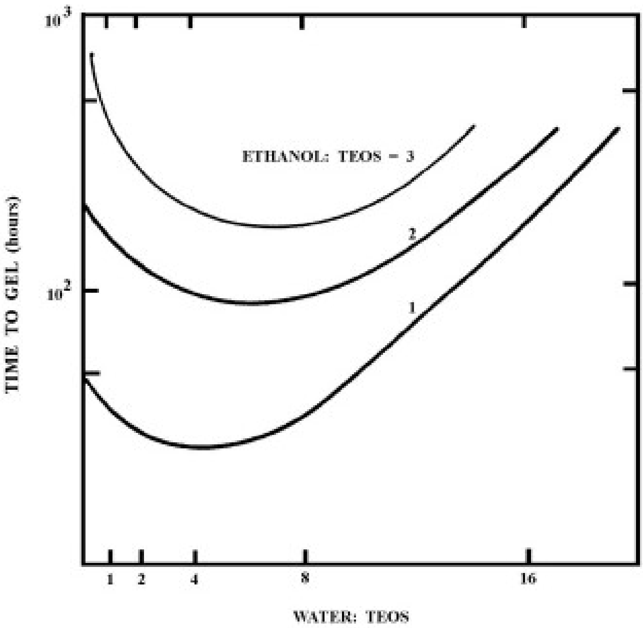

Figure 2.3.3. Gel times as a function of water: TEOS ratio, R [38,44].

The particle size can be varied by changing the concentration and aging time. When a gel is maintained in its pore liquid, its structure and properties continue to change long after the gel point and the process is called aging. The process is illustrated in figure 2.3.4. During aging, polycondensation continues along with localized solution and reprecipitation of the network. The strength of the gel is reported to increase with aging.

The liquid is removed from the interconnected pore network during drying. Large capillary stresses can develop during drying when pores are small (<20 nm) and these stresses will cause the gels to crack catastrophically unless the drying process is controlled [39]. Wet-aged increased coalescence and cause little shrinkage on drying.

Structural evolution during sol to gel and gel to solid transitions needs to be fully understood to achieve real mastery of the sol-gel process [42]. The properties of a gel and its response to heat treatment are very sensitive to the structure already formed during the sol stage [42].

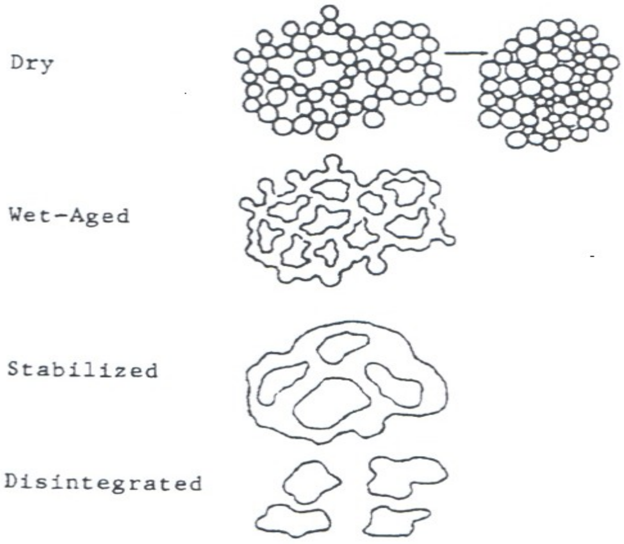

Figure 2.3.4. Illustration of the stages in aging process of gel [39].

2.4. Luminescence

Luminescence is defined as a phenomenon in which the electronic state of a substance is excited by some kind of external energy (physical or chemical) and the excitation energy is given off as light [45]. It can be divided into two types, phosphorescence and fluorescence. Phosphorescence is a luminescence process whereby the light emission from a substance continues for few seconds, minutes or hours after the exciting radiation has ceased, while fluorescence is a process in which emission stops suddenly after radiations have stopped [46]. There are many types of energy by which luminescence can be excited. Among them include a beam of photons (process called photoluminescence), an energetic beam of electrons (cathodoluminescence); a chemical energy resulting from a chemical reaction (chemiluminescence), an electric field through the specimen (electrolumiscence) and a biochemical enzyme-driven reaction with a light producing step (bioluminescence). Our study is mainly focused on cathodoluminescence for the field emission display (FED) and photoluminescence for a fundamental understanding of the phosphor, and so only the two processes will be discussed in more details.

2.4.1. Cathodoluminescence (CL)

Cathodoluminescence is defined as an optical and electrical phenomenon whereby a beam of high energy electrons is generated by an electron gun and then impacts on a luminescent material (phosphor), causing the material to emit visible light. The principal examples of cathodoluminescence are the screens of television, computer, radar, and oscilloscope displays. Cathodoluminescence occur because the impingement of a high energy electron beam onto a semiconductor will result in the promotion of electrons from valence band into the conduction band, leaving behind holes. When an electron and a hole recombine, it is possible for a photon to be emitted. The energy (colour) of the photon and the probability that a photon and not a phonon will be emitted results from the purity, and defect state of the material.

There are two possible types of collisions between energetic electrons and the material (phosphor), namely elastic and inelastic collisions. An elastic collision occurs between primary electrons and atoms of the target material. This collision type produces back scattered electrons, which suffer virtually no loss of energy. Inelastic collision involves electron-electron and electron-plasmon interactions. In these cases, a single primary electron undergoes rapid inelastic collision within a material. When an energetic electron is incident on a phosphor, a number of physical processes occur, which include emission of secondary electrons, Auger electrons and back scattered electrons. Hundreds of free electrons and free holes are produced along the path of the incident electron (primary electron).

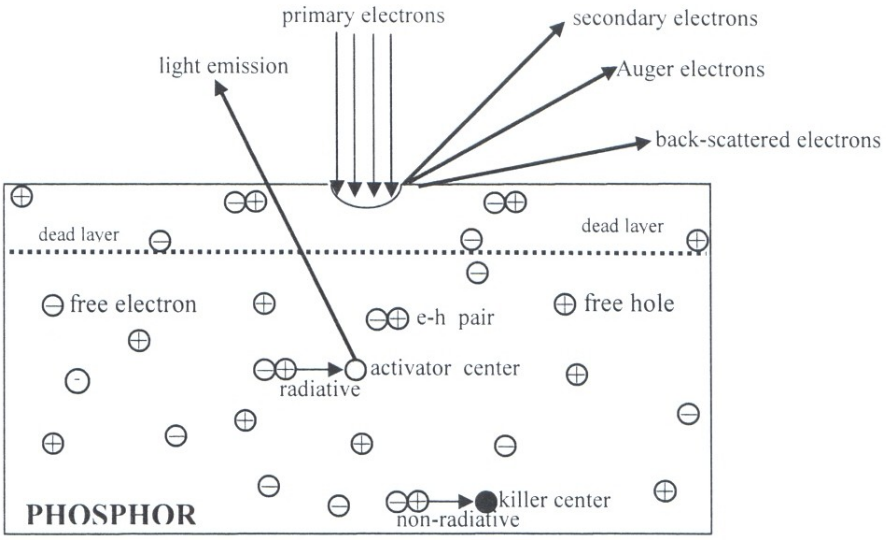

Figure 2.4.1. The CL process in a phosphor grain [47].

Illustrated in figure 2.4.1 are the free electrons and holes that couple and produce electron-hole (e-h) pairs. The e-h pairs can diffuse through the phosphor and transfer their energy to activate ions and subsequently emit light [47]. This process is referred to as radiative recombination. Unwanted process in which the e-h pairs recombine non-radiatively by transferring their energy to killer centers (incidental impurities and inherent lattice defects) is also possible. The e-h pair can also diffuse to the surface of the phosphor and recombine non-radiatively [47]. A thin dead (non-luminescent) layer may be formed on the surface.

2.4.2. Photoluminescence (PL)

Photoluminescence in solids is a process in which luminescence is stimulated by the interaction of photons (electromagnetic radiation) with a material. The process is divided into two major types, namely intrinsic and extrinsic photoluminescence [48]. Intrinsic photoluminescence is observed in materials which contain no impurity atoms. Extrinsic photoluminescence is caused by intentionally incorporated impurities and in most cases metallic impurities or defects [14,48].

2.4.3. Intrinsic photoluminescence

There are three kinds of intrinsic photoluminescence; namely band-to-band, exciton and cross-luminescence. Band-to-band results from the recombination of an electron in the conduction band with a hole in the valence band and can only be observed in a very pure crystals at relatively high temperatures [48]. An exciton is a composite particle of an excited electron and hole interacting with one another as discussed in section 2.2.1. Cross-luminescence is produced by the recombination of an electron in the valence band with a hole in the outermost core band. It can only take place when the energy difference between the top of the valence band and that of the outermost core band is smaller than the band-gap energy; otherwise, an Auger process occurs [48].

2.4.4. Extrinsic photoluminescence

Most of the observed types of luminescence that have practical applications belong to this category. Intentionally incorporated impurities are called activators and materials made luminescent in this way are called phosphors. Extrinsic luminescence is classified into two types, namely localized and delocalized luminescence. In a delocalized luminescence the excited electrons and holes of the host lattice participate in the luminescence process, while in a case of the localized luminescence the excitation and emission processes are confined in a localized luminescence center, the host lattice does not contribute to luminescence process [48].

2.4.5. Band-gap Transition Phosphors

When a phosphor is bombarded with an energetic electron (2 – 10 keV), free electrons and free holes are generated in the conduction and valence bands respectively. There are different models of electron transitions that result in luminescence as shown in figure 2.4.2. Figure 2.4.2(a) shows a direct recombination of free electrons and holes for a perfect (free from impurities and lattice defects) crystal [14,47]. Due to the presence of activator impurities, incidental impurities and lattice defects, a crystal is distorted and localized energy levels (impurity levels) in the band-gap are created. This provides effective recombination paths for the free electrons and holes as represented by (b), (c) and (d) in figure 2.4.2. The photon energy of these transitions is smaller than the band-gap in accordance with the impurity level.

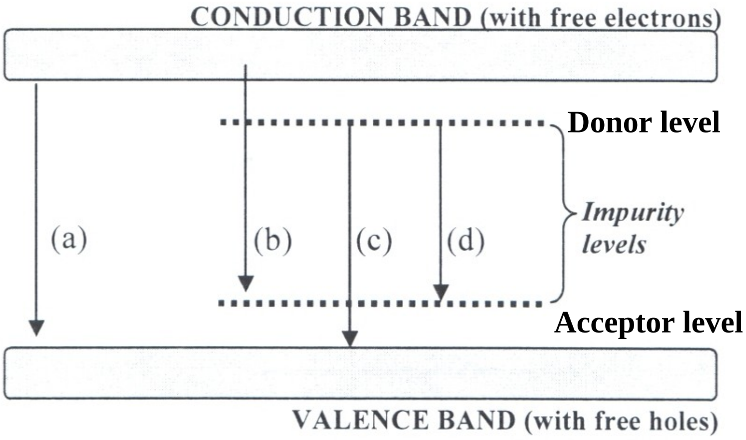

Figure 2.4.2. Models of cathodoluminescent transitions [47].

2.5. Cathodoluminescence degradation of phosphors

Degradation of the CL intensity of phosphors has been a subject of concern since the 1960s. It is defined as a reduction (quenching) of luminescence efficiency of phosphors during electron beam or photon bombardment. Different kinds of effects that contribute to the CL degradation will be dealt with in the following subsections. These are killers (incident impurities or lattice defects), concentration quenching and thermal quenching (an increase in temperature). Extensive research performed on the CL degradation of phosphors resulted in the proposal of Pfanhl's law [49] that describes the rate of degradation of CL intensity and development of an electron stimulated surface chemical reaction (ESSCR) model [47,51]. The Pfanhl's law is defined as;

$$I(N) = \frac{I_o}{\left(1 + CN)\right)} \ , \qquad 2.6$$

where I is the aged CL intensity, I_o is the initial CL intensity, N is the number of electrons per unit area and C is the burn parameter which is equal to the inverse of the number of electrons per unit area required to reduce the intensity to half its original value. This model predicts that the CL degradation is depended upon the type of gas in the vacuum, gas pressure, beam voltage and electron (coulombic) dose [50,47,51].

2.5.1. Killer effect

Killers are defects caused by incidental impurities (contamination) and inherent lattice defects that reduce the luminescence intensity of a phosphor [47,45]. The atoms and molecules adsorbed at the surface of the phosphor may reduce luminescence by producing a non-luminescent layer when they react with ambient vacuum species. Killers can affect the luminescence of phosphors in two different ways. They give rise to deep levels in the forbidden band which act as non-radiative recombination centres for free electrons in the conduction band and holes in the valence band, or the excitation energy absorbed by luminescent centres is transferred to killers without emitting radiation [47,51,52].

2.5.2. Concentration quenching

An increase in the concentration of activators and co-activators to obtain brighter phosphors may result in a reduction of light output due to concentration quenching. At high concentration, a fraction of the activators may change to killers because of the local field disturbance and induce the quenching effect due to resonance energy transfer [51,53]. This is clearly shown in figure 2.5.1 for $Ca_2MgSi_2O_7$: Eu^{2+} phosphor [54]. The emission intensity increase with the concentration of Eu^{2+} until it reached a critical quenching concentration (x_c) whereby the emission intensity begins to decrease. In this effect, excited activators are annihilated non-radiatively whereby their energy is transferred to unexcited activators, and electrons are raised into the conduction band. In this way, the excitation energy migrates in the lattice and is dissipated in non-radiative recombination traps [45]. It was also observed that the distance between active ions decrease with an increase in doping concentration, and when the distance is short enough (in the range of 1-2 nm), the interaction between active ions will occur and cause concentration quenching [55,56,57]. The concentration quenching may occur through the following channels: (i) cross-relaxation between active ions, (ii) the transference of active energy between ions and in the end transfer to the impurity ions, and then forming the quenching center, (iii) the interaction between active ions and host will transfer the energy to lattice defects and finally (iv) a lot of defects such as color centre, OH^- and other kinds of defects may trap energy and form the quenching centre [52,55].

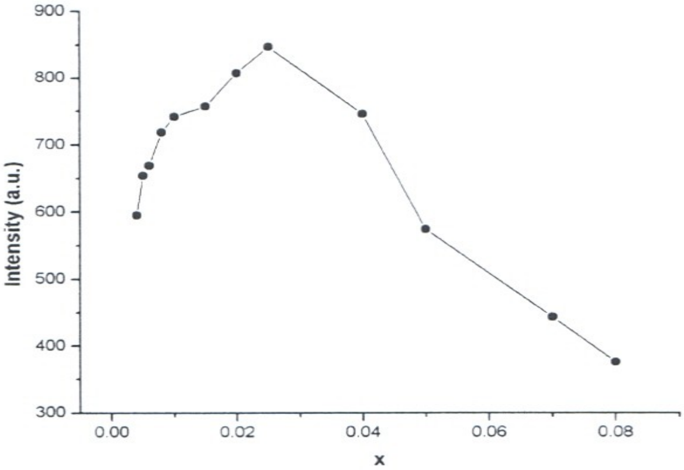

Figure 2.5.1. Emission intensity as a function of Eu^{2+} concentration (x) in $Ca_2MgSi_2O_7$: Eu^{2+} phosphor [54].

2.5.3. Thermal quenching

Thermal quenching refers to a decrease of luminescence efficiency of a centre due to the local heating by energetic electrons or photons. It occurs at high temperatures when thermal vibrations of atoms surrounding luminescent center transfer energy away from center resulting in a non-radiative recombination, and a subsequent depletion of the excess energy as phonons in the lattice [47]. The thermal quenching process is described in terms of configurational coordinate model of non-radiative relaxation processes in figure 2.5.2**.**

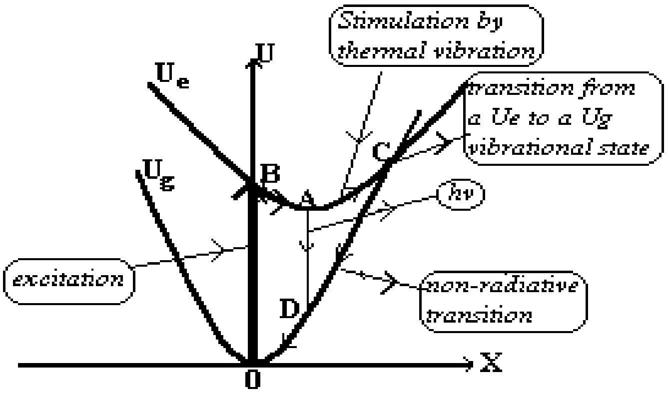

Figure 2.5.2. Configuration-coordinate model of luminescent centre [47,51].

In the diagram (figure 2.5.2) the energies of luminescent centres in the ground state and in the excited state are represented by U_g and U_e, respectively. With optical excitation, the system will undergo a vertical transition from ground state (point O) to the excited state (point B) and immediately adapts by changing the atomic configuration from B to the new equilibrium A along the curve U_e, with excess energy lost as heat. The system may undergo a radiative transition from A to D. This transition may be followed by the slower rearrangement of the atomic configuration from D to O along U_g with excess energy dissipated as heat. At higher temperatures, the luminescent center is thermally activated from point A, the point of the lowest energy on the excited state to the crossing point C where the electronic states of the excited and ground states are intermixed, and then thermally released from C to O on the ground state. The energy ε necessary to excite the center from A to C is called thermal activation energy. A probability that the centre will undergo non-radiative transition by thermal activation via point C is generally given by

$$W_{NR} = s\exp\left(\frac{-\varepsilon}{kT}\right) \tag{2.7}$$

where the activation energy ε is the difference of potential energy between the points A and *C*, *k* is the Boltzman's constant and *s* is a frequency factor. If W_R is the probability of radiative transition, the temperature dependence of the luminescence efficiency is given by

$$\eta = \frac{W_R}{W_R + W_{NR}} = \frac{W_R}{W_R + s\exp\left(\frac{-\varepsilon}{kT}\right)} \tag{2.8}$$

The efficiency always decreases with increasing temperature. Thus, at high temperatures, the non-radiative relaxation from A competes with a radiative transition from A to D, causing thermal quenching of emission [47,45,51].

2.5.4. Electron Stimulated Surface Chemical Reaction (ESSCR)

A mathematical model for the ZnS based phosphor was developed, and showed that the rate of removal of S from the surface of the powder phosphors correlates with the degradation of CL [50,47,51]. In this model, the concentration of *S* on the surface, C_s, can be expressed by a standard chemical rate equation:

$$\frac{dC_s}{dt} = -kC_s C_{as}^n, \tag{2.9}$$

where k is a chemical rate constant, C_{as}^n is the concentration of the adsorbed atomic species that will react with the ZnS, and n is the order of surface reaction. The first order surface reactions are assumed. The concentration of the adsorbed species on the surface, C_{as} can be expressed as:

$$C_{as} = N\phi_{ma}C_m J\tau_{as} \tag{2.10}$$

where Z is the number of reactive atomic species produced from the parent molecule, ϕ_{ma} is the dissociation cross section of the molecule to atoms, C_m is the surface concentration of the molecular species, J is the current density causing the dissociation, and τ_{as} is the lifetime of a reactive atomic species. C_m controls the rate of production of C_{as} and can be expressed as:

$$C_m = \sigma(\tau_o e^{Q/kT})(\frac{P_m}{\sqrt{2\pi mkT}}), \tag{2.11}$$

where σ is the molecular sticking coefficient, P_m is the partial pressure of the molecular gas in the vacuum, τ_o is the mean time between attempts by the adsorbed molecule to escape from the surface, Q is the energy required to desorb from the surface, k is the Boltzmann’s constant, m is the molecular mass, and T is absolute temperature. The first term in brackets is the molecular mean stay time on the surface, while the second term in brackets is the molecular flux onto the surface. Substituting (2.10) and (2.11) into (2.9) gives:

$$\frac{dC_s}{dt} = -k\sigma C_s N\phi_{ma} J\tau_{as}(\tau_o e^{Q/kT})(\frac{P_m}{\sqrt{2\pi mkT}}). \tag{2.12}$$

Equation (2.12) may be written as

$$\frac{dC_s}{C_s} = -KJP_m dt, \tag{2.13}$$

where K is defined by

$$K = k\sigma N\phi_{ma}\tau_{as}(\tau_o e^{Q/kT})(\sqrt{2\pi mkT}). \tag{2.14}$$

Integrating equation (2.13) with respect to time yields

$$C_s = C_s^0 e^{-KP_m Jt}, \tag{2.15}$$

where the boundary conditions C_s = C_s^0 at time equal to zero were applied. *Jt* is equal to charge per unit area or the electron dose, also known as coulomb dose [50,47]. This model predicts that the concentration of S will decrease exponentially with the coulomb dose, and the rate of loss will be larger at higher gas pressures. Since the C_s and the CL intensity are correlated, equation (2.15) can be written in terms of the CL intensity, I_{CL}, as

$$I_{CL} = I_{CL}^0 e^{-KP_m Jt} \tag{2.16}$$

The study of degradation of sulphide phosphors showed a direct correlation between the decrease of CL intensity and changes in the surface chemistry during prolonged exposure to a beam of electrons. The changes suggest that electron beam stimulated surface chemical reactions are taking place.

2.6. The thin film phosphors

Thin film technology is pervasive in many applications, including microelectronics, optics, magnetic, hard and corrosion resistant coatings, micro-mechanics, etc. This is the most desirable form of the powder phosphors for applications in many devices such as display technologies. By using thin film phosphors, debonding, outgassing and carbon contamination associated with phosphor powder (screens) can be eliminated [58]. The studies of semiconductor thin films grown on either glass or silicon substrates using spin coating [59], vacuum evaporation [60,61], sol-gel [62] or pulsed laser deposition [63] techniques have been reported. In many of these techniques, small clusters or atoms can move on the surface of the substrate, and upon meeting each other they form a larger cluster or a fractal structure depending on the temperature and materials properties [64]. As the movement takes place only on the substrate, all the constituents of the resulting structure are in contact with the substrate so that a 2D-like geometry results. The use of the film polycrystalline semiconductors has attracted much interest in an expanding variety of applications in various electronic and optoelectronic devices.

A growth mode called thermodynamic criterion was developed in order to understand the growth of the thin film on a substrate. The model is defined as

$$\Delta\sigma = \sigma_f + \sigma_i - \sigma_s, \qquad 2.15$$

where σ_s is the surface free energy of the substrate, σ_i is the free energy of the interface and σ_f is the surface free energy of the film [65]. If $\Delta\sigma \leq 0$, the adatoms are more strongly bound to the substrate than to each other and the film tends to extend on the substrate to minimize the total energy. If $\Delta\sigma \geq 0$, the atoms are more strongly bound to each other than to the substrate. In this case, the film energy may get a contribution from strain energy. It is reported that in most cases, growth occurs far from equilibrium such that it is strongly influenced by kinetic process. Growth of a film starts with the arrival of atoms from the target and then the impinging atoms lose enough energy thermally to stay on surface. If rebound is strong enough, atom escapes; otherwise the atom is trapped - oscillates and loses energy to lattice.

Due to the use of sensitive substrates (e.g. glass) and the temperature-sensitive phosphor materials, it is highly desirable that for any technique to work, good quality thin film phosphors can be deposited at low temperatures [66]. The low substrate temperature deposition is one particular advantage that helped pulsed laser deposition (PLD) to gain its wide spread acceptance [67]. Pulsed laser deposition (PLD) technique has been quiet successful in depositing complex materials such as superconducting oxide thin films and provides a unique process for stoichiometric evaporation of target materials. The PLD process of thin film formation on the substrate is shown in figure 2.6.1. This figure clearly shows the deposition process from the interaction of the laser with the target, the plume formation and finally the film formation on the substrate.

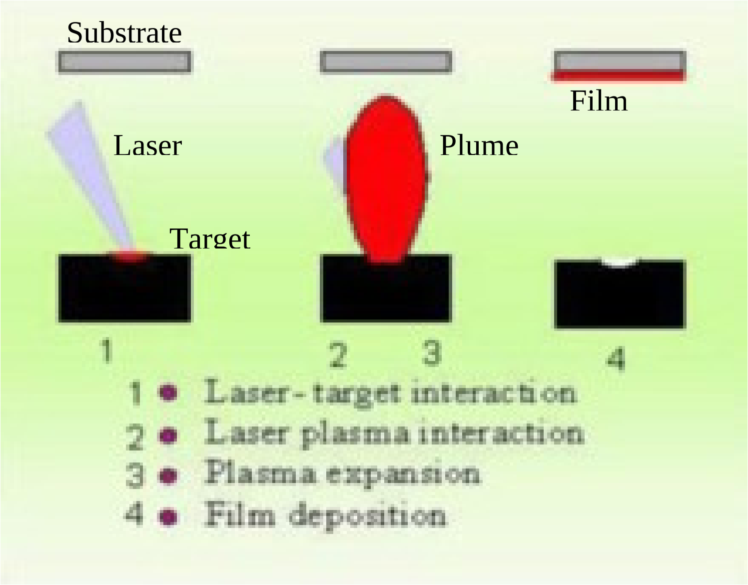

Figure 2.6.1. Summary of film formation by PLD system [68].

Recently, it has been observed that low-dimensional semiconductor materials, especially composites, have attracted much interest because of their valuable photoluminescence properties [63]. Thin films grown from this low-dimensional semiconductors have shown different behavior compared to the bulk semiconductor films due to size effects. Pulsed laser deposition (PLD) is a highly versatile technique for the growth of thin films and nanostructured materials [63]. However, it has been reported that the films grown by this technique showed less stress but more defects [69]. McKittrick et al [70] investigated the effects of substrate temperatures on the PL intensity of $(Y_{1-x}Eu_x)_2O_3$ thin films prepared by metallorganic chemical vapor deposition grown on sapphire. The results revealed that increasing the substrate temperatures increases the PL intensities of the emission spectrum. Post-deposition heat treatment (300 ^oC to 600 ^oC) showed an increase in the PL intensity with increase in annealing temperature as reported by Sagar et al [59]. Furthermore, they observed that the increase in annealing temperature causes the depletion of the grains which play a major role in increasing defects densities which lead to a drop in the PL intensity. In general, when the substrate temperature is increased or the deposit is annealed at higher temperature, the diffusion length increases and a more compact two-dimensional (2-D) island is formed [64]. Sintering and recrystallization of small primary particles into larger particles lead to a reduction in band gap as the quantum confinement decreases, eventually reaching almost the value of the bulk [64]. However, thin film phosphors are generally less bright than powder phosphors because an estimated 80% to 90% of light generated within the film is lost to internal reflection [47] and to the presence of defects in the film introduced during ablation [69]. The emission wavelength of the films grown from nanoparticles showed a red-shift due to band tail effect [61,71]. The presence of impurities in the material showed a band tail encroaching into the empty band gap leading to a band gap reduction of the semiconductor. Further red-shift of the emission wavelength of the films was observed with an increase in temperature due to sintering of small particles [1] which results in grain growth. The results lead to an increase in delocalization of electrons, and eventually a loss of quantum-size effect. The red-shift of band gap energy may originate from the residual stress due to the lattice distortion [59].

2.7. Energy transfer in nanoparticle phosphors

In order to improve the luminescence efficiency of the nanoparticle phosphors, a non-radiative energy transfer between semiconductor nanoparticles through the matrix was investigated. Energy transfer between donors and acceptors plays an important role in phosphors. The process involves two luminescent centers (D and A) separated by distance R, and requires a certain interaction between these centers. The interaction can be an exchange interaction, radiation reabsorption or multipole-multipole interaction [54]. Exchange interaction is responsible for the energy transfer for forbidden transitions and the critical transfer distance (R_c) is reported to be approximately twice the radius of a sphere with volume V as shown in figure 2.8.1;

$$R_c \approx 2\left(\frac{3V}{4\pi x_c N}\right)^{1/3}, \qquad 2.16$$

where x_c is the critical concentration and N is the Z ions in the unit cell [54]. The mechanism of radiation reabsorption comes into effect only when there is broad overlap of fluorescent spectra of the sensitizer and activator in the view of emission and excitation. Multipole-multipole interaction occurs when the distance between two ions is about 20 Å. Energy transfer can occur between a pair of identical centers or between two non-identical centers. In this study, the energy transfer between non-identical centers was evaluated.

The process of energy transfer between two non-identical centers, a sensitizer/energy donor (D) and energy acceptor (A) separated by a distance R in a phosphor is illustrated in figure 2.8.1. The rate of energy transfer (P_{DA}) between D and A is given by [72];

$$P_{DA} = \frac{2\pi}{\hbar}\left| < D, A^{*}\middle| H_{DA} \middle| D^{*}, A > \right|^{2} . \int g_{D}(E).g_{A}(E)dE, \tag{2.17}$$

where the matrix element represents the interaction between initial state $|D^{*}$, A> and the final state <D, $A^{*}|$. H_{DA} is the interaction Hamiltonian and D^{*} and A^{*} are excited states of D and A. The integral represents the spectral overlap between D emission and A absorption where $g_x(E)$ is the normalized optical line function of center x (x = D or A). D^{*} can decay to the ground state non-radiatively by transferring energy to A with a P_{DA} or radiatively with a rate P_D. The critical distance (R_c) for energy transfer is defined as the distance for which P_{DA} equals P_D. For $R>R_c$, radiative emission from D prevails, and energy transfer from D to A dominates for $R<R_c$ [47,72].

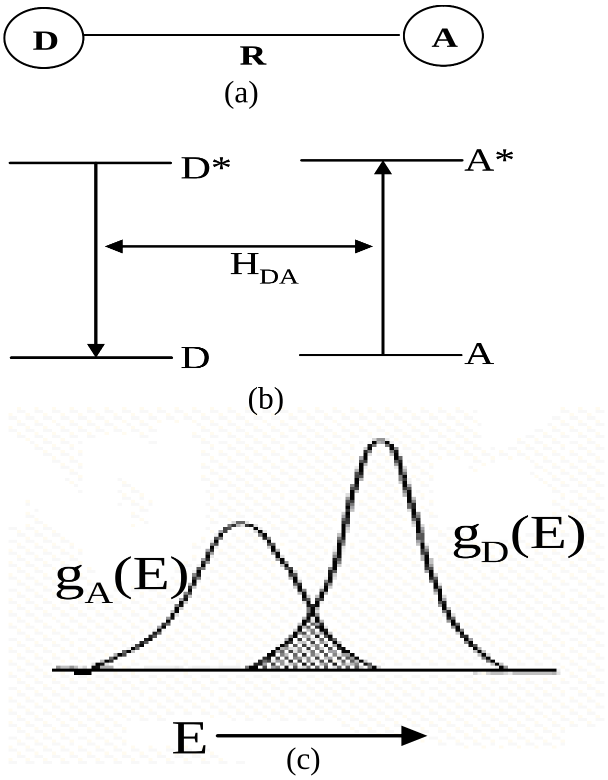

Figure 2.8.1. (a) Two centers D and A separated by a distance R, (b) energy transfer between D and A, and (c) the overlap between D emission and A absorption spectra [47].

References

[1] G. Hodes, A. Albu-Yaron, F. Decker and P. Motisuke, *Physical Review B*, **36** (8) (1987) 4215.

[2] L.Z. Yao, C.H. Ye, C.M. Mo, W.L. Cai, L.D. Zhang, *J. Crystal Growth*, **216** (2000) 149-150.

[3] B. Zhang, G. Li, J. Zhang, Y. Zhang, L. Zhang, *Nanotechnology*, **14** (2003) 443.

[4] R.K. Joshi, A. Kanjilal, H.K. Sehgal, *Nanotechnology*, **14** (2003) 809.

[5] I. Chakraborty, S.P. Moulik, *Journal of Nanoparticle Research*, **6** (2004) 233.

[6] Ring Surf: Nanotechnology Structures-Quantum Confinement, 2003-2007 http://www.ringsurf.com/.

[7] M.J. Fernee, A. Watt, J. Warner, N. Heckenberg, H. Rubinsztein-Dunlop, *Nanotechnology*, **15** (2004) 1328.

[8] M.J. Fernee, A. Watt, J. Warner, N. Heckenberg, H. Rubinsztein-Dunlop, *Nanotechnology*, **15** (2004) 1351.

[9] Semiconductor Physics: Density of States, http://britneyspears.ac/physics/dos/dos.htm

[10] Evident Technologies, August 14, http://www.evidenttech.com/qdot-definition/quantum-dot-introduction.php.

[11] A.L. Rogach, A. Eychmuller, S.G. Hickey, and S.V. Kershaw, *Small*, www.small-journal.com, 2007, **3** (4) 537.

[12] H. Tang, G. Xu, L. Weng, L. Pan, L. Wang, *Acta Materialia*, **52** (2004) 1489.

[13] K. Kang, K. Daneshvar, *Journal of Applied Physics*, **95** (9) (2004) 4747.

[14] H. Yang, Ph.D. dissertation, University of Florida, Florida, (2003).

[15] S. Glutsch, *Excitons in Low-Dimensional Semiconductors* (Springer:Berlin:New York, 2004).

[16] M.A. Omar, Elementary Solid State Physics, Addison-Wesley Publishing Company, Sydney, London, 1975.

[17] A. van Dijken, E.A. Meulenkamp, D. Vanmaekelbergh, A. Meijerink, *J. Lumin*, **90** (2000) 126.

[18] R.N. Bhargava, *J. Lumin*, **70** (1996) 85.

[19] L. Sun, C. Qian, C. Liao, X. Wang, C. Yan, *Solid State Communications*, **119** (2001) 395.

[20] J. Rama and R. Pino, Physical *Chemistry: Energy Band Theory and quantum Confinement*, Meliorum Technologies Inc., NY USA 14607, http://www.meliorum.com/Meliorum_Technol.

[21] L. Guo, Z. Wu, X. Ai, Q. Li, H. Zhu, S. Yang, *Optical Materials*, **14** (2000) 247.

[22] Z.L. Wang, *J. Phys. Chem. B*, **104** (2000) 1160.

[23] M.J. Fernee, A. Watt, J. Warner, S. Cooper, N. Heckenberg, H. Rubinsztein-Dunlop, *Nanotechnology*, **14** (2003) 991.

[24] J.H. Warner, A.R. Watt, M.J. Fernee, N.R. Heckenberg, H. Rubinsztein-Dunlop, *Nanotechnology*, **16** (2005) 479.

[25] M. Flores-Acosta, R. Perez-Salas, M. Sotelo-Lerma, F.F. Castillo-Barraza and R. Ramirez-Bon, *J. Materials Online*, **1** (2005) 2.

[26] M.J. Fernee, E. Thomsen, P. Jensen, H. Rubinsztein-Dunlop, *Nanotechnology*, **17** (2006) 956.

[27] Z. Zhang, J.C. Li, Q. Jiang, *J. Phys. D: Appl. Phys.*, **33** (2000) 2653.

[28] Q. Jiang, L.H. Liang, J.C. Li, *J. Phys.: Condens. Matter*, **13** (2001) 565.

[29] K.K. Nanda, *Applied Physics Letters*, **87** (2005) 021909-2.

[30] K.K. Nanda, S.N. Sahu, S.N. Behera, *Physics Review A*, **66** (2002) 013208-1.

[31] S.C. Tjong, H. Chen, *Materials Science and Engineering: Reports*, **45** (2004) 5.

[32] Y.J. Yang, L.Y. He, Q.F. Zhang, *Electrochemistry Communication*, **7** (2005) 361.

[33] R.S. Patil, C.D. Lokhande, R.S. Mane, T.P. Gujar, S-H. Han, *J. Non-Crystalline Solids*, **353** (2007) 1645.

[34] L. Sun, C. Qian, C. Liao, X. Wang, C. Yan, *Solid State Communications*, **119** (2001) 393.

[35] L.L. Beecroft, C.K. Ober, *Chem. Mater.*, **9**(6) (1997) 1312.

[36] R. Tamaki, Y. Chujo, *Appl. Organometal. Chem.*, **12** (1998) 755.

[37] Y. Zhang, J.M. Kim, D. Wu, Y. Sun, D. Zhao, S. Peng, *J. Non-Crystalline Solids*, **351** (2005) 777.

[38] L.C. Klein, *Ann. Rev. Mater. Sci.*, **15** (1985) 227.

[39] L.L. Hench, J.K. West, *Chem. Rev.*, **90** (1990) 33.

[40] P. Aragon-Santamaria, M.J. Santos-Delgado, A. Maceira-Vidan, L.M. Polo-Diez, *J. Mater. Chem.*, **1** (3) (1991) 409.

[41] A.C. Pierre, *Introduction to sol-gel processing*, Kluwer Academic Publishers, Boston, 1998.

[42] S. Criston, L. Armelao, E. Tondello, P. Traldi, *J. Mass Spectrom.*, **34** (1999) 1380.

[43] N. Yamanda, I. Yoshinaga, S. Katayama, *J. Sol-Gel Science and Technology*, **13** (1998) 445.

[44] K. Mauritz, Sol-Gel chemistry, http://www.psrc.usm.edu/mauritz/solgel.html.

[45] S. Shionoya, W.M. Yen, Phosphor Handbook, Phosphor Research Society, CRC Press.

[46] W. Wolf, H. Deubel, *P31 phosphor persistence at photonic mean luminance level*, **10** (4) (1997) 323.

[47] O.M. Ntwaeaborwa, Ph.D. dissertation, University of the Free State, South Africa (2006).

[48] D.R. Vij, Luminescence of Solids, Plenum Press, New York (1998) 95.

[49] A. Pfahnl, *Advances in electron tube techniques*, Pergamon, New York, (1961) 204

[50] P.H. Holloway, T.A. Trottier, J. Sebastian, S. Jones, X-M. Zhang, J-S. Bang, B. Abrams, W.J. Thomes and T-J. Kim, *J. Appl. Phys.*, **88** (2000) 1.

[51] K.T. Hillie, Ph.D. dissertation, University of the Free State, South Africa (2001).

[52] W.M. Yen, S. Shionoya, H. Yamamato, Phosphor handbook, 2nd edition, CRC Press.

[53] M. Garcia-Hipolito, R. Martinez, O. Alvarez-Fregoso, E. Martinez, C. Falcony, *J. Lumin*, **93** (2001) 13.

[54] L. Jiang, C. Chang, D. Mao, C. Feng, *Materials Science and Engineering* B**103**, (2003) 273.

[55] P. Yang, P. Deng, Z. Yin, *J. Lumin*, **97** (2002) 52.

[56] L. Jiang, C. Chang, D. Mao, C. Feng, *Materials Science and Engineering*, **B103** (2003) 272.

[57] D. Wang, Q. Yin, Y. Li, *Journal of Materials Science*, **37** (2002) 382

[58] R.K. Singh, Z. Chen, D. Kumar, K. Cho, M. Ollinger, *Applied Surface Science*, **197-198** (2002) 321.

[59] P. Sagar, P.K. Shishodia, R.M. Mehra, H. Okada, A. Wakahara, A. Yoshida, *J.*

Lumin., **126** (2007) 801.

[60] S. Kumar, T.P. Sharma, M. Zulfequar, M. Husain, *Physica B*, **325** (2003) 9

[61] H.Z. Wu, D.J. Qiu, Y.J. Cai, X.L. Xu, N.B. Chen, *Journal of Crystal Growth*, **245** (2002) 51.

[62] A. Martucci, J. Fick, Serge-Emile LeBlanc, M. LoCascio, A. Hache, *Journal of Non-Crystalline Solids*, **345 & 346** (2004) 639.

[62] D. Riabinina, F. Rosel, M. Chaker, *Journal of Experimental Nanoscience*, **1** (1) (2005) 83.

[64] K.K. Nanda, F.E. Kruis, H. Fissan, *Journal of Applied Physics*, **91** (4) (2002) 2315.

[65] J.M. Ngaruiya, Ph.D. dissertation, Aachen Technical University (RWTH), Aachen, Germany, 2004.

[66] V. Craciun, R.K. Singh, *Applied Surface Science*, **168** (2000) 239.

[67] X. W. Sun, H.S. Kwok, *Appl. Phys*. A, **69** [Suppl.] (1999) S39.

[68] Pulsed Laser Deposition and Epitaxy: www.geocities.com/afserghei/LVE.htm (2008).

[69] H. Misawa, S. Juodkazis, *3D Laser Microfabrication: Principles and Applications*, (2006) Wiley-VCH.

[70] J. McKittrick, C.F. Bacalski, G.A. Hirata, K.M. Hubbard, S.G. Pattillo, K.V. Salazar, M. Trkula, *J. Am. Ceram. Soc.*, **83** (5) (2000) 1241.

[71] S.K. O’Leary, S.R. Johnson, P.K. Lim, *J. Appl. Phys.*, **82** (7) (1997) 3334.

[72] G. Blasse and B.C. Grabmaier, Luminescent Materials, Springler-Verg, Berlin, 1994.

CHAPTER 3

EXPERIMENTAL RESEARCH TECHNIQUES

3.1. Introduction

In this chapter, a brief description of different surface techniques used in the characterization of the sol-gel SiO_2:PbS powder nano-phosphor and thin films is given. The techniques include Auger electron spectroscopy (AES), x-ray photoelectron spectroscopy (XPS), x-ray diffraction (XRD), transmission electron spectroscopy (TEM) and scanning electron spectroscopy (SEM). The pulsed laser deposition (PLD) technique was used in addition to grow thin luminescent films on the silicon (Si) substrates. The elemental composition on the surfaces of powder phosphors during electron or x-ray bombardment was monitored with AES, XPS and SEM-EDX. The TEM and SEM were used to obtain the morphological information of powder phosphors. SEM was also used to obtain the information about the surface morphology of the thin films. XRD and TEM were used to identify the crystalline phases and crystal sizes of the PbS nanoparticles. AES, Ocean Optics S2000 spectrometer and helium cadmium (He-Cd) and argon (Ar^+) lasers were used to measure the cathodoluminescence (CL) and photoluminescence (PL), respectively, of the powder and thin films.

3.2. AES system

Auger Electron Spectroscopy was developed in the late 1960’s, deriving its name from the effect first observed by Pierre Auger [1], a French Physicist, in the mid-1920’s. It is based on the measurement of the kinetic energies of the emitted Auger electrons. Auger electron spectroscopy, which is capable of identifying individual elements and with a shallow depth of about five monolayers from which data is taken, is particularly suited for surface analysis. In the Auger process, a high-energy (2-10 keV) primary electron hits and liberates a core level (e.g. K level) electron thereupon ionising the atom. The ionised atom that remains after the removal of the core hole electron is in a highly excited state and will rapidly relax back to a lower energy state. For this atom to reorganise itself to a lower energy state, an electron from the higher level (L_1 level) will drop to the lower level to fill the void caused by the liberated electron. The energy released in the transition is either emitted as a photon or transferred to another electron in the higher level (L_2 level). If the energy is sufficient, this electron can be ejected from the surface and detected as an Auger secondary electron. The emitted electron is known as a KLL electron [2]. The system can detect and analyze all elements with the exception of hydrogen (H) and helium (He) because they do not have electrons occupying the L level (have less than three electrons).

Due to the specific energy levels involved in the transition and the energy of the detected Auger electron, the atom from which the electron was ejected can be identified. Auger Spectroscopy can also be used for depth profiling with the use of an ion gun as part of the vacuum system. As the ion gun etches away the material, the electron probe focused on the same spot can give information about the composition of the surface layers with sputter depth. A detailed discussion of the Auger process can be obtained from other sources [1,3]. The PHI model 549 Auger spectrometer used in this study is shown in figure 3.1.

Figure 3.1. The PHI model 549 Auger spectrometer.

3.3. X-ray Photoelectron Spectroscopy

X-ray photoelectron spectroscopy (XPS), also known as electron spectroscopy for chemical analysis (ESCA), is a widely used surface technique to obtain chemical information at surfaces of different materials. It uses highly focused monochromatised x-rays to probe the material of interest. The XPS process involves the ejection of a photoelectron from the K level of an atom by x-rays in vacuum. The phenomenon is based on the photoelectric effect outlined by Einstein in 1905 where the concept of the photon was used to describe the ejection of electrons from a surface when photons impinge upon it [4]. The energy of the photo-emitted electrons is specific to the chemical state of the elements and compounds present, i.e. bound-state or multivalent states of individual elements can be differentiated [5]. Photoelectrons are collected and analyzed to produce a spectrum of emission intensity versus electron binding energy. The small spot capabilities allow one to obtain XPS information at 30-micron resolutions, making XPS chemical mapping and imaging a viable surface research tool [6]. XPS can easily analyze nonconductive samples with the system's charge neutralization. The basic components of a XPS spectrometer are an x-ray source, electron energy analyzer for the photoelectrons, and an electron detector. In this study, the Quantum model 2000 XPS spectrometer from the National Meteorology Institute of South Africa (NMISA) (see figure 3.2) was used.

Figure 3.2. Quantum 2000 scanning x-ray photoelectron spectrometer.

3.4. X-ray Diffraction

X-ray diffraction (XRD) is an efficient analytical non-destructive technique used to investigate structural properties of crystalline materials. It is also used in applications such as phase identification, determination of grain size, composition of solid solution, lattice constants, and degree of crystallinity in a mixture of amorphous and crystalline substances [7]. A diffraction pattern is produced when a material is irradiated with a collimated beam of x-rays. The x-ray spectra generated by this technique provide a structural fingerprint of the material (unknown). The relative peak height is generally proportional to the number of grains in a preferred orientation and peak positions are reproducible [7]. The intensity of the diffracted x-rays is measured as a function of diffraction angle 2θ and the specimen's orientation. The x-ray diffractometer used in this study is Philips SAM003A shown in figure 3.3, from the National Metrology Institute of South Africa (NMISA).

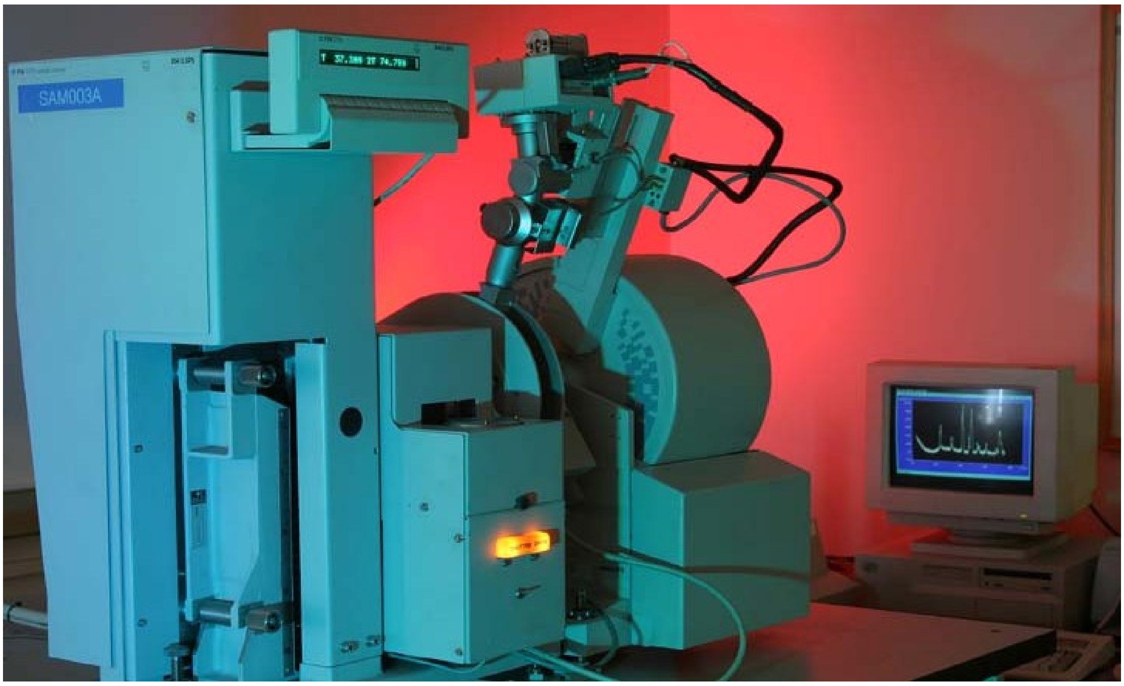

Figure 3.3. Philips SAM003A model x-ray diffractometer.

3.5. Transmission Electron Microscopy

Transmission electron microscopy (TEM) is an imaging technique whereby a beam of electrons is transmitted through a specimen, and then an image is formed. The image is then magnified and directed to appear either on a fluorescent screen or layer of photographic film, or to be detected by a sensor such as a CCD camera. The system can study small details in the cell or different materials down to near atomic levels [8,9]. It can investigate the size, shape and arrangement of the particles which make up the specimen as well as their relationship to each other on the scale of atomic diameters. Materials to be analyzed with this technique need to have dimensions small enough to be electron transparent and that can be produced by the deposition of a dilute sample containing the specimen onto support grids. The suspension is normally a volatile solvent such as ethanol, ensuring that the solvent rapidly evaporates allowing a sample that can be rapidly analyzed.

The possibility for high magnifications has made the TEM a valuable tool in medical, biological and material sciences research. In all cases, the specimens must be very thin and able to withstand the high vacuum present inside the instrument. For biological specimens, the maximum specimen thickness is roughly 1 micrometer [9]. To withstand the instrument vacuum, biological specimens are held at liquid nitrogen temperatures. In material science/metallurgy the specimens tend to be naturally resistant to vacuum and must be prepared as a thin foil, or etched so that some portion of the specimen is thin enough for the beam to penetrate.

The system can also be used for the determination of the electron diffraction patterns of the crystalline structures. A crystalline material interacts with the electron beam mostly by diffraction rather than absorption. The intensity of the transmitted beam is affected by the volume and density of the material through which it passes. The intensity of the diffraction depends on the orientation of the planes of atoms in a crystal relative to the electron beam. At certain angles the electron beam is diffracted strongly from the axis of the incoming beam, while at other angles the beam is largely transmitted. In this study, the TEM images of PbS nanoparticles were obtained using a Philips CM 100 Transmission Electron Microscopy, shown in figure 3.4.

Figure 3.4. The PHILIPS CM 100 model Transmission Electron Microscope.

3.6. Scanning Electron Microscopy (SEM)

Scanning electron microscopy (SEM) is a technique whereby a beam of energetically well-defined and highly focused electrons is scanned across a material (sample). The microscope uses a lanthanum hexaboride (LaB_6) source and is pumped using turbo and ion pumps to maintain the highest possible vacuum. The technique can provide material's (only conducting and semiconducting) information about topography, morphology and crystallography [10]. If the system is equipped with energy dispersive x-ray spectrometer (EDS), it can also provide information about chemical composition of the material [11].

The basic principle of the system is that, the electron beam impinges the surface and generates a splash of electrons with kinetic energies much lower than the primary incident electrons called secondary electrons. An image of the sample surface is constructed by measuring the secondary electron intensity as a function of the primary beam position. The SEM has many advantages over traditional microscopes. It has a large depth of field, which allows more of a specimen to be in focus at one time. The SEM also has much higher resolution, so closely spaced specimens can be magnified at much higher levels. Because the SEM uses electromagnetic lenses, the researcher has much more control in the degree of magnification. All of these advantages, as well as the actual strikingly clear images, make the scanning electron microscope one of the most useful instruments in research today [12]. A simplified layout of a SEM is shown in figure 3.5.

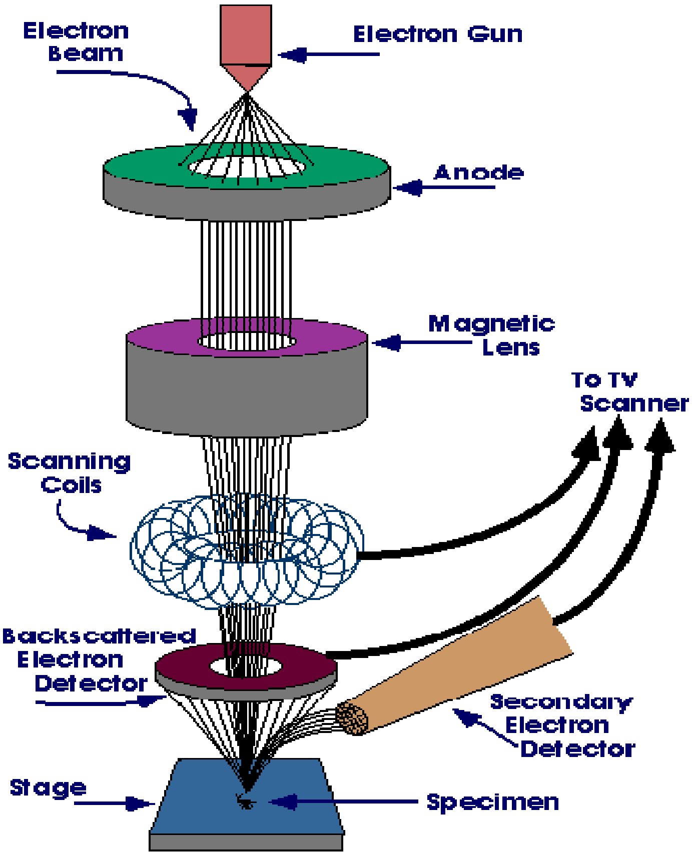

Figure 3.5. A simplified layout of a SEM [12].

The SEM images of powder and thin film samples in this study were obtained using Gemini Leo-Field Emission Scanning Electron Microscope model 1525 in figure 3.6 from the NMISA.

Figure 3.6. Gemini Leo-Field 1525 model Scanning Electron Microscope.

3.7. Pulsed Laser Deposition (PLD)

Pulsed laser deposition (PLD) is an extremely versatile technique for preparing a large variety of thin films and multilayer structures. The system involves ablation of a solid target in a high vacuum chamber; either in vacuum or in the presence of some background gas (i.e. O_2, N_2 etc.) by means of laser pulses [13]. In this technique, a pulsed laser beam is directed at a solid target and its interaction with the target produces a broad plume of the target material that is ablated on a heated substrate (usually silicon) placed directly in the line of the plume. Particles ejected from the target material, which have trajectories generally parallel to the propagation direction of the plume, are too heavy to have significant lateral diffusion and have little chance of lodging on the deposition surface. The substrate may be rotated about an axis perpendicular to the deposition surface (generally perpendicular to the propagation direction of the plume) to provide uniform deposition over the entire surface [13]. The main advantage of the PLD technique is its simplicity and low cost, and the possibility to obtain uniform films with good adherence and reproducibility [14]. Nanoseconds pulsed lasers, particularly excimers, are currently the standard used in PLD [15]. Of the excimer lasers, KrF and XeCl have been extensively used for PLD. Figure 3.7 shows an example of a laser plume during ablation.

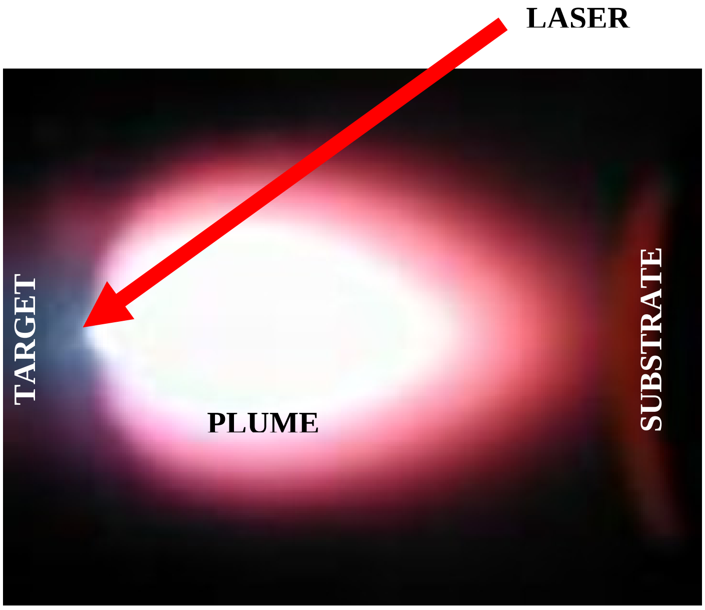

Figure 3.7. Laser plume during deposition [16].

The technique chamber can load multiple targets on a rotating holder and sequentially exposed to the pulsed laser beam, and thereby enabling the in-situ growth of heterostructures and superlattices with relatively clean interfaces [17]. The technique is known to have a number of advantages over conventional thin-film deposition techniques [such as molecular beam epitaxy (MBE), MOCVD, thermal evaporation (TE), chemical vapour deposition, metalorganic vapor-phase epitaxy (MOVPE), photochemical deposition (PD), electro deposition, chemical bath deposition (CBD) and spray pyrolysis (SP)], which include cost-effectiveness, stoichiometric transfer, inherent simplicity for the growth of multilayered structures, congruent transfer between the target and the deposited film, small target size and clean deposition due to the absence of atmospheric gas [14,17,18]. The LP Excimer laser (KrF) PLD system used in this study, figure 3.8, was from the National Laser Centre (NLC), CSIR.

Figure 3.8. PLD, LP Excimer laser (KrF), system for growing thin solid films.

3.8. Hellium-Cadnium (He-Cd) and Argon (Ar^+) lasers

The Helium-Cadmium (He-Cd) laser is one of a class of gas lasers using helium in conjunction with a metal which vaporizes at a relatively low temperature. A typical construction for the He-Cd laser is in the form of a tube, terminated by two Brewster's angle windows, with the two laser mirrors mounted separated from the tube. The tube filled with helium, also has a reservoir containing the Cd and a heater to vaporize the metal [19]. The reservoir is raised to a high enough temperature (~250 ^oC) to produce the desired vapor of Cd atoms in the tube. He-Cd lasers can give output powers of 50 – 100 mW and it can produce a high quality beam at 442 nm (violet-blue) and/or 325 nm (UV) depending on the optics [19]. A schematic drawing of the He-Cd laser equipment for photoluminescence is shown in figure 3.9.

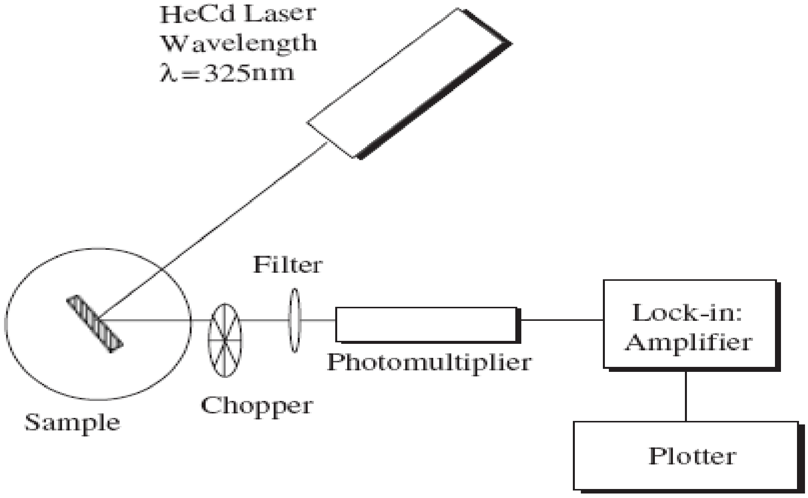

Figure 3.9. A schematic drawing of the He-Cd laser equipment for photoluminescence [20].

Argon laser is one of a family of ion (ionized argon) lasers that use a noble gas as the active medium. This laser is used in many applications such as; forensic medicine, entertainment, general surgery, and ophthalmic surgery etc. Argon lasers emit at several wavelengths through the visible and ultraviolet spectrum: 351 nm, 454.6 nm, 457.9 nm, 465.8 nm, 476.5 nm, 488.0 nm, 496.5 nm, 501.7 nm, 514.5 nm, 528.7 nm [21]. Unlike He-Cd lasers, the energy level transitions that contribute to laser action come from ions. Because of the large amount of energy required to excite the ionic transitions in ion lasers, the required current is much greater [22]. The He-Cd (325 nm)/Ar^+ (458 nm) laser system used in this study, shown in figure 3.10, was from the Nelson Mandela Metropolitan University (NMMU) of South Africa.

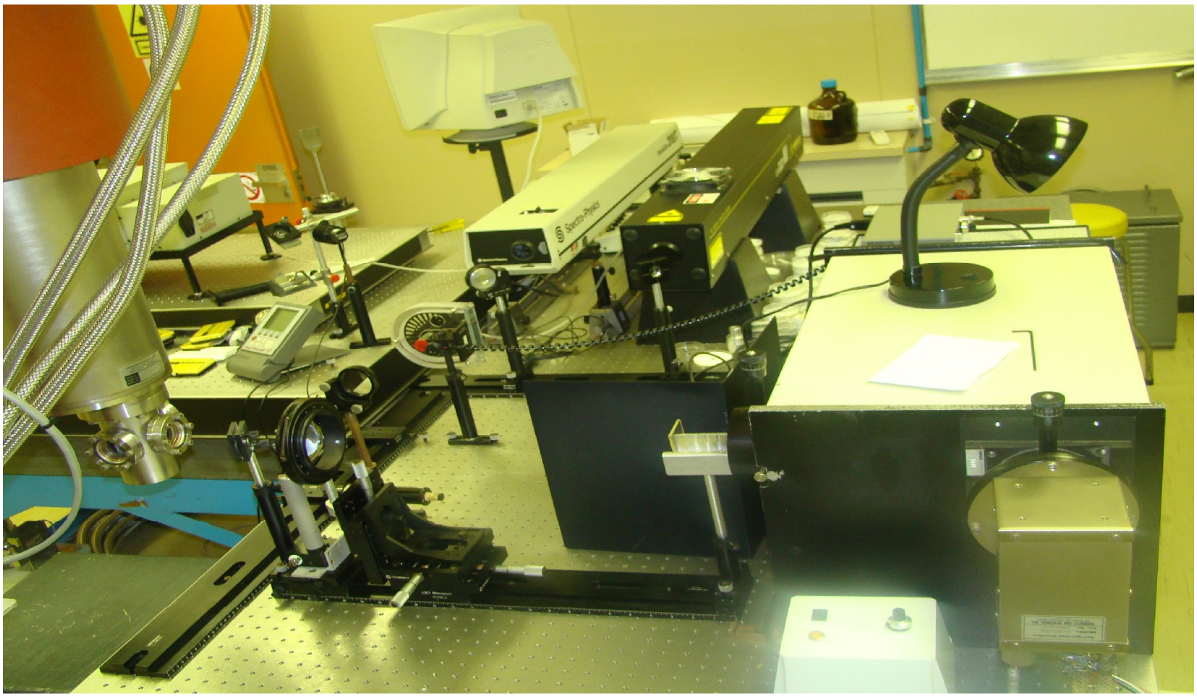

Figure 3.10. He-Cd (325 nm)/Ar$^+$ (458 nm) laser for photoluminescence.

References

[1] D. Briggs, and J.T. Grant, Surface Analysis by AES and XPS, IM Publications, Chichesteter, England, (1998).

[2] Silicon FarEast: http://www.siliconfareast.com/augeranalysis.htm, 2008

[3] J.M. Walls (Ed.), Methods of surface analysis: Techniques and applications, Cambridge University Press.

[4] UK Surface Analysis Forum: XPS: http://www.uksaf.org/tech/xps.html 2008.

[5] X-ray photoelectron Spectroscopy: http://www.chem.qmul.ac.uk/surfaces/scc/scat5_3.htm 2008.

[6] P. Dunn**,** R. Schulze, M. Paffett, Materials Science and Technology Division Facility Focus**:** http://www.lanl.gov/orgs/mst/files/facilities/LALP-07-018.pdf. 2007.

[7] G. Cao, Nanostructures and Nanomaterials: Synthesis, Properties & Applications, 6th edition, London, 2004.

[8] Z.L. Wang, Y. Liu, Z. Zhang, Handbook of nanophase and nanostructured materials, 4th edition, New York, 2003.

[9] Transmission Electron Microscopy: http://en.wikipedia.org/wiki/Transmission_Electron_Microscopy, 22 January 2008.

[10] University of Nebrasaka-Lncon:http://www.unl.edu/CMRAcfem/semoptic.htm.

[11] Binghamton University: Nanotechnology for undergraduate education: http://nue.clt.binghamton.edu/semtem.html.

[12]. J. Schweitzer, Radiological and Environmental Management (REM): http://www.purdue.edu/REM/rs/sem.htm 2008.

[13] J.T. Cheung, *Method of laser ablation for uniform thin film deposition*, US Patent (1995).

[14] X.L. Tong, D.S. Jiang, W.B. Hu, Z.M. Liu, M.Z. Luo, Appl. Phys., **A 84**, (2006) 143.

[15] J. Reilly, C. Allmond, S. Watson, J. Gammon, J.G. Kim, *J. Appl. Phys.*, **93** (5) (2003) 3098.

[16] Carnegie Mellon University, Materials Science and Engineering: neon.materials.cmu.edu/salvador/researchgroupS00.html

[17] O.M. Ntwaeaborwa, Ph.D. dissertation, University of the Free State, South Africa (2006).

[18] T. Yoshitake, G. Shiraishi, K. Nagayama, *Applied Surface Science*, **197-198** (2002) 379.

[19] O. Svelto, Principles of lasers, 4th edition, Springer, New York, 1998.

[20] T. Katsumata, S. Toyomane, R. Sakai, S. Komuro, T. Morikawa, J. Am. Ceram. Soc., **89** (3) (2006) 932.

[21] P.J. Vinken, G.W. Bruyn, Neuro-oncology, Elsevier Health Sciences, Revised series 23, Amsterdam, 1997.

[22] W. Thomas Silfvast, Laser fundamentals, 2nd edition, Cambridge University Press, Florida, 2004.

CHAPTER 4

SOL - GEL PREPARATION OF PbS NANOPARTICLES INCORPORATED IN SiO_2 MATRIX

4.1. Introduction

A strong interest has been posted in studying the preparation and properties of transparent media in which semiconductor nanocrystals are dispersed. Their potential applications in the optical, photonic devices [1] electro-optical field have turned them into very attractive materials [2,3]. Useful devices based on PbS quantum dots doped glasses have not been fully developed. This is mostly attributed to the observed broad size distribution of the dots, high concentration of many vacancies, substitution defects, and low dot concentrations. Thus, further improvements on the fabrication of QDs embedded in glass matrices are required.

Previously sol-gel process has been used to prepare a variety of materials ranging from inorganic ceramics to glass. This chapter presents a general idea of synthesis of SiO_2 doped with lead sulphide (PbS) nanophosphor. The samples were characterized by XRD, AES, XPS, SEM-EDS and TEM.

4.2. Preparation of SiO_2:PbS nanoparticle phosphor

SiO_2:PbS gel was prepared by mixing 10 g of tetraethylorthosilicate (TEOS) solution, 5 g of ethanol (EtOH), and 5 g of 0.15 M nitric acid (HNO_3). The mixture was stirred at room temperature for 1 hour. The resulting solution (transparent) was mixed with 0.03 g of $Pb(CH_3COO)_2.3H_2O$ dissolved in 5 g of ethanol and 0.01 g of Na_2S dissolved in 5 g of ethanol, and stirred further for 30 minutes. The gels were allowed to dry at room temperature for ~10 days, crushed into powders and annealed in air at 200 °C for 2 hours. The overall equation for the formation of PbS from the solution of $Pb(CH_3COO)_2.3H_2O$ and Na_2S is shown;

$$Pb(CH_3COO)_2.3H_2O + Na_2S \rightarrow PbS + 2Na^+ + 2CH_3COO^- + 3H_2O(\uparrow).$$

Figure 4.1 shows a flow diagram for the preparation of SiO_2:PbS.

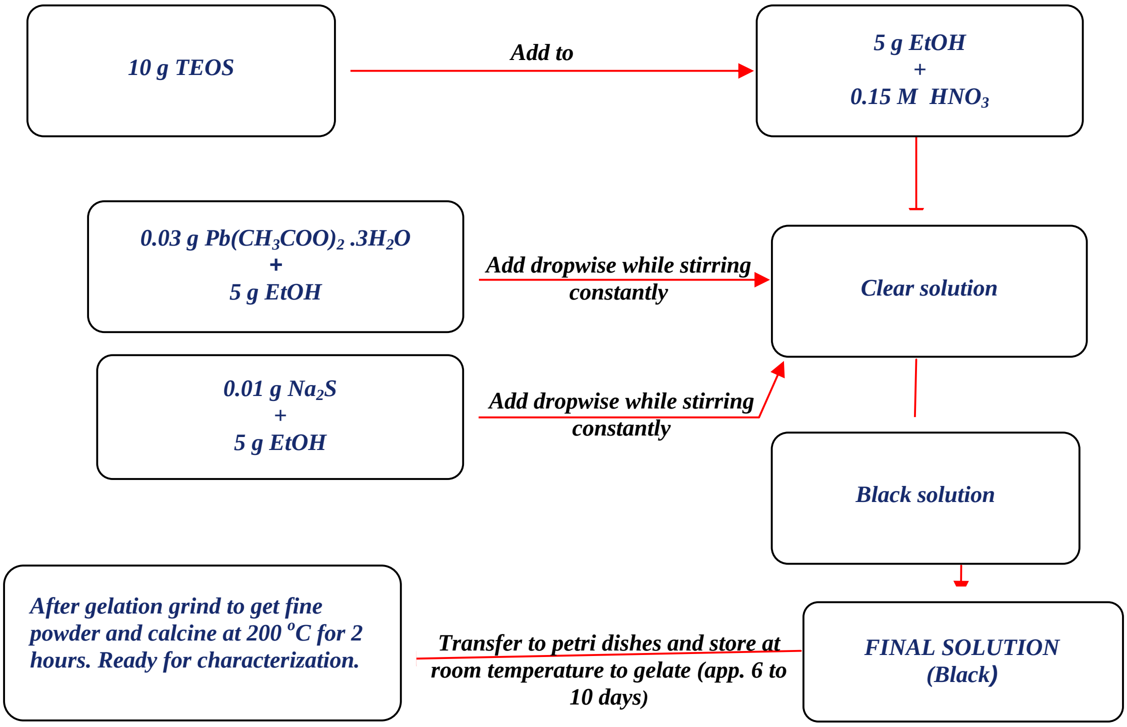

Figure 4.1. Preparation of SiO_2:PbS nanoparticle phosphors by the sol-gel process.

4.3. Characterization

Crystallization of the lead sulphide (PbS) in the amorphous SiO_2 matrix is apparent from the XRD spectrum shown in Figure 4.2. The five diffraction peaks of PbS shown correspond to the <111>, <200>, <220>, <311> and <222> planes of the cubic phase. In order to subtract the background due to the amorphous SiO_2 from the XRD spectrum, a least squares fit of the form [4]

$$f\left(x\right)=\sum_{i=1}^{D}C_i x^{i-1} \tag{1.1}$$

was performed on the XRD data, where D is the degree of curve fit, C_i is the curve fit coefficient and x is the value at which the fit is required. A degree of curve fit of 20 was found to be the best fit for the amorphous SiO_2 XRD peak data. Figure 4.3 shows the five diffraction peaks of PbS after the removal of the background contribution of the amorphous SiO_2. The results showed in figures 4.2 and 4.3 show broader peak widths of the PbS nanoparticles compared to the bulk PbS. The broadening of the peaks is attributed to small crystallites or nanocrystalline nature of the powder (particle size effect). The Debye-Scherrer's equation [5]:

$$d=\frac{k\lambda}{\beta\ \cos\theta} \tag{1.2}$$

was used to determine the average size (*d)* of the PbS nanoparticles with β the full-width-at-half-maximum of the diffraction peaks, k is the shape factor, taken as 0.89 and λ_{Cu} is the X-ray wavelength (0.154 nm). The nanocrystallite size as calculated from the broadening of the XRD peaks obtained from the powder was 16 ± 2 nm in diameter. Possibly observe that no double peak was expected at <111> and this may be attributed to the system noise level. The XRD parameters of the PbS nanoparticles compare very well with those of the standard PbS (Galena), as shown in table 1.

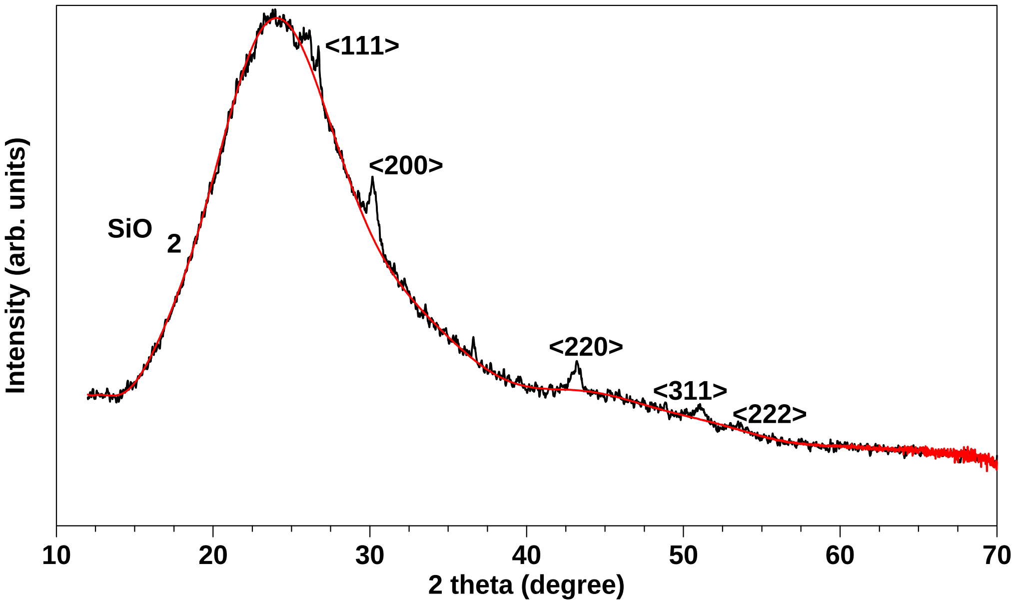

Figure 4.2. XRD patterns of PbS nanoparticles embedded in SiO_2 by the sol-gel process.

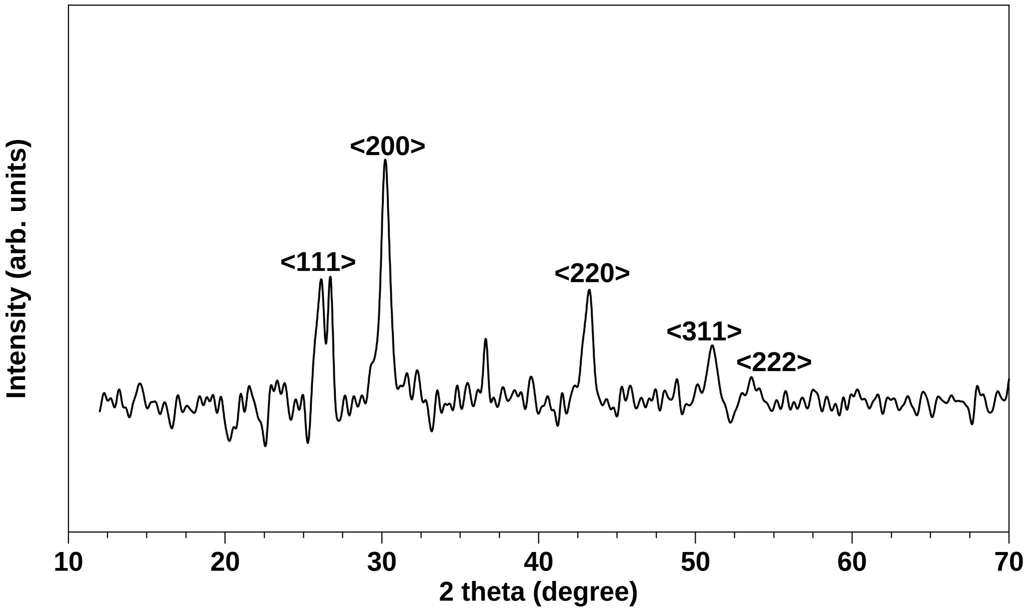

Figure 4.3. XRD patterns of PbS nanoparticles after the removal of the background amorphous SiO_2.

hkl	**d (Å)**	**2θ (degree) theoretical**	**2θ (degree) experimental**
(111)	3.44	25.9	26.0
(200)	2.98	29.9	30.0
(220)	2.11	42.8	43.0
(311)	1.80	50.7	51.0
(222)	1.72	53.2	53.0

Table 1. XRD parameters of PbS nanoparticles in SiO_2 matrix compared to those of PbS (Galena) standard structure.

Figure 4.5 shows the AES spectrum of SiO_2:PbS with characteristic Auger peaks of Si at 78 eV and O_2 at 506 eV. The Si peak in the compound (SiO_2) is known to be in the range of 70 – 80 eV and the shift from the normally high energy Si (92 eV) peak of the element (Si) to a low energy is attributed to the change in the density of state in the valence band and relaxation effects [1]. The AES could not detect Pb^+ and S^- ions probably due to their relatively low concentration in the SiO_2 matrix.

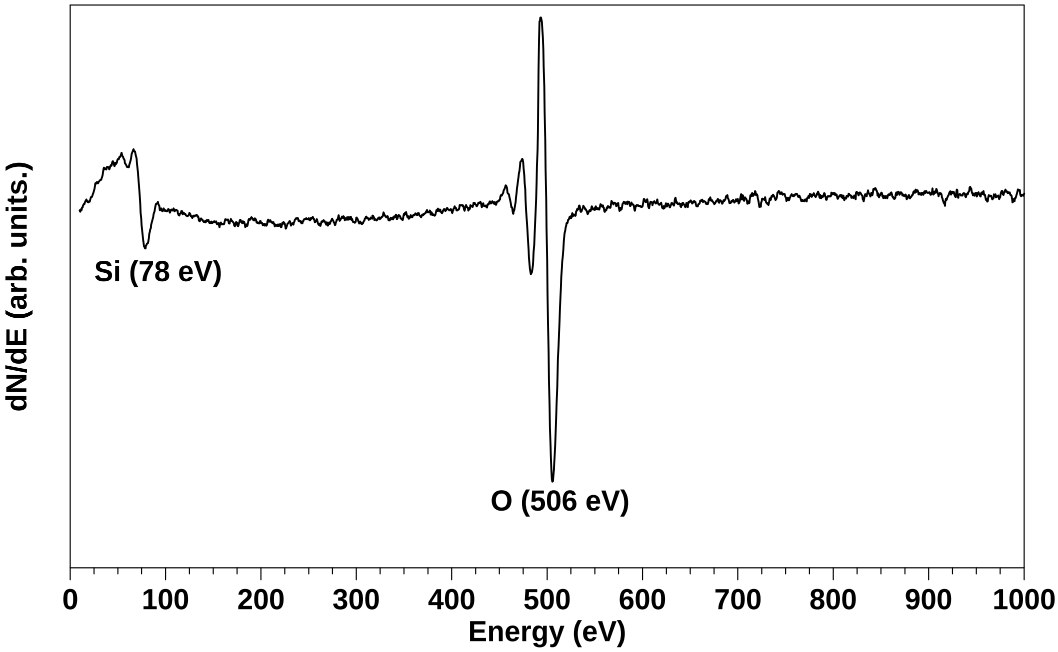

Figure 4.5. AES spectrum from the annealed SiO_2:PbS (0.134 mol%PbS) powder phosphor.

The XPS spectrum of the annealed SiO_2:PbS powder is shown in figure 4.6. The spectrum shows the presence of O, Si and adventitious C on the surface. Pb^+ and S^- ions could not be detected by the XPS and this is also ascribed to their relatively low concentration in the matrix, as in the case of AES.

SEM image of the as prepared SiO_2:PbS powder sample is shown in figure 4.7. The image shows multi-facets of agglomerated composite-particles with nano-sized particles on the surface. It is clear that most of the particles were micron sized.

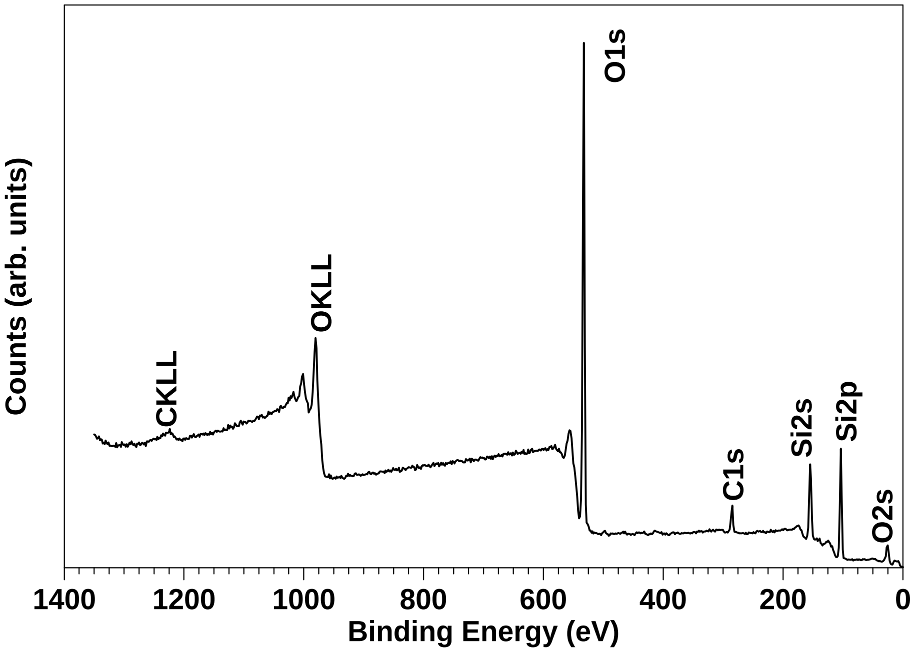

Figure 4.6. XPS spectrum of the annealed SiO_2:PbS (0.134mol%PbS) powder phosphor.

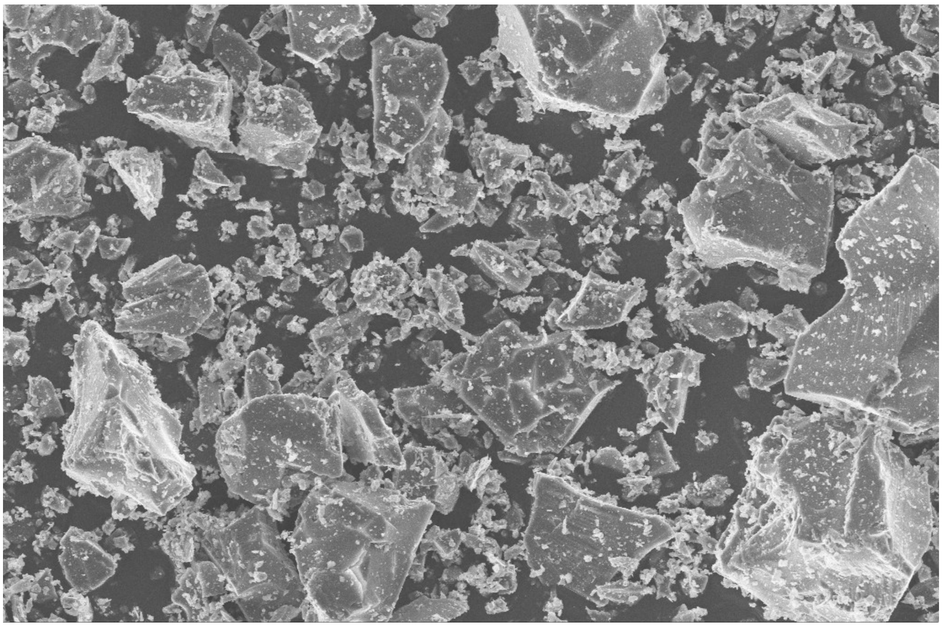

Scale 10 µm

Figure 4.7. The SEM photograph of the annealed SiO_2:PbS powder phosphor.

A TEM image of the PbS nanoparticles in SiO_2 suspended in ethanol and dried on a Cu-grid is shown in Figure 4.8. The black spots in the image are the PbS nanoparticles, in a SiO_2 particle, as confirmed by the electron diffraction pattern in Figure 4.10. The "white" area is due to an optical effect from the SiO_2 particle that was studied with the TEM. It is, however, clear from the pictures that some of the larger particles are made up of agglomeration of smaller particles, which makes it difficult to determine a mean particle size. Most of the particles were in the order of 17 nm, but there were also smaller (10 nm) and bigger agglomerated particles (up to 50 nm), as indicated by the particle size distribution. The measurements show that the particle size distribution is relatively broad (in the range of 10 to 50 nm). Most of the particles were slightly smaller than the exciton Bohr diameter of PbS [6]. The polyhedron shape of the PbS nanoparticles is also clear on some of the particles on the TEM image.

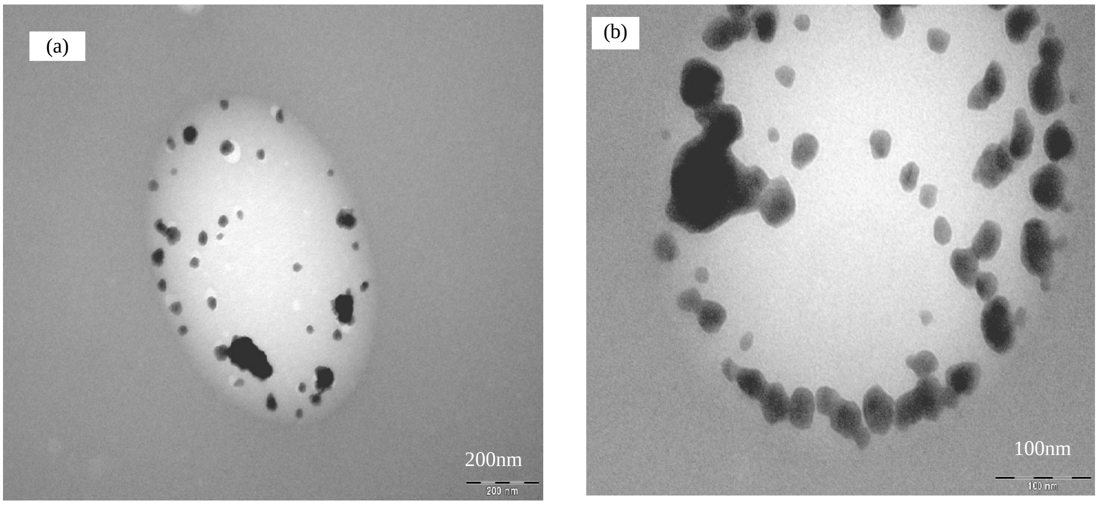

Figure 4.8. TEM images of PbS nanoparticles in a SiO_2 matrix at different magnifications.

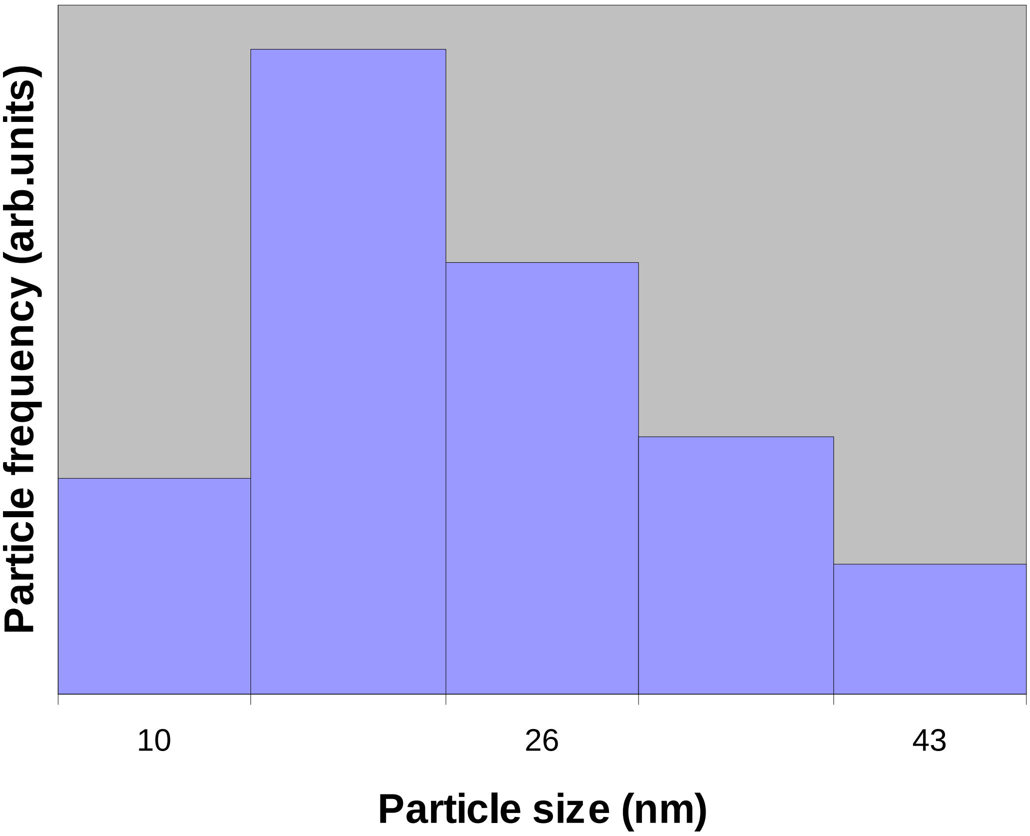

Figure 4.9. Particle size distribution obtained from several TEM images in Figure 4.8.

The electron diffraction pattern as shown in figure 4.10 was used for the determination of the crystalline structure of the nanoparticles and therefore for their classification. In this pattern, the bright spots are due to the electron diffraction from the PbS crystalline planes. The calculated interplanar distances of the nanoparticle crystalline lattice are given in Table 2 together with the standard PbS (Galena) crystalline structure [7]. The calculated values of the interplanar distances of the nanoparticles crystalline lattice and those of the Galena structure are in good agreement and therefore it can be concluded that the nanoparticles embedded in SiO_2 observed in the TEM image are PbS crystalline nanoparticles with a cubic structure. EDS on the as prepared powder sample confirmed the existence of PbS in the SiO_2 matrix as shown in figure 4.11.

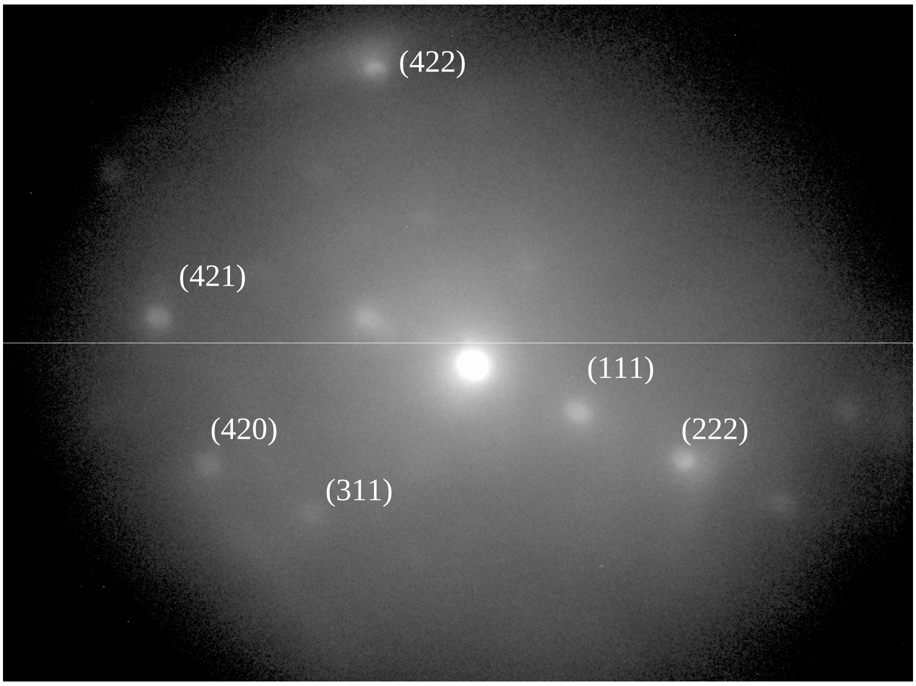

Figure 4.10. Electron diffraction pattern of the PbS.

Crystalline plane (hkl)	Interplanar distance (d) of PbS in SiO_2 (Å)	Interplanar distance (d) PbS (Galena) (Å)
(111)	3.32	3.44
(311)	1.74	1.80
(222)	1.66	1.72
(420)	1.32	1.33
(422)	1.18	1.22

Table 2. Calculated interplanar distances of PbS nanoparticles compared to those of PbS bulk standard (Galena) structure [7], with a = 5.9524 Å ($d = \frac{a}{\sqrt{h^2 + k^2 + l^2}}$), and their corresponding crystalline lattice planes.

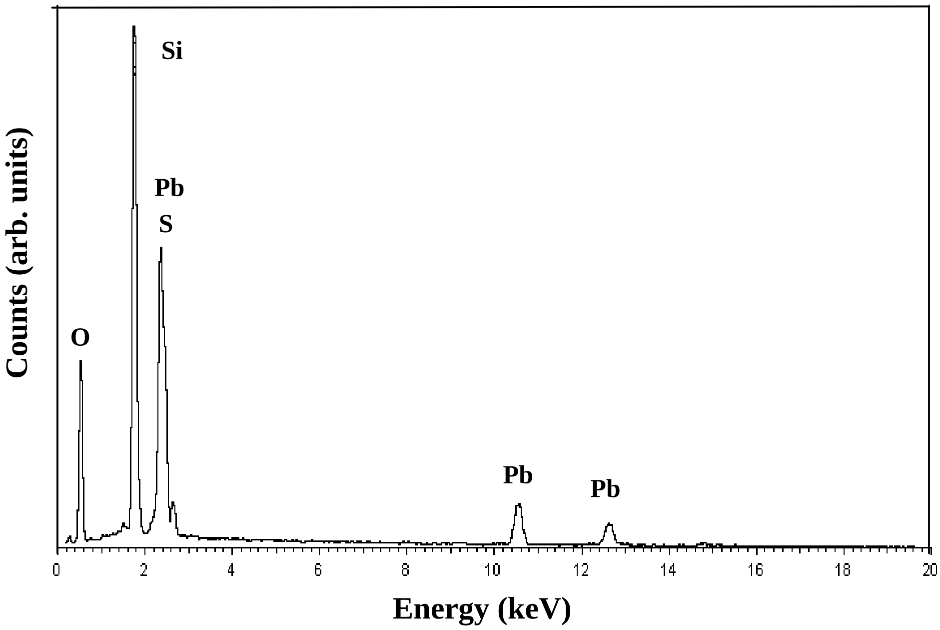

Figure 4.11. EDS spectrum for chemical composition of the as prepared SiO_2:PbS powder sample.

4.4. Conclusion

Luminescent polyhedron PbS nanoparticles with sizes ranging from 10 to 50 nm inside the SiO_2 matrix were successfully synthesized. X-ray and electron diffraction patterns confirmed the cubic crystal structure of the PbS particles. Broader peak widths of the PbS nanoparticles due to size effect were observed. Chemical composition analysis confirmed the existence of the PbS in the SiO_2 matrix.

References

[1] D. Riabinina, F. Rosei, M. Chaker, *Journal of Engineering Nanoscience*, **1** (1) (2005) 83.

[2] R. K. Joshi, A. Kanjilal and H. K. Sehgal, *Nanotechnology*, **14** (2003) 809.

[3] A. Martucci, J. Fick, Serge-Emile LeBlanc, M. LoCascio, A. Hache, *Journal of Non-Crystalline Solids*, **345 & 346** (2004) 639.

[4] F.R. Ruckdeschel, *BASIC Scientific Subroutines*, Volumes I and II, BYTE Publications/McGraw-Hill, Inc., Peterborough, NH, (1981).

[5] P.S. Khiew, S. Radiman, N.M. Huang, Md. Soot Ahmad, *Journal of Crystal Growth*, **254** (2003) 239.

[6] A.A. Patel, F. Wu, J.Z. Zhang, C.L. Torres-Martinez, R.K. Mehra, Y. Yang, S.H. Risbud, *J. Phys. Chem.*, **B 104** (2000) 11598.

[7] S.Kumar, M.A.M. Khan, S.A. Khan, M. Husain, *Optical materials*, **25** (2004) 29.

CHAPTER 5

CATHODOLUMINESCENCE DEGRADATION OF THE SiO_2:PbS NANOPARTICULATE POWDER PHOSPHORS

5.1. Introduction

Standard cathodoluminescent (CL) phosphors normally lose brightness upon bombardment with an electron beam. The changes in the cathodoluminescent brightness and in the surface chemistry of nanoparticulate SiO_2 coated powder phosphor have been reported [1]. This chapter deals with cathodoluminescence degradation of SiO_2:PbS nanoparticulate powder phosphors prepared by the sol-gel process. The powders were degraded under different oxygen pressures and the CL intensity as a function of electron dose and the surface chemical changes were recorded. A possible mechanism for the desorption of oxygen from the surface causing a decrease in the CL intensity is discussed. In this study, AES, XPS and CL spectroscopy were used to characterize the SiO_2:PbS powder samples.

5.2. Experimental

The surface chemical composition of the samples was investigated with AES and XPS while the CL brightness was investigated by using an Ocean Optics spectrometer. AES and the CL spectroscopy data were collected simultaneously and an Ocean Optics S2000 spectrometer, respectively. The powders were irradiated with a beam of electrons with an energy of 2 keV and a beam current density of 54 mA/cm^2 in an ultra high vacuum chamber for several hours. The chamber was first evacuated to approximately 2×10^{-9} Torr before being backfilled to 5×10^{-8}, 1×10^{-7} and 2×10^{-7} Torr O_2 pressures for the degradation. Finally, a Quantum 2000 scanning microprobe XPS system was used for the analysis of the degraded spots. All measurements were done at room temperature. Figure 5.1 shows schematic diagram of the PHI Model 549 Auger spectrometer with a quartz view port for the S2000 spectrometer mounted approximately 60° to the incident electron beam.

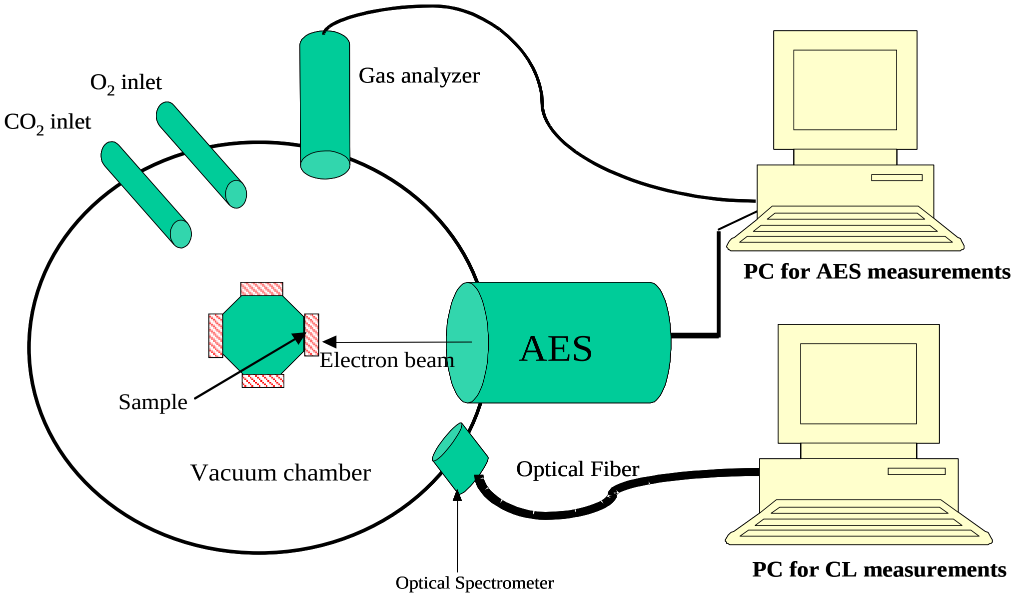

Figure 5.1. AES and Optical spectrometer used to take measurements.

5.3. Results and discussion

SiO_2:PbS samples were bombarded with a beam of electrons under different residual O_2 gas pressures. Figure 5.2 shows the AES spectra of SiO_2:PbS before and after degradation with characteristic Auger peaks of Si at 78 eV and O_2 at 506 eV. The Si peak in the compound (SiO_2) is known to be in the range of 70 – 80 eV and the shift from the normally high energy Si (92 eV) peak of the element (Si) to a low energy is attributed to the change in the density of state in the valence band and relaxation effects [2]. The AES spectrum after degradation shows a change in the shape of the shoulder of the Si (78 eV) peak.

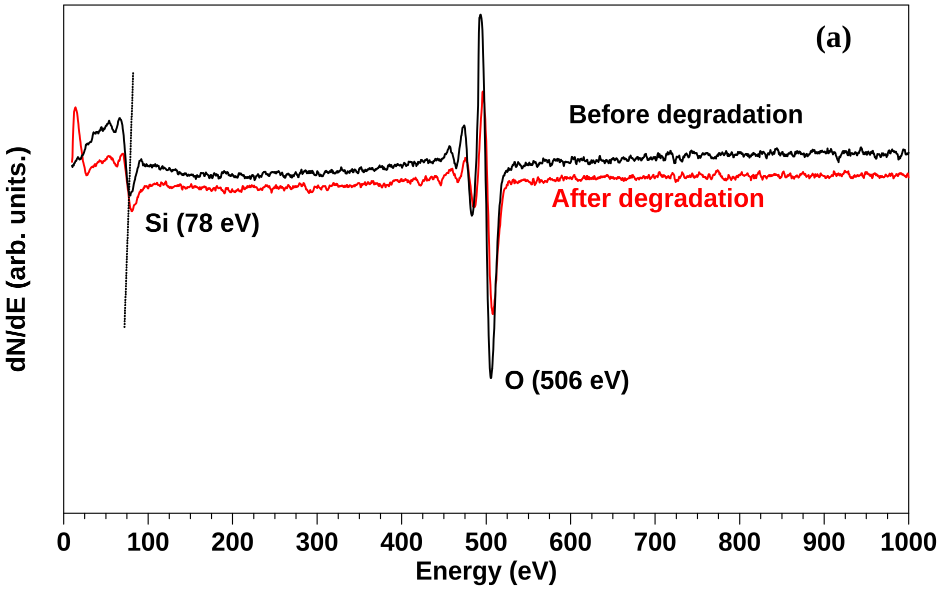

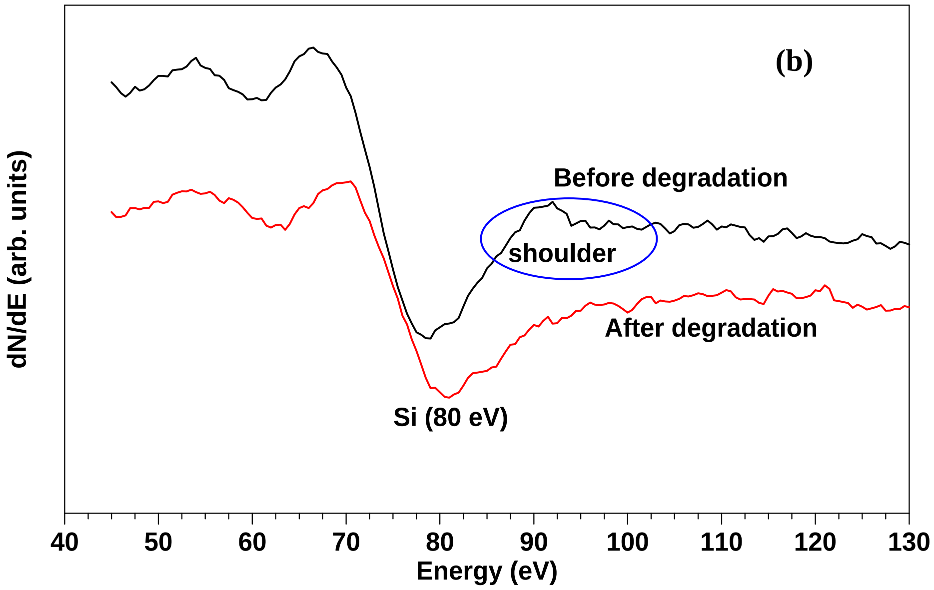

Figure 5.2. (a) AES spectra from SiO_2:PbS powder phosphor before and after degradation in 1×10^{-7} Torr O_2, and (b) a detailed Si (78 eV) peak before and after degradation.

A detailed Si (78 eV) peak shape before and after degradation is shown in Figure 5.2 (b). The change in shape is due to the development of the extra peaks of SiO_x(0<x<2) and elemental Si caused by the electron bombardment. A slight Si peak shift towards higher energies was also observed.

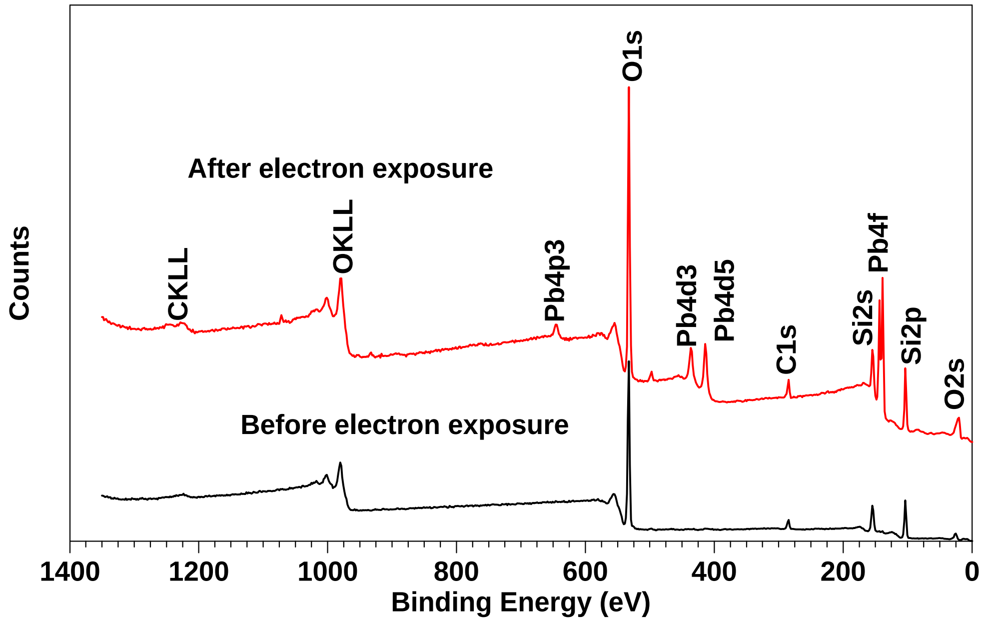

Figure 5.3. XPS spectra of SiO_2:PbS powder phosphor before and after electron exposure.

Figure 5.3 shows the XPS spectra of the nanoparticle phosphors powder before and after electron exposure. The lead peaks (Pb4f, Pb4d5, Pb4d3 and Pb4p3) are not clear/are overshadowed in the spectrum of the as prepared powder sample due to low concentration of PbS in SiO_2, but the peaks were clearly seen after the powder sample was subjected to electron exposure of 700 C/cm^2. The enhancement of the Pb4f, Pb4d5, Pb4d3 and Pb4p3 peaks after electron exposure is attributed to the dissociation of the SiO_2 into elemental Si and O [2,3,4] which resulted in oxygen desorbing from the surface and thereby exposing the PbS nanoparticles.

Figure 5.4 (A) shows the CL spectra before and after degradation. Maximum intensity of the CL spectra was observed to be at the wavelength of 680 nm. The peak is, however, very broad due to the contribution of the different particle sizes. Kumar and Jakhmola [5] measured a fluorescence peak at 675 nm at room temperature for RNA-mediated fluorescent PbS nanoparticles with a broad size distribution of 2 – 24 nm which corresponds to a band gap of 1.86 eV. The emission peak was 70% of the initial intensity after degradation showing that a prolonged exposure to 2 keV electrons reduces the CL intensity. Figure 5.4 B(i) and (ii) shows the photographs of the irradiated spot before and after electron degradation, respectively. The intensities observed from the CL photographs correspond very well with the intensities of the CL spectra before and after electron exposure.

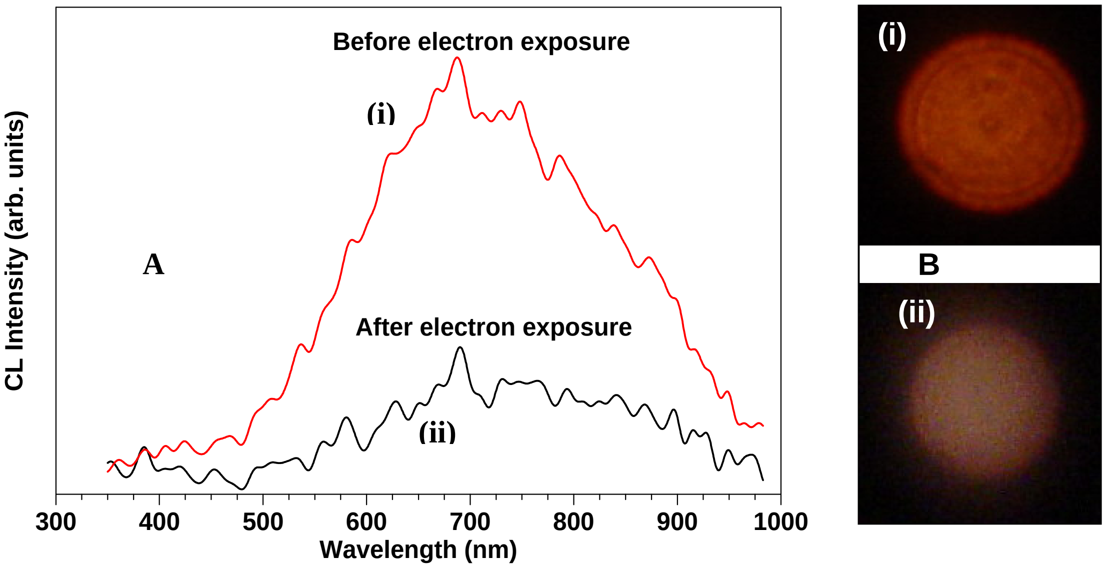

Figure 5.4. (A) CL emission spectra of SiO_2:PbS powder phosphor (i) before and (ii) after electron exposure in 1×10^{-7} Torr O_2. B(i) and (ii) are the photographs of the irradiated spot before and after degradation.

Figures 5.5 and 5.6 show the change in both CL intensity and Auger peak-to-peak heights (APPHs) of C, O_2 and Si for the SiO_2:PbS nanoparticle phosphors as a function of electron dose at O_2 pressures of 1×10^{-7} Torr and 5×10^{-8} Torr, respectively. During the electron bombardment of the nanoparticle powders, the O_2 signal decreased considerably with time. There is no noticeable change in the Si peak-to-peak heights during the degradation process. A very small C peak-to-peak height remains constant throughout the degradation process. The desorption of oxygen from the surface is apparent and suggests the degradation of the surface due to the dissociation of SiO_2 [2,3,6] into elemental Si and O_2 by the electron bombardment. Oxygen desorbs from the surface under prolonged electron bombardment thereby leaving the surface rich in elemental silicon [3,4,6,7].

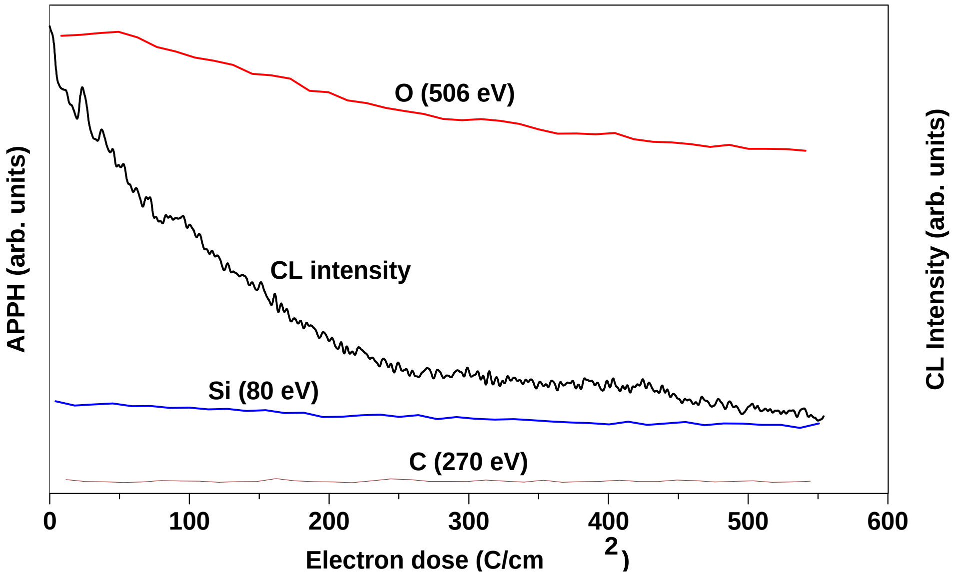

Figure 5.5. Auger peak-to-peak heights of O, Si and C as a function of 2 keV electron dose in 1 × 10^{-7} Torr O_2.

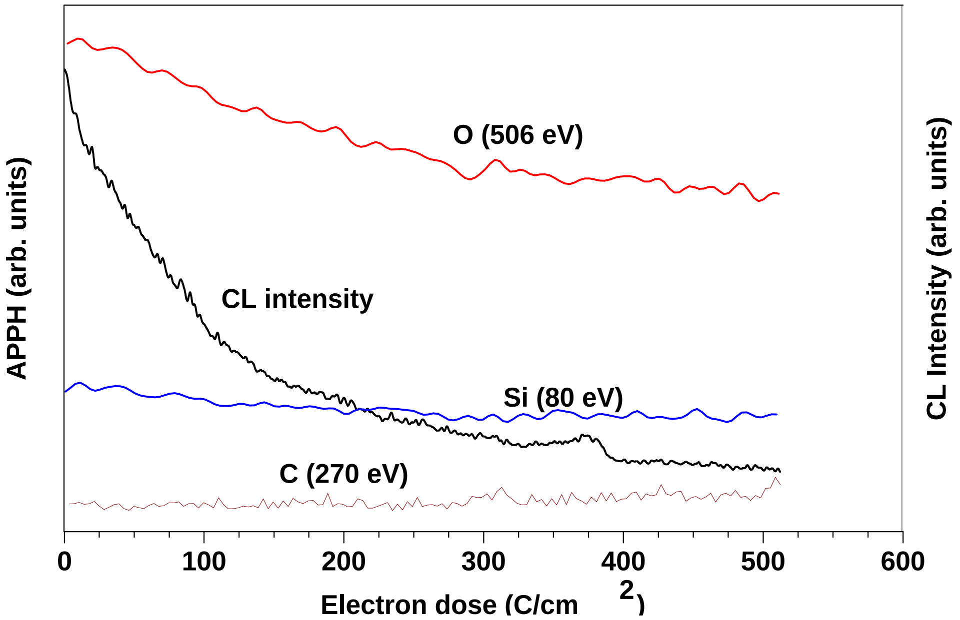

Figure 5.6. Auger peak-to-peak heights of O, Si and C as a function of 2 keV electron dose in 5 × 10^{-8} Torr O_2.

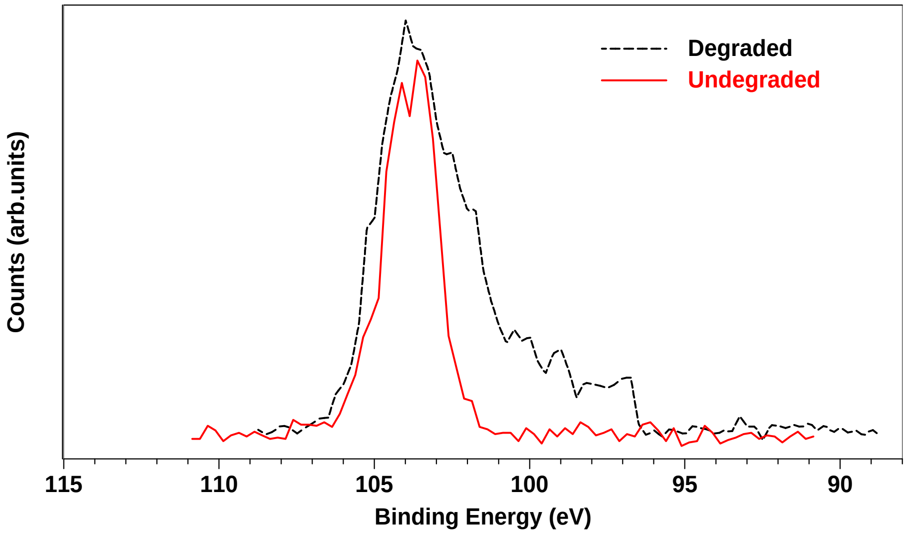

Figure 5.7. A high resolution XPS scan of the Si2p peak before and after degradation.

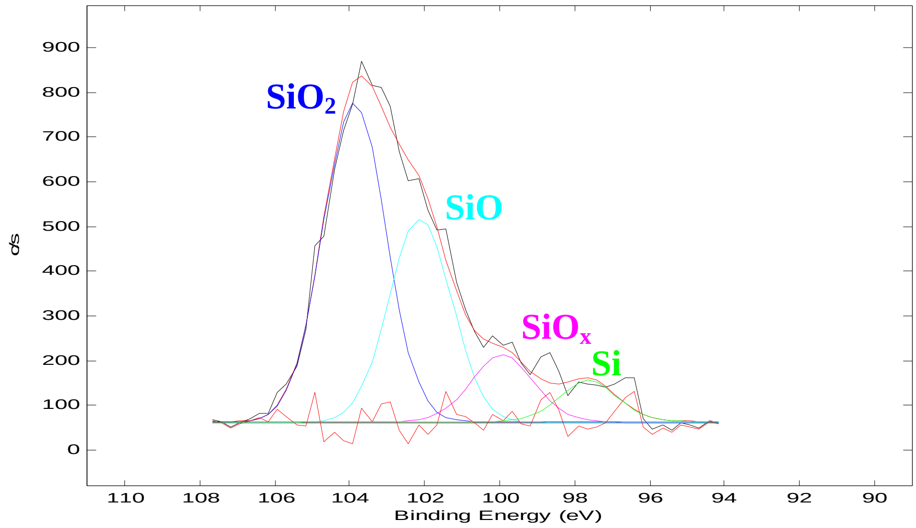

Figure 5.8. The XPS peak fitting of the Si2p peak after degradation. A combination of SiO_2, SiO, SiO_x and elemental Si was observed in the degraded powder samples.

Figure 5.7 shows a high resolution XPS scan of the Si2p peak before and after degradation. The Si2p peak after degradation has broadened on the low energy side of the peak. The peak fit, as shown in Figure 5.8, of the degraded sample shows that there are extra peaks of SiO (101.8 eV) [8], SiO_x (100.4eV) [9] and Si (98.6 eV) [10] developing on the low-energy side of the Si2p-103.6 eV in the peak of the degraded powder. A concurrent decrease in the CL intensity and the O_2 APPH suggests the change in the surface composition of the SiO_2:PbS surface. A simplified mechanism for the desorption of O_2 from a soda-glass bombarded with electrons as proposed by Lineweaver [6] involves the penetration of the electrons into the glass and dissipate their energy by ionizing and exciting the atoms of the glass. The electrons then come to rest at some depth in the glass by producing a net negative charge. This net charge set up a field in the glass layer. The positive sodium ions present in the glass move away from the surface due to the influence of the field and the oxygen ions diffuse towards the surface and eventually released into the vacuum. After bombarding the surface with electrons, the degraded spot is left rich in elemental silicon and SiO_2 being reduced to oxygen deficient

SiO_x (0<x<2) which is thought to be less efficient and as a result a decrease in the CL intensity of the SiO_2:PbS powders.

An alternate interpretation for the dissociation and desorption observed in SiO_2 is the electron stimulated desorption (ESD) [3,4], whereby the silicon-oxygen bond is broken by the excitation into an ionic state. This is followed by desorption of oxygen into the atmosphere which results in a decrease in the CL intensity as can be seen in the presented data. An important parameter influencing the dissociation of SiO_2 as documented by Thomas [3] is the residual gas pressure of oxygen in the chamber. Due to the recombination of Si and O_2, the dissociation of SiO_2 is much less at higher oxygen pressures. The rate at which oxygen and silicon recombine after the dissociation due to electron bombardment is larger at higher oxygen pressures. Figure 5.9 shows the normalized CL intensity curves as a function of electron dose for data collected at 2×10^{-7}, 1×10^{-7} and 5×10^{-8} Torr O_2. Swart et al. [11] reported an increase in the degradation rate of ZnS phosphors as the oxygen pressure increases. The data in this study show a decrease in the degradation rate as the oxygen pressure increases from 5×10^{-8} to 2×10^{-7} Torr which is different from what was reported by Swart et al. [11], but expected for SiO_2:PbS since its degradation is attributed to the dissociation of SiO_2 (into elemental Si and O) which is much less at high oxygen pressures.

The desorption of O_2 in this study could also be associated with an electron stimulated surface chemical reaction (ESSCR) [11,12] as reported by Ntwaeaborwa et al. [2] in the study of the degradation of SiO_2:Ce,Tb. Under electron-beam bombardment, the Si-O bonds are broken and free oxygen desorbed as ions or as O_2 molecules following a reaction with dissociated species (H, O or C) from vacuum ambient gases (e.g. H_2O, O_2 and CO_2). Another possibility as observed by Thomas [3] is that the excess O_2 gas in the system can recombine with the dissociated silicon to form SiO_2 again, which explains why the degradation rate is slower at higher oxygen pressures. It was clear from the APPH data shown in figure 5.10 that the desorption of O_2 from the surface at higher O_2 pressures was less severe than at lower pressures which confirms why the rate of CL degradation SiO_2:PbS is less severe at higher oxygen pressures.

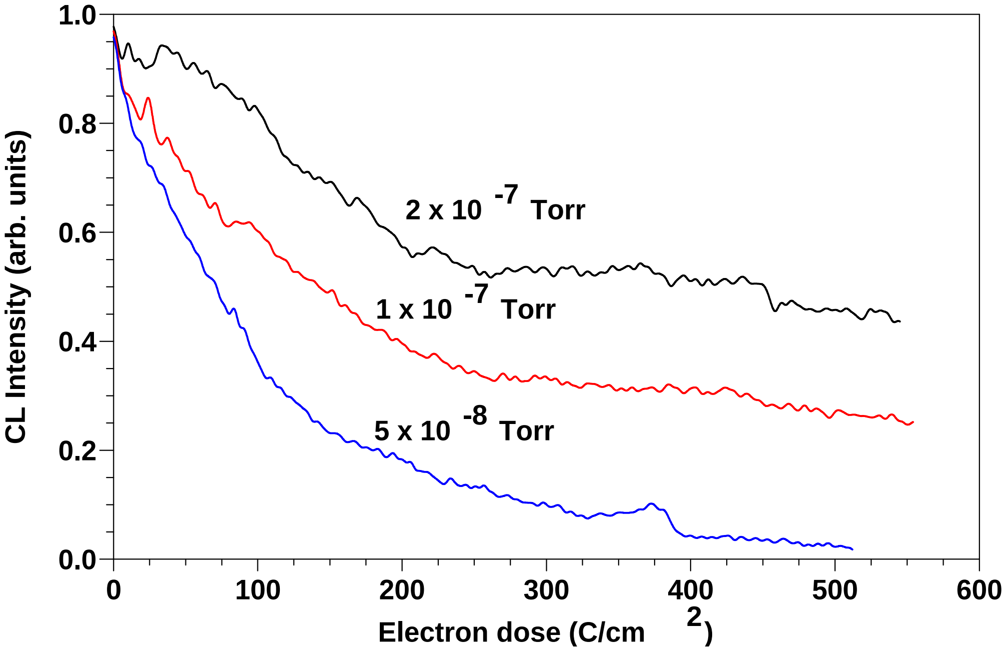

Figure 5.9. Normalized CL intensities versus electron dose at 2×10^{-7} Torr O_2 , 1 × 10^{-7} Torr O_2 and 5 × 10^{-8} Torr O_2.

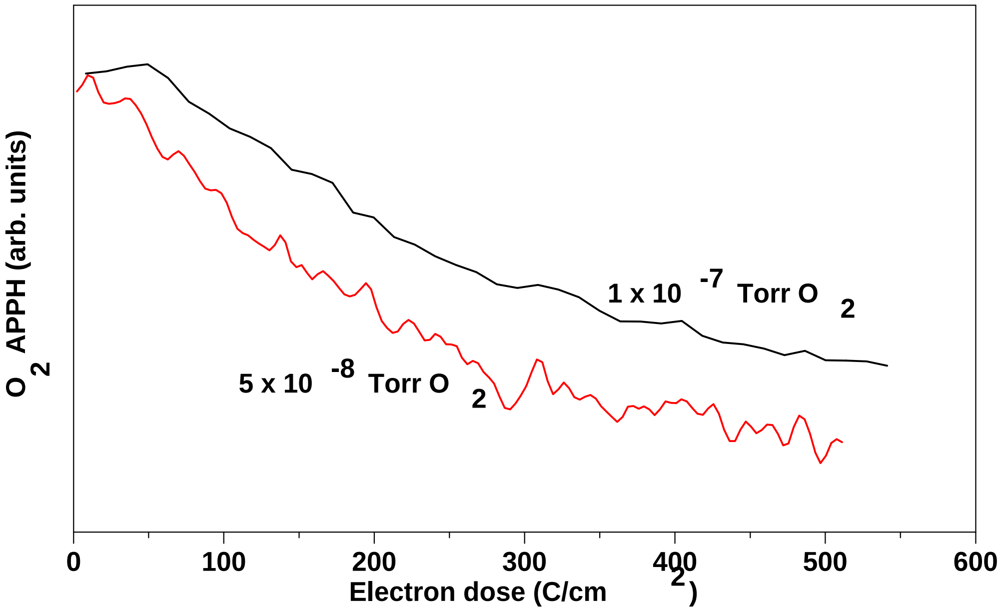

Figure 5.10. Normalized O_2 APPH's versus electron dose at 1 x 10^{-7} Torr O_2 and 5 x 10^{-8} Torr O_2.

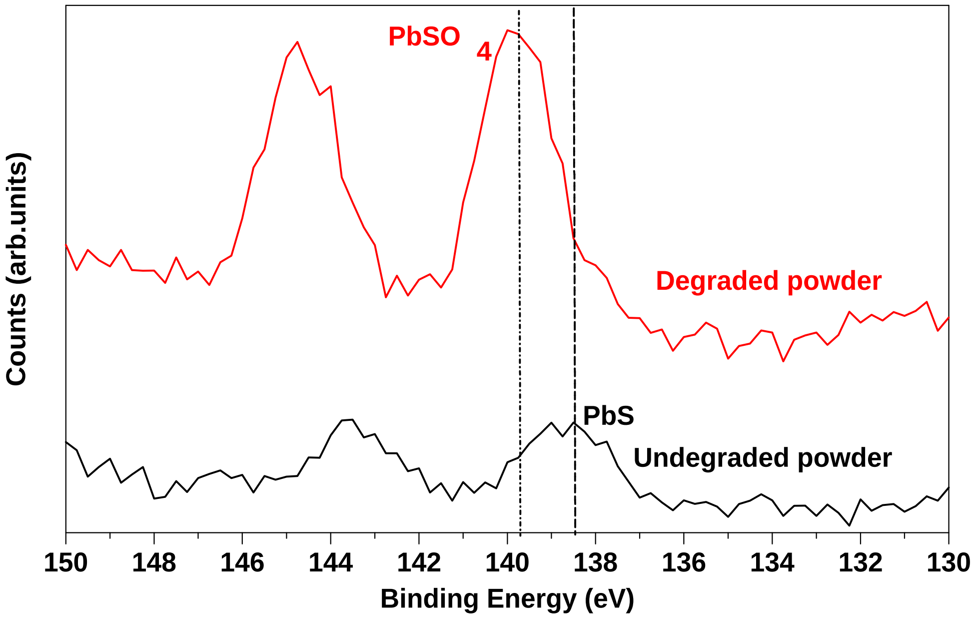

Figure 5.11. A high resolution XPS scan of the PbS peak before and after degradation.

Figure 5.11 shows XPS spectra of PbS sample before and after degradation. $PbSO_4$ was formed on the surface during electron bombardment. This is confirmed by a shift in the peak position of PbS before degradation to $PbSO_4$ after degradation [13]. Chen et al. [14], in their study of the degradation of ZnS phosphor reported the formation of a $ZnSO_4$ layer on the surface due to the electron bombardment in a dry O_2 ambient. The formation of $ZnSO_4$ was postulated to be due to the diffusion of charge reactants through the $ZnSO_4$ film to the reaction interfaces.

5.4. Conclusion

SiO_2 was reduced to SiO_x($0<x< 2$) by the desorption of oxygen from the surface during electron bombardment and the surface was left rich in elemental silicon. The rate of degradation of CL intensity decreased with an increase in the oxygen pressure. The decrease in CL intensity is best explained in terms of the formation of a less efficient SiO_x ($0<x< 2$) layer on the surface. The reaction on the surface is a combination of the dissociation of the SiO_2 by the e-beam and the recombination of the dissociated Si with the O_2 in the chamber. A combination of SiO_2, SiO, SiO_x and elemental Si was observed in the degraded powder samples. $PbSO_4$ was also formed on the surface during electron bombardment of SiO_2:PbS.

References

[1] B.L. Abrams, W.J. Thomes, J.S. Bang, P.H. Holloway, Rev. Adv. Mater. Sci., **5** (2003) 139 .

[2] O.M. Ntwaeaborwa, H.C. Swart, R.E. Kroon, P.H. Holloway, J.R. Botha, *J. Phys.Chem. Solids,* **67** (2006) 1751.

[3] S. Thomas, *J. Appl. Phys*., **45** (1) (1974) 161.

[4] T.E. Madey and J. T. Yates, *J. Vacuum Sci. and Tech.,* **8** (4) (1971) 525.

[5] A. Kumar and A Jakhmola, *Langmuir*, **23** (6) (2007) 2915.

[6] J.L. Lineweaver, *J. Appl. Phys.,* **34** (6) (1963) 1786.

[7] L.F. Vassamillet, *J. Appl. Phys*., **40** (4) (1969) 1637.

[8] T.P. Nguyen, S. Lefrant, *J. Phys. Cond. Matter,* **1** (1989) 5197.

[9] W.A.M. Aarnik, A. Weishaupt, A. van Silfout, *Appl. Surf. Sci*., **45** (1990) 37.

[10] G.E. Franklin, D.H. Rich, H. Hong, T. Miller, *Phys. Rev*., B **45** (1992) 3426.

[11] H.C. Swart, L. Oosthuizen, P.H. Holloway and G.L.P. Berning, *Surf. Int. Anal*., **26** (1998) 339.

[12] H.C. Swart, T.A. Trottier, J.S. Sebastian, S.L. Jones and P.H. Holloway, *J. Appl. Phys.,* **83** (9) (1998) 4579.

[13] L.R. Pederson, *J. Electron Spectrosc. Relat. Phenom,* **28** (1982) 203.

[14] SH Chen, AP Greeff and HC Swart, *J. of Lumin.,* **109** (2004) 93.

CHAPTER 6

PHOTOLUMINESCENCE PROPERTIES OF SiO_2 SURFACE PASSIVATED PbS NANOPARTICLES

6.1. Introduction

A unique property associated with semiconductor nanoparticles is their luminescence characteristics with the specific emission wavelengths dependent upon the nature of the semiconductors, the physical dimensions, as well as the chemical environment. In this chapter, the photoluminescent properties of SiO_2 surface passivated PbS nanoparticle phosphors are discussed.

6.2. Experimental

A He-Cd laser (325 nm) and Ar^+ laser (458 nm) were used to excite photoluminescence (PL) of the SiO_2:PbS powder phosphor and the spectra were collected by using a 0.5 m SPEX 1870 spectrometer.

6.3. Results and discussion

Figure 6.1 shows the PL emission spectra of a pure SiO_2 powder sample excited at a wavelength of 325 nm with a He-Cd laser. A broad emission peak at ~ 450 nm was observed which is ascribed to SiO_2 (no peaks were observed at ~ 560 and 650 nm). The emission suggests that the transitions in SiO_2 (band gap ~ 7.8 eV) are not that of conduction band (CB) to valence band (VB), but from the defects inside the SiO_2. The emission at 450 nm has been ascribed to the defect luminescence originating from neutral oxygen vacancies [1].

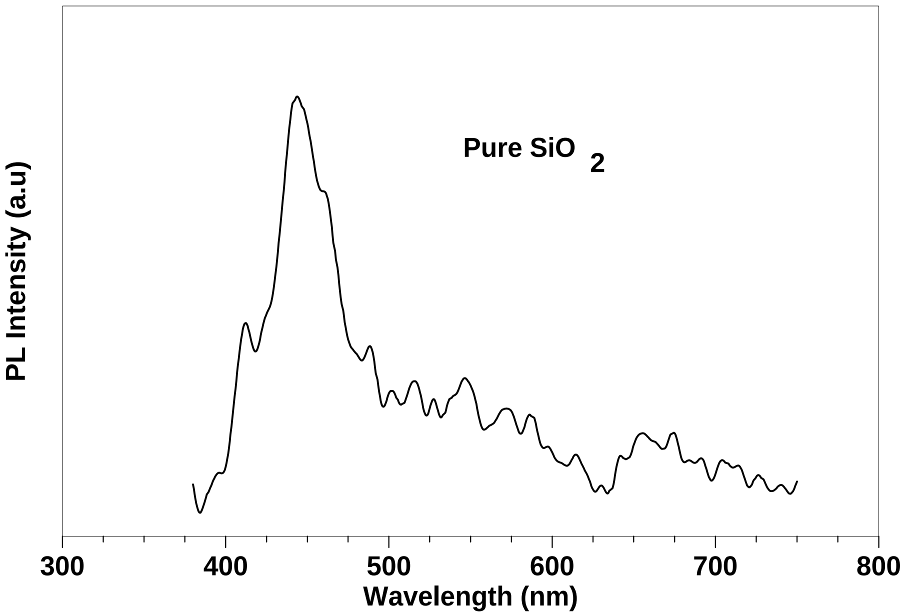

Figure 6.1. Photoluminescence (PL) spectrum of sol gel prepared SiO_2 powder excited with a He-Cd laser at 325 nm.

Figure 6.2(a) presents the normalized PL intensities of the SiO_2:PbS powder sample excited at 325 nm as well as the spectrum excited at a wavelength of 458 nm. The 325 nm excited PL emission spectrum of the SiO_2:PbS (Figure 6.2(a)) shows a strong peak at ~ 450 nm and a shoulder at ~ 560 nm. The shoulder is attributed to the PbS nanocrystallites. Further examination with an excitation at 458 nm from the Ar^+ laser gave rise only to the second emission peak at ~ 560 nm as shown in Figure 6.2(a). The observed peak corresponds very well with the shoulder that was observed with the excitation wavelength of 325 nm. The peak at ~ 560 nm was only observed in the powder with PbS nanoparticles, a further indication that it was from the PbS nanocrystals in SiO_2. Yang *et al*. have reported PL spectra of PbS embedded in sol-gel silica glass with an emission peak [2] at 440 nm when excited at 380 nm and another peak at 605 nm when excited at 475 nm. In their study, no shoulder was observed when they excite at 380 nm and the same emission wavelength (440 nm) was observed for the pure sol-gel silica glass.

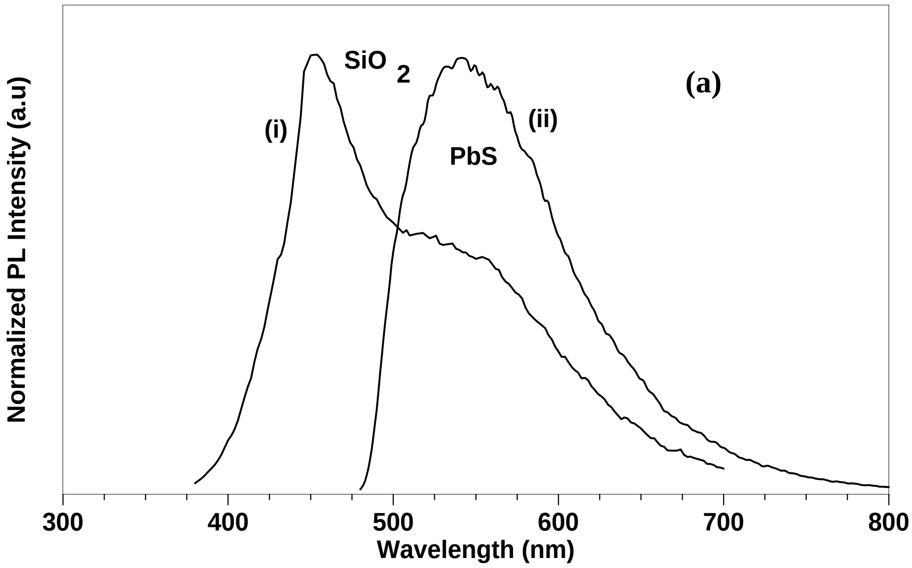

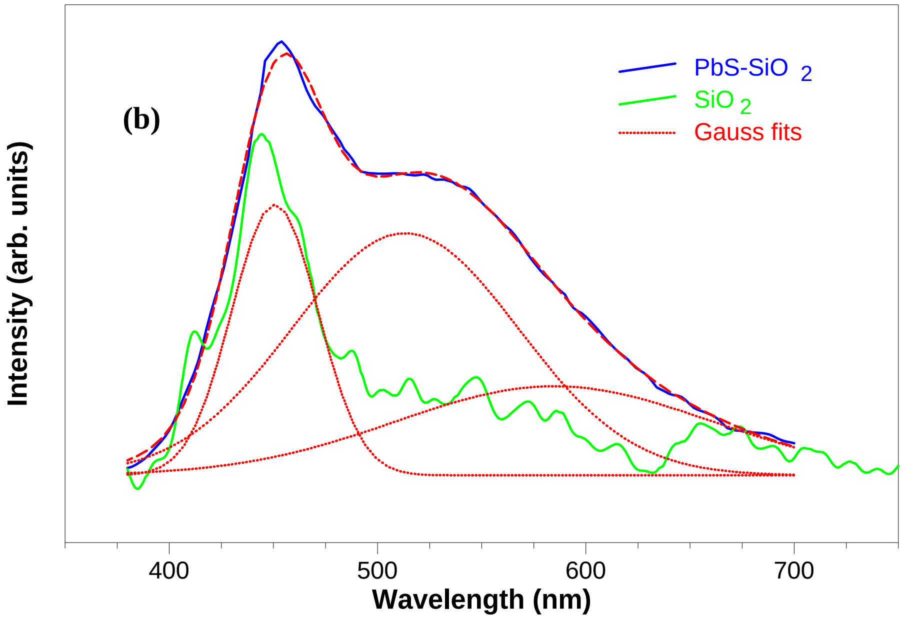

Figure 6.2. (a) Normalized photoluminescence (PL) of the SiO_2:PbS sample excited at (i) 325 nm and at (ii) 458 nm wavelengths, and (b) the 325 nm excited emission spectrum fitted with multiple gaussian profiles.

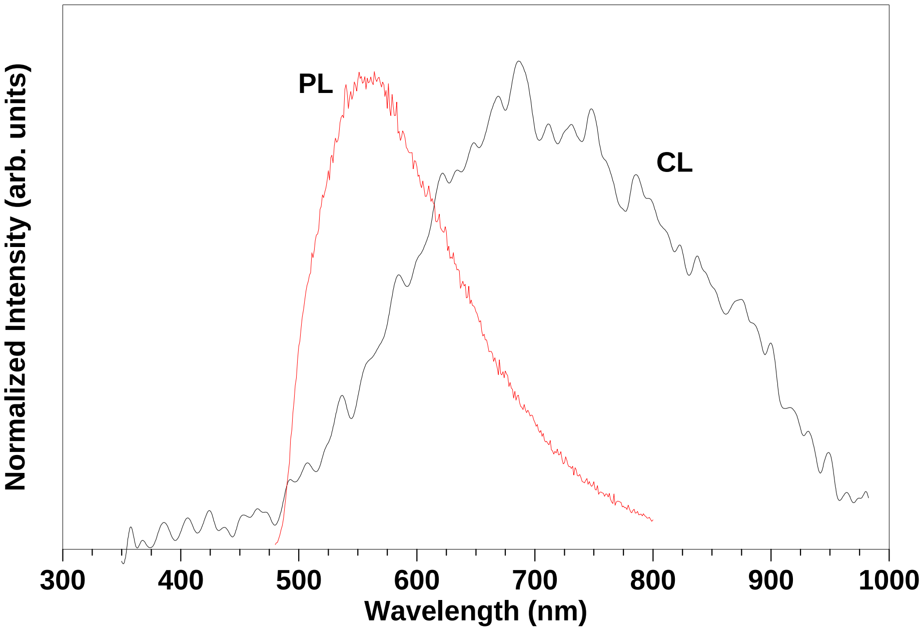

Figure 6.3. Normalized PL and CL emission spectra of SiO_2:PbS powder phosphor.

Figure 6.3 shows the normalized PL and CL spectra for the SiO_2:PbS powder. It is clear from the figure that the emission wavelengths of the PL and CL are different. One reason for the observed difference between the PL and CL spectra of SiO_2:PbS nano-powders may be attributed to the sample heating (local) due to the different excitation procedures [3]. The surface damage induced by local heating under electron excitation (irradiation) (CL) was visible to the naked eye. Another possibility may be that the excitation cross sections for the newly formed discrete energy levels, due to quantum confinement, for the two techniques (photons and electrons) are different in this case. The effect however must be investigated further in future.

The possible allowed electronic transitions as observed by Fernee *et al.* [4] for PbS nanoparticles are described by S_e - S_h and P_e - P_h. Sashchiuk et al. [5] measured a broad emission band of PbS in the range of 600 – 800 nm, in their study of optical and conductivity properties of PbS nanocrystals embedded in amorphous zirconia. A broad PL emission band peaking at 804 nm was also observed by Chen *et al.* [6] for alkanethiolate capped PbS nanoparticles. Cao et al. [7] observed a broad PL emission at

434 nm in their study of growth and photoluminescence properties of PbS nanocubes. For PbS nanoparticles over-coated with CdS, a broad band emission peak at 510 nm was observed by Warner *et al*. [8].

Our results show some similarities and also differences to previous studies. The difference can be ascribed to the different reaction environments and different host materials. In the strong quantum confinement regime, there may be a continuous variation in nanocrystal stoichiometry away from that of the bulk due to the change in the ratio of reactants required to form the smallest nanocrystals [9]. It is also speculated that a variation in stoichiometry may be driven by surface capping ligands that bind to only one atomic species [9]. Similarly sized PbS nanocrystals with different stoichiometries can have dramatically different optical properties which could explain some rather anomalous results obtained for PbS nanocrystals. Therefore, the luminescence properties of PbS can be affected by host materials, depending on the reaction conditions.

The emission peak excited at 325 nm was fitted with multiple gaussian profiles in Figure 6.2(b). At least three gaussian profiles are needed for an acceptable fit in this emission spectrum. The peak at 450 nm corresponds to the SiO_2 emission peak, as observed in Figure 6.1. The remaining two Gauss peaks of which one (at 514 nm) is stronger compared to the other one (at 593 nm) are ascribed to PbS nanoparticles transitions, representing, respectively, the direct recombination and the recombination through shallow surface states [4,10,11]. A schematic illustration of the allowed transitions is given in Figure 6.4. Our fits only showed two possible broad peaks while Fernée *et al.* [12] also mention the existence of transitions at other energies, which become possible with the introduction of some degree of symmetry breaking such as the departure from spherical symmetry. Due to the wavelength measuring restriction it was not possible to measure the other direct transition with the measuring system used in this study.

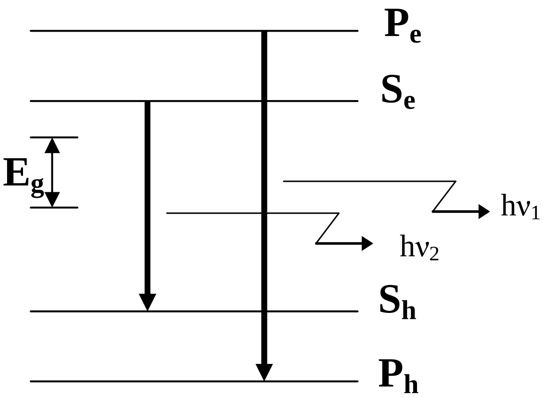

Figure 6.4. Allowed optical transitions in PbS nanocrystals [8].

It is a well known fact that the dispersion relations for the energy of electrons and holes in a semiconductor are parabolic at first approximation as illustrated in Figure 6.5(a) for a bulk semiconductor [13]. This approximation is true only for electrons and holes that occupy the levels that lie at the bottom and top of the conduction and valence bands respectively. It is important to remember that these parabola are really a *quasi-continuous* set of electron (hole) states along a given direction in ***k***-space and that the lowest occupied level in the CB and the highest occupied level in the VB are separated by an energy gap, which for bulk materials are usually in the order of an electron volt. When the dimensionality of the semiconductor bulk material is reduced in size to a zero-dimensional Quantum Dot the quasi-continuous nature is de-emphasized, since only discrete energy levels can exist in the dot. Subsequently each of the original parabolic bands of the bulk case is fragmented into an ensemble of points as demonstrated in Figure 6.5(b) for a nanoparticle.

These atomic-like electronic energy levels are formed due to charge-carrier confinement in three dimensions. The intrinsic characteristics due to the chemical composition and the distribution of sizes of the nanocrystals play an important role in the optical and electronic properties. Nanocrystals embedded in dielectric matrices behave as quantum boxes when their radii are smaller than the exciton Bohr radius and under such circumstances their optical properties are strongly modified compared to bulk [14]. As the particle diameter is reduced, the confinement energy increases and a blue-shift occurs

(Figure 6.6) [15] due to the quantum-confinement effect. The luminescence corresponding to the recombination of the excited hole and electron in a single nanocrystal will have a finite width due to homogeneous line broadening, as illustrated in Figure 6.6. The dependence of E_g on the particle size, which will be in the range, $r \pm \Delta r$, will have a further broadening effect on the luminescent wavelength. There will always be a statistical distribution of particle sizes due to the growth process. The results in this study clearly show the broadening of the peak due to the different sizes and the blue shift of the wavelengths due to quantum confinement.

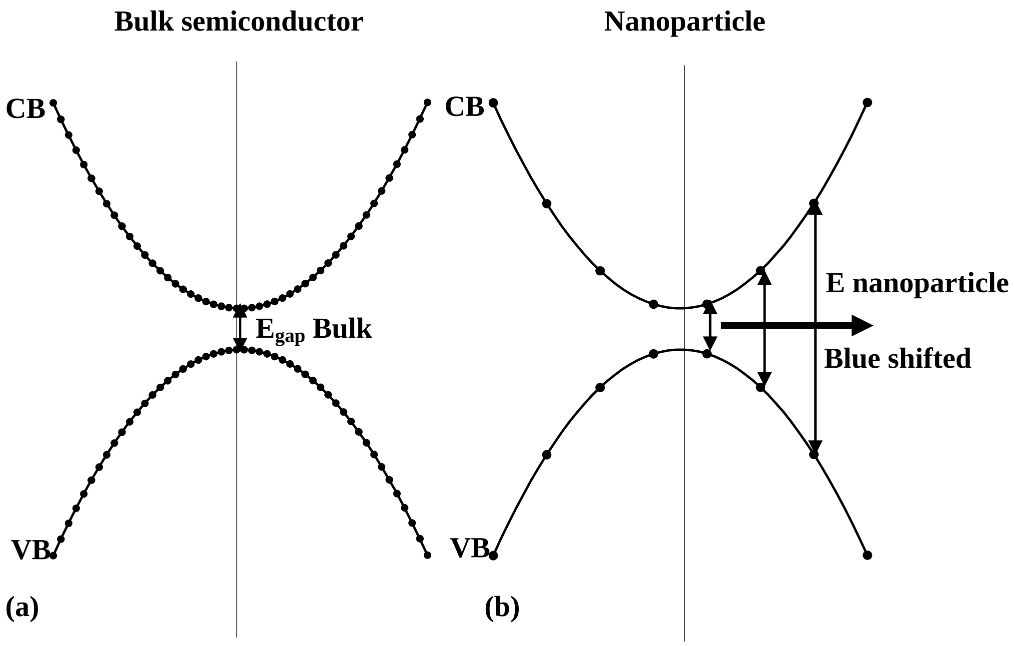

Figure 6.5. Energy dispersion for (a) the bulk semiconductor case compared to that of (b) the nanoparticle case. Partially redraw from [14].

The only way an electron can fill up an energy state in the CB is if it is excited to the CB from the VB, leaving behind a hole in the VB. Now due to the fact that both these carriers have charges, they will interact via the Coulombic force. However, even before that is considered, the amount of energy needed to excite the electron to the CB (which is equal to the energy gap ($E_{G\text{-}Bulk}$)) must also be taken into account. And then it must be considered that both carriers are confined in the 3D potential well ($E_{3D\text{-}Well}$). Coulomb interaction between the electron and the hole must also be taken into account as well as the screening by the rest of the crystal (E_B). An estimate of the size dependence of the energy gap of a *spherical* Quantum Dot can be made [16-22]:

$$E_{G-Dot} = E_{G-Bulk} + E_{3D-Well} + E_B$$
$$E_{G-Dot} = E_{G-Bulk} + \frac{h^2}{2\mu D^2} - 1.8\frac{e^2}{2\pi\varepsilon\varepsilon_0 D}$$

Where D is the diameter of the nanosphere, μ is the reduced mass of the exciton, ε, the exciton dielectric constant which gives an indication of the strength of the screening coefficient and ε_0 the dielectric constant for the semiconductor material under consideration.

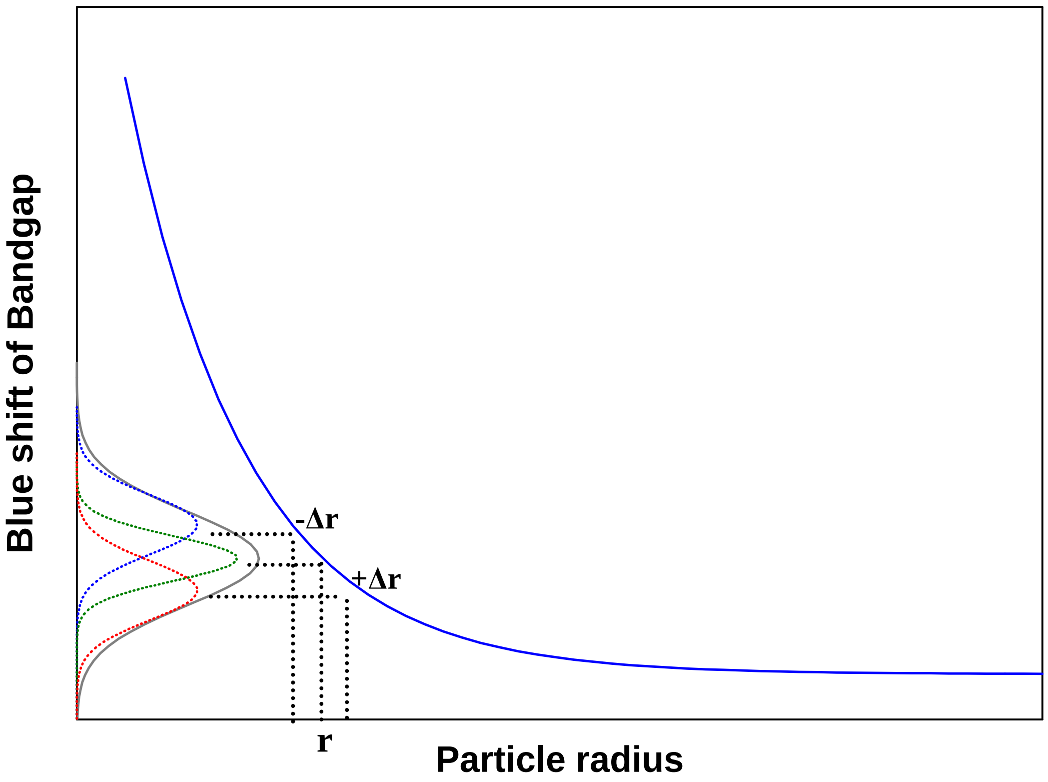

Figure 6.6. Induced blue or red shift in decreasing or increasing the nanoparticle diameter (r). The envelope shows the homogeneous line broadening of the emission peak due to composite size variation. Partially redraw from [15].

6.4. Conclusion

The emission wavelength of PbS nanoparticles in SiO_2 is blue-shifted (560 nm) from the bulk PbS emission wavelength (3200 nm). Strong emission peaks of SiO_2 at 450 nm and PbS at 593 nm and 514 nm were differentiated. The photoluminescence emission wavelength is blue-shifted from the cathodoluminescence emission wavelength.

References

[1] T. Inokuma, Y Kurata, and S Hasegawa, *J. Lumin.*, **80** (1999) 247.

[2] P. Yang, C. F. Song, M.K. Lu, X. Yin, G.J. Zhou, D. Xu and D.R. Yuan, *Chemical Physics Letters*, **345** (2001) 430.

[3] V.S. Gorelik, S.N. Mikov, M.I. Sokolovskii, T. Tsuzuki, *Inorganic Materials*, **42** (3) (2006) 284.

[4] M.J. Fernee, A. Watt, J. Warner, S. Cooper, N. Heckenberg and H. Rubinsztein-Dunlop, *Nanotechnology*, **15** (2004) 1329.

[5] A. Sashchiuk, E. Lifshitz, *J. Sol-Gel Sci. and Technol*., **24** (2002) 35.

[6] S.Chen, L.A. Truax, J.M. Sommers, *Chem. Mater*., **12** (2000) 3864.

[7] H.Cao, G. Wang, S. Zhang, X. Zhang, *Nanotechnology*, **17** (2006) 3281.

[8] J.H. Warner, A.R. Watt, M.J. Fernee, N.R. Heckenberg, H. Rubinsztein-Dunlop, *Nanotechnology*, **16** (2005) 482.

[9] M.J. Fernee, E. Thomsen, P. Jensen, H. Rubinsztein-Dunlop, *Nanotechnology*, **17** (2006) 956.

[10] M.J. Fernee, A. Watt, J. Warner, S. Cooper, N. Heckenberg and H. Rubinsztein-Dunlop, *Nanotechnology*, **14** (2003) 991.

[11] B. Capoena, A. Martuccib, S. Turrellb, M. Bouazaoui, J of Molecular Structure, **651–653** (2003) 467.

[12] M.J. Fernee, A. Watt, J. Warner, N. Heckenberg and H. Rubinsztein-Dunlop, *Nanotechnology*, **15** (2004) 1351.

[13] W.J. Parak, L.Manna, F.C. Simmel, D. Gerion, A.P. Alivisatos, *Nanoparticles – From Theory to Applications*, Wiley – VCH Verlag GmbH & Co. KGaA, 2004.

[14] J.L. Machol, F.W. Wise, R.C. Patel and D.B. Tanner, *Phys. Rev.*, B **48** (1993) 2819.

[15] A.L. Rogach, A. Eychmuller, S.G. Hickey, and S.V. Kershaw, *Small*, www.small-journal.com, 2007, **3** (4) 537.

[16] M.G. Bawendi, M.L. Steigerwald, L.E. Brus, Annu. *Rev. Phys. Chem*., **4**1 (1990) 477.

[17] T. Trindade, P. O’Brien, N.L. Pickett, *Chem. Mat*., **13** (2001) 3843.

[18] L.E. Brus, *J. Chem. Phys*., **79** (1983) 5566.

[19] L.E. Brus, *J. Chem. Phys*., **80** (1984) 4403.

[20] L.E. Brus, *J. Chem. Phys*., **90** (1986) 2555.

[21] R.A. Harris, Ph.D dissertation, University of the Free State, 2006.

[22] M.L. Steigerwald, L.E. Brus, *Acc. Chem. Res*., **23** (1990) 183.

CHAPTER 7

PHOTOLUMINESCENCE PROPERTIES OF POWDER AND PULSED LASER DEPOSITED PbS NANOPARTICLES IN SiO_2

7.1. Introduction

Nanostructured materials, and in particular semiconductor nanostructures and thin films may be exploited for their novel electronic and optical properties. These structures are of great interest since they have potential applications in future quantum and photonic devices [1]. An amorphous silica (SiO_2) has been used as a host matrix for different band gap and rare-earth elements to prepare nanophosphors that could be used in light emitting technologies.

Sukhovatkin et al. [2] measured room-temperature amplified spontaneous emission and spectral narrowing at infrared wavelengths in solution-processed films made up of PbS quantum-dot/nanocrystals. These are relevant to optical amplification applications. Nanocrystals synthesized in an aqueous solution result in high quantum-dot volume fractions in solid films and in a red-shift emission relative to absorption. Integration of light emitters, detectors, modulators, and signal-processing elements on a single chip would combine electronic-based computing with optical- and radio-frequency-based communications.

Thin film sensors on the basis of different glass materials (PbS-AgI-AsS, CdS-AgI-AsS, Tl-Ag-As-I-S) have been prepared by means of an off-axis pulsed laser deposition technique (PLD) [3]. It is shown that the complex stoichiometry of the chalcogenide target materials is maintained in the chalcogenide thin films prepared by PLD. The sensor performance results obtained from the thin films compared good with measurements performed with bulk sensors.

PbS nanoparticles were incorporated in SiO_2 by a sol-gel process resulting in a nanoparticulate phosphor (nanophosphor) that can be used in light emitting devices. SiO_2 has been a preferred host matrix for PbS nanoparticles lately because it has been reported to exhibit high fluorescence intensity compared to other matrices such as ZnS [4]. The photoluminescence properties of nanoparticulate SiO_2:PbS powder and pulsed laser deposited thin films as well as the effects of temperature on the PL intensity, particle growth and morphology of the films are reported.

7.2. Experimental

Silica glass (SiO_2) doped with PbS was prepared by a sol-gel process at room temperature. The gels were dried at room temperature for ~3 – 10 days. The sol-gel preparation of SiO_2:PbS phosphor is discussed in details elsewhere [5]. The dried gels were ground into powders and annealed in air at 200 ^oC for 2 hours. The powders were pressed to prepare pellets that were used as targets to grow thin films. The targets were ablated on Si (100) substrates using a 248 nm KrF laser at different deposition temperatures of room temperature, 100 ^oC, 200 ^oC, 300 ^oC and 400 ^oC. The deposition was carried out at the pressure of 300 mTorr O_2 using PLD system and the target-to-substrate distance was ~5 cm. The targets were ablated at a frequency of 10 Hz, laser beam spot size of 13 mm^2, the energy of 182 mJ and the pulse duration of 30 ns. Particle morphologies were determined by Leo-Field Emission Scanning Electron Microscope model 1525 and the PL emission data was collected by using a 458 nm Ar^+ laser fitted with a SPEX 1870 0.5 m spectrometer and a photomultiplier detector. A schematic diagram of the PLD system is shown in figure 7.1.

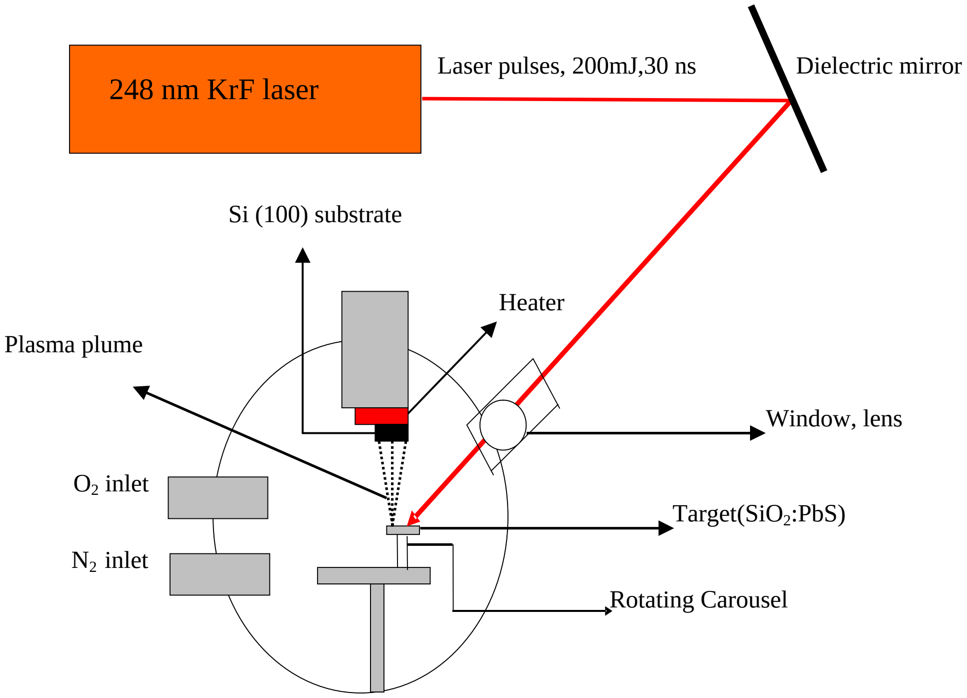

Figure 7.1. Schematic diagram of the PLD system.

7.3. Results and discussion

Figures 7.2 (a) –(d) show the SEM images of SiO_2:PbS thin films deposited at different temperatures on Si (100) substrates. The films in figure 7.2 (a) – (d) were deposited at room temperature, 100 ^oC, 200 ^oC and 400 ^oC, respectively. It is clear from the images that the deposited material consisted of agglomeration of spherical nanoparticles distributed uniformly over the substrates. The diameters of the spheres increased relatively with temperature suggesting that there is a correlation between deposition temperatures and growth in particle sizes. Similar results have been reported by Riabinina et al [1]. Figure 7.3 presents the relationship between the sizes of the agglomerated particles and the substrate temperatures from the SEM images. The graph clearly shows that the sizes of the agglomerated nanoparticles increased with an increase in the substrate temperatures.

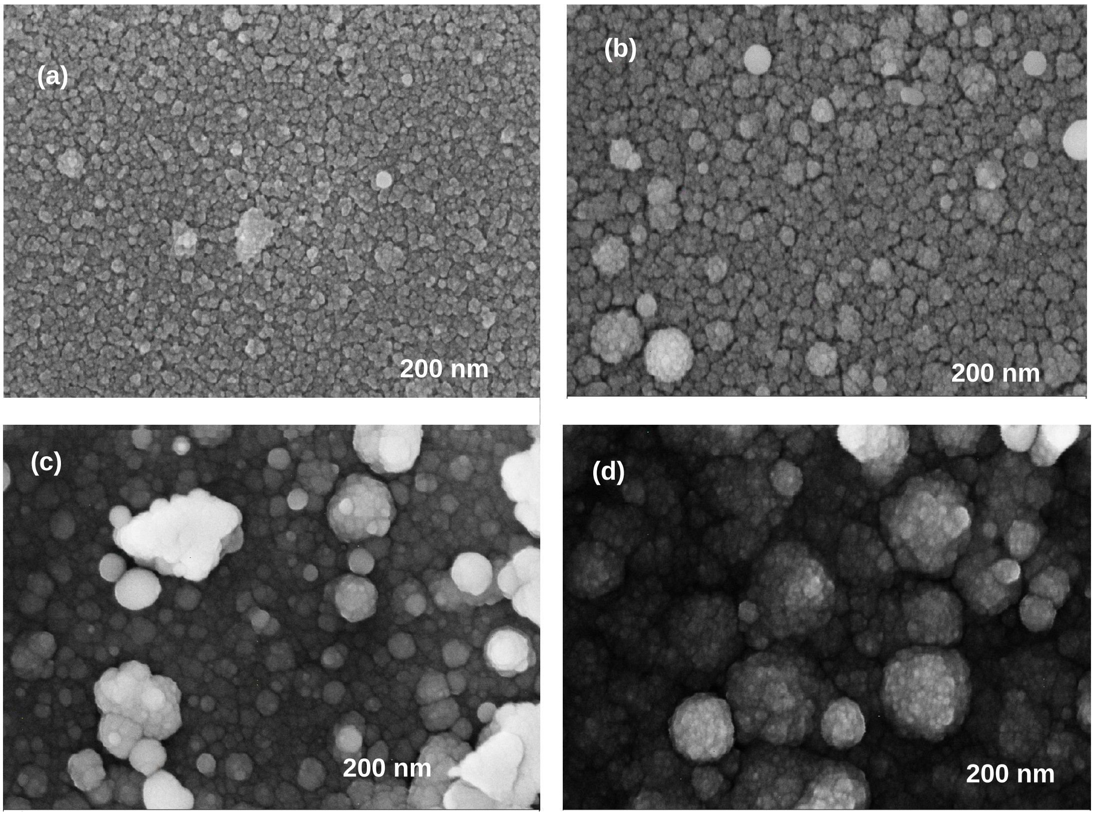

Figure 7.2. SEM images of the PLD thin films deposited at different substrate [Si(100)] temperatures; (a) room temperature, (b) 100 °C, (c) 200 °C and (d) 400 °C.

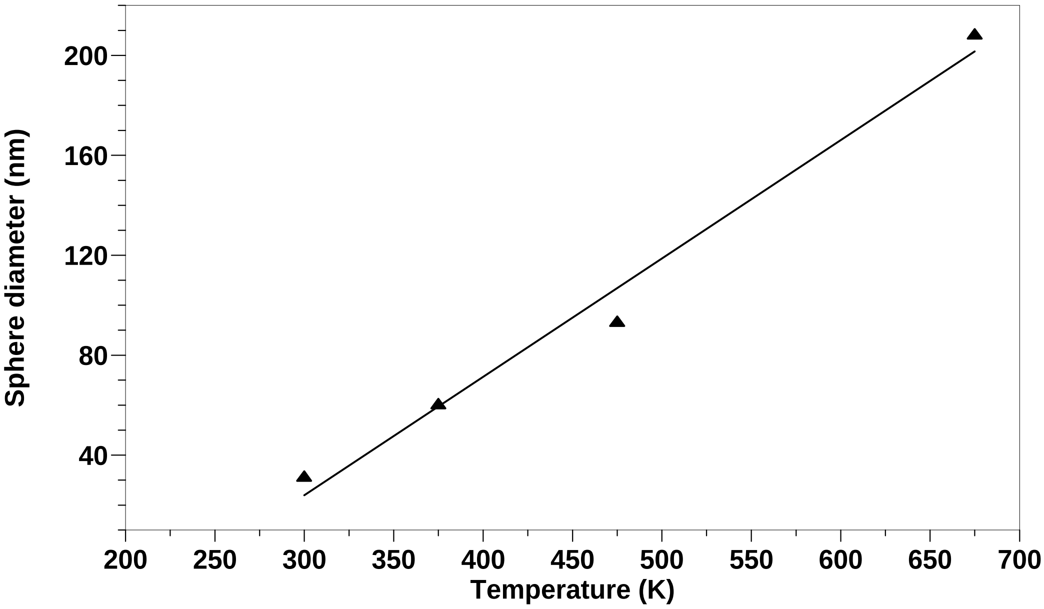

Figure 7.3. Diameter of agglomerated particles as a function of deposition temperatures of the thin films.

The increase in the substrate/deposition temperatures is reported to have caused an increase in the connectivity (agglomeration) between particles [6] due to the sintering of small particles. This would eventually lead to grain growth at high enough temperatures. The results (connectivity) are expected to increase delocalization of electrons, which results in a loss of the quantum-size effect. Nanda et al [7] have also reported that sintering and recrystallization of small primary particles into larger particles lead to a reduction in band gap as the quantum confinement decreases, eventually almost reaching the value of the bulk. This behavior is clearly seen in our PL emission spectra of the powder and thin film samples.

Figure 7.4 shows the photoluminescence (PL) spectra of SiO_2:PbS powder and the PLD thin film. PL emission spectrum of SiO_2:PbS (figure 6.2) excited with a He-Cd laser at 325 nm showed a broad peak at ~ 450 nm and a shoulder peaking at ~560 nm. The emission from SiO_2 is ascribed to the defects luminescence originating from neutral oxygen vacancies [8]. The SiO_2:PbS powder was further examined with an excitation wavelength of 458 nm Ar^+ laser, figure 7.4, and only the peak at ~560 nm was observed, which corresponds very well with the observed shoulder. This emission is attributed to PbS nanoparticles in SiO_2. Similar results have been reported elsewhere [4,9].

The PL emission from the SiO_2:PbS powder is more intense than that of the film made from this same powder. The weak PL intensity of the film is attributed to poor poly-crystalline quality and some incidental defects that could have been introduced in the thin film during the PLD process. The PL spectrum of the thin film is red-shifted from that of the powder by approximately 100 nm. The red-shift is ascribed to band tail effects [10,11,12] associated with incidental impurities/defects in the material. A defect-free crystalline semiconductor has the absorption spectrum terminating abruptly at the energy gap [11]. Wang et al [13] observed a red-shift of the PL emission wavelength of CdS/SiO_2 PLD thin films with respect to bulk and they attributed the shift to the interaction of the CdS nanocrystallites with SiO_2 at their interfaces. Tong et al [14] also observed a large red-shift of the PL emission wavelength of the CdS thin films grown by PLD process. In their study, they observed that during deposition, the CdS films experience sulfur (S) loss due to an outward diffusion process, and as a result there is expected to be large density of S vacancies in the film. Eventually this leads to a decrease in the band gap due to disorder effects produced by S vacancies and Cd interstitial defects.

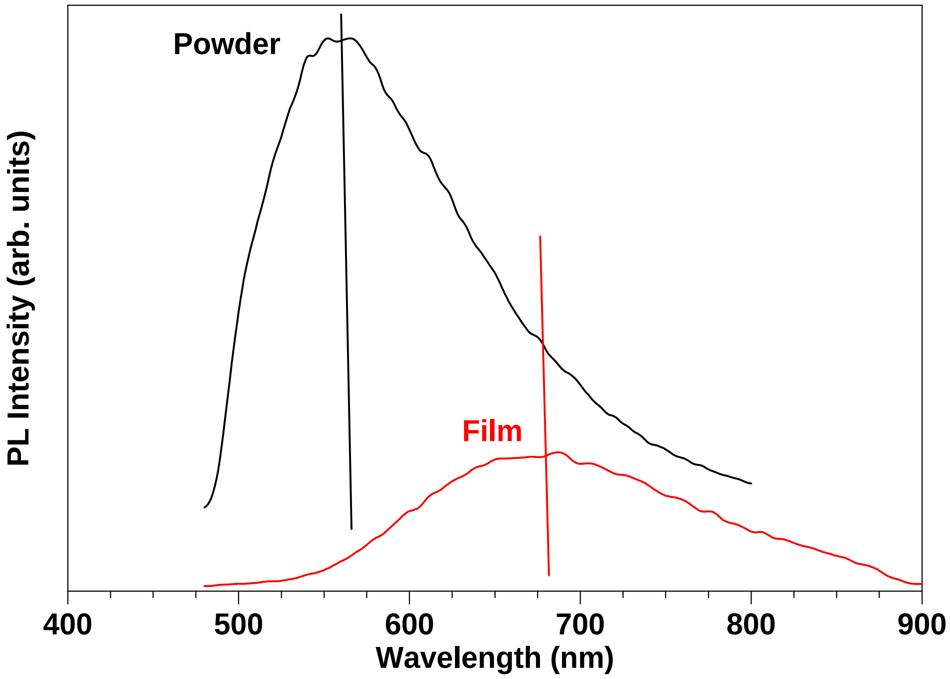

Figure 7.4. PL spectra of the SiO_2:PbS powder sample and thin film both excited at 458 nm.

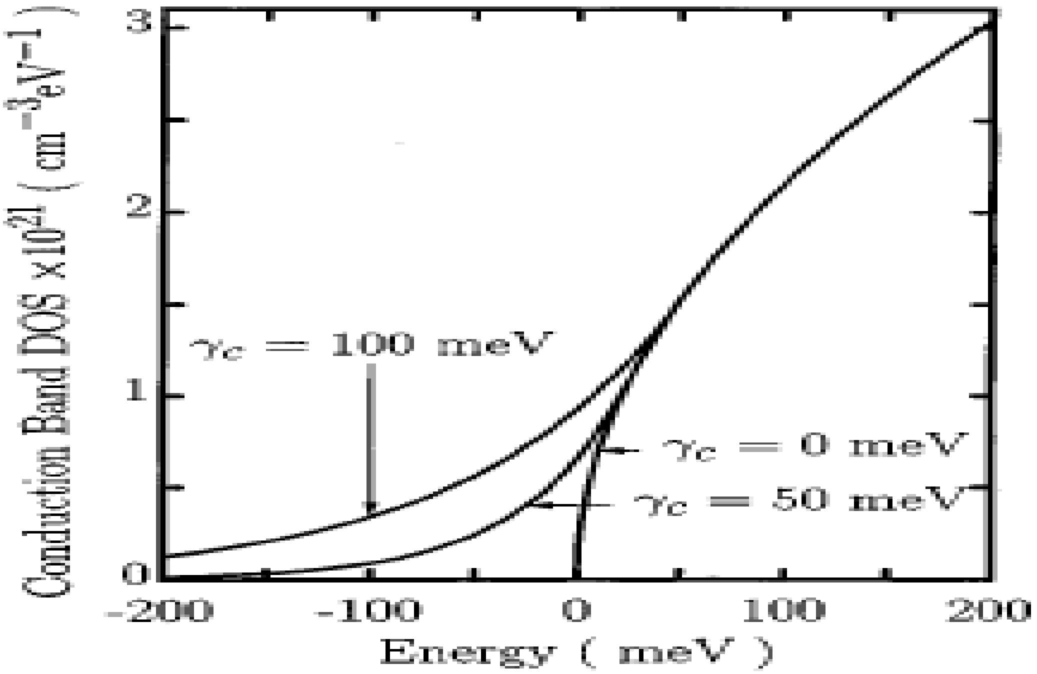

Figure 7.5. The conduction-band distribution of states (DOS) function $N_c(E)$ showing the distribution of conduction-band tail states in the film [11].

In contrast, an amorphous semiconductor has a tail in the absorption spectrum encroaching into the empty band gap as shown in figure 7.5. Since the band gap of the semiconductor in the nano-scale regime is tunable, the decrease in the band gap of a film made from nanoparticles could be attributed to this band tail effect caused by the impurities in the film. Hodes et al [6] have reported that the nature of the localization of electrons and holes in a confined space which results in quantum size effect demands electronic isolation between particles. They further reported that when individual particles are in electrical contact, they might lose their quantization effect. The red-shift of the band gap energy of the film is also believed to originate from the residual stress in the film due to lattice distortion [15].

Figure 7.6 presents the PL emission spectra of the thin films grown on Si (100) at different substrate temperatures ranging from room temperature to 300 °C. The PL intensity increased relatively with the increase in the substrate temperature. This relative increase of the PL intensity with the substrate temperature suggests the depletion of the grains which plays a major role in increasing defect densities, in other words a reduction in the surface/volume ratio. Similar behavior was observed by Mckittrick et al [16], in their study of characterization of photoluminescent $(Y_{1-x}Eu_x)_2O_3$ thin films prepared by metallorganic chemical vapour deposition. They measured an increase in the PL intensity with an increase in substrate temperature (500 ^oC, 600 ^oC and 700 ^oC) of the films grown on sapphire substrates. They ascribed the increase in the PL intensity with increasing deposition temperature to an increase in the volume fraction of cubic Y_2O_3. They further pointed out that the emission intensity increase can be attributed to both grain growth (minimizing grain-boundary area) and a reduction of disorder around the Eu^{3+} in the lattice.

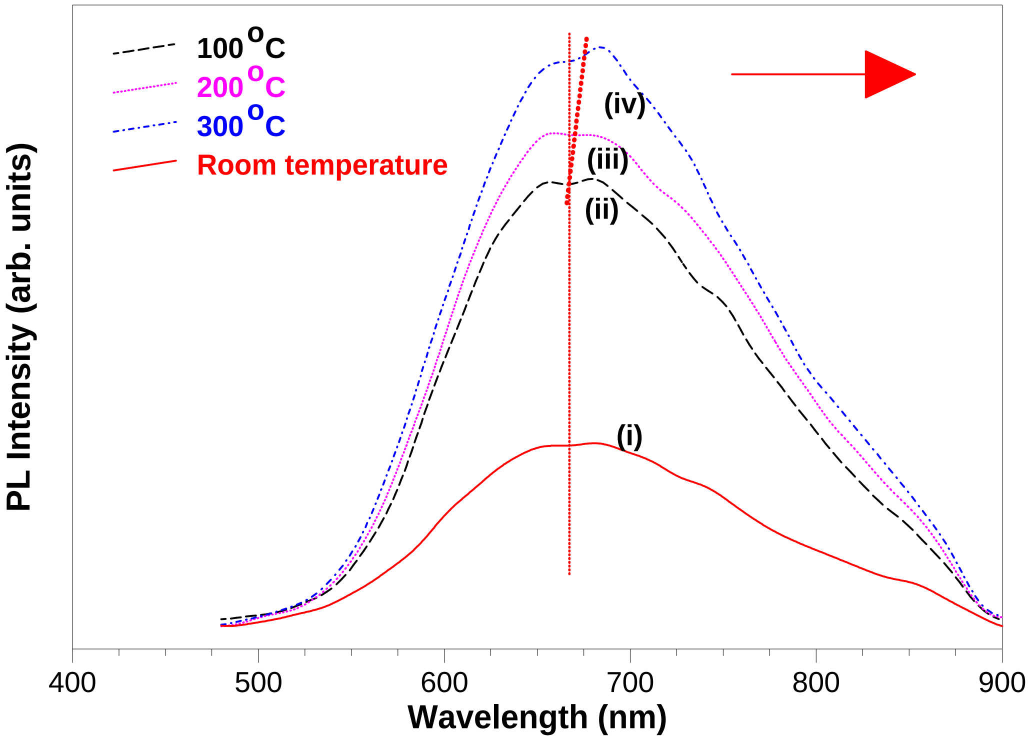

Figure 7.6. PL spectra of the thin films grown at different substrate temperatures; (i) room temperature, (ii) 100 °C, (iii) 200 °C and (iv) 300 °C.

Sagar et al [15] also observed an increase in the PL of the sol-gel derived ZnO films as a function of substrate temperature. They reported that the photoluminescence is sensitive to the quality of crystal structure and to the presence of defects. A slight shift of the PL spectra towards longer wavelength (red) with increase in the substrate temperature was observed. The red-shift proves the grain growth [17] of the agglomerated particles with increase in deposition temperature as observed in the SEM images of these films. It also suggests that as the temperature increases, the connectivity between the particles also increases due to sintering of small particles. A further red-shift in PL emission wavelength upon heating due to the crystallite size growth represents the typical size effect. A 10 nm red-shift of PL emission of an annealed sample compared to that of the unannealed sample was observed by Wang et al [13], in the study of SiO_2:CdS PLD thin films. The shift was also ascribed to the growth of the crystallite size.

The effect of post deposition annealing treatment is illustrated in figure 7.7. A film deposited at a substrate temperature of 400 °C, was later annealed in air at 400 °C for two hours. Figure 7.7 shows that post deposition annealing increased the PL intensity by ~ 50%. This may be due to the decrease of defects in the film and the increase in crystallite size as a result of heating [16].

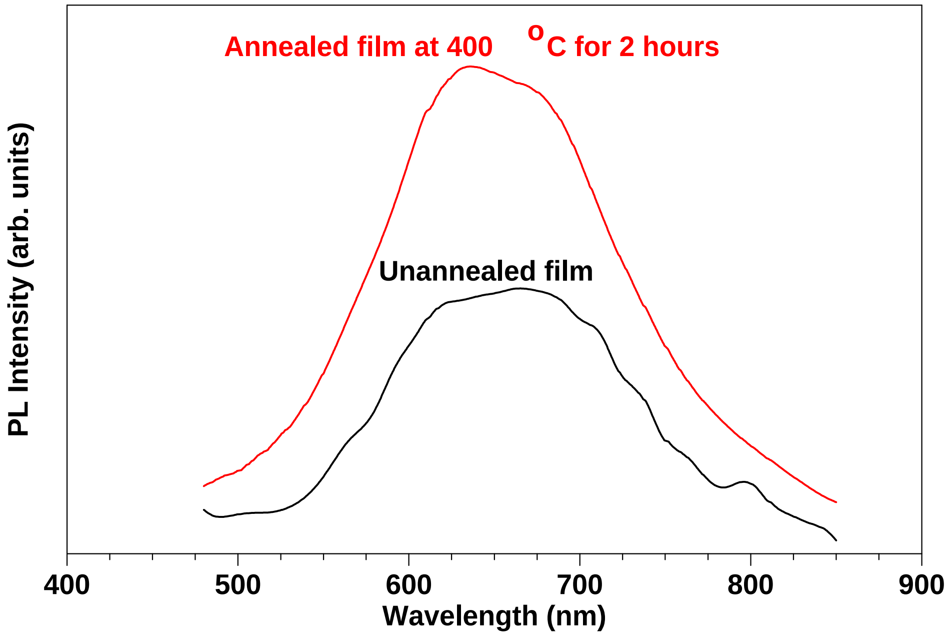

Figure 7.7. PL spectra of annealed and unannealed films.

7.4. Conclusion

The effect of the substrate temperature on the grain growth and PL intensity has been examined in SiO_2:PbS thin films deposited on Si(100) by the PLD technique. The SEM data showed the agglomeration of spherical nanoparticles whose diameters increased with deposition temperature. The red shifting of the emission wavelengths of the films from those of the powders was observed in the PL spectra. The PL intensity increased with increase in the substrate temperatures.

References

[1] D. Riabinina, F. Rosei, M. Chaker, *Journal of Engineering Nanoscience*, **1** (1) (2005) 83.

[2] V. Sukhovatkin, S. Musikhin, I. Gorelikov, S. Cauchi, L. Bakueva, E. Kumacheva and E. H. Sargent, *Optics Letters*, **30** (2) (2005) 171.

[3] J. Schubert, M.J. Schöning, Yu G. Mourzina, A.V. Legin, Yu G. Vlasov, W. Zander, H Lüth., *Sensors and Actuators*, B: Chemical Volume **76** (1-3) (2001) 327.

[4] Ping Yang, Chun Feng Song, Meng Kai Lu, Xin Yin, Guang Jun Zhou, Dong Xu, Duo Rong Yuan, *Chemical Physics Letters,* **345** (2001) 429.

[5] A. Martucci, J. Fick, Serge-Emile LeBlanc, M. LoCascio, A. Hache, *Journal of Non-Crystalline Solids*, **345 & 346** (2004) 639.

[6] G. Hodes, A. Albu-Yaron, F. Decker, P. Motisuke, *Physica Review B*, **36** (8) (1987-I) 36.

[7] K.K. Nanda, F.E. Kruis, H. Fissan, *Journal of Applied Physics*, **91** (4) (2002) 2315.

[8] T. Inokuma, Y. Kurata, and S. Hasegawa, *J. Lumin.,* **80** (1999) 247.

[9] J.H. Warner, A.R. Watt, M.J. Fernee, N.R. Heckenberg, H. Rubinsztein-Dunlop, *Nanotechnology*, **16** (2005) 482.

[10] H.Z. Wu, D.J. Qiu, Y.J. Cai, X.L. Xu, N.B. Chen, *J. Crysta. Growth*, **245** (2002) 51.

[11] Stephen K. O'Leary, S.R. Johnson, P.K. Lim, *J. Appl. Phys.,* **82** (7) (1997) 3334.

[12] J. Singh, *Journal of Materials Science: Materials in Electronics*, **14** (2003)172.

[13] H. Wang, Y. Zhu, P.P. Ong, *J. Crysta. Growth*, **220** (2000) 554.

[14] X.L. Tong, D.S. Jiang, Y. Li, Z.M. Liu, M.Z. Luo, *Phys. Stat. Sol.* (a) **2003** (8) (2006) 1992.

[15] P. Sagar, P.K. Shishodia, R.M. Mehra, H. Okada, A. Wakahara, A. Yoshida, *J Lumin*, **126** (2007) 804.

[16] J. Mckittrick, C.F. Bacalski, G.A. Hirata, K.M. Hubbard, S.G. Pattillo, K.V. Salazar, M. Trkula, *J. Am. Ceram. Soc.*, **83** (2000) 1241.

[17] Y. Zhu, Z.X. Shen, Y.V. Lim, H. Zang, Y. Liu, A.T.S. Wee, *Journal of Physics: Conference Series*, **28** (2006)130.

CHAPTER 8

PbS CONCENTRATION QUENCHING IN SiO_2 MATRIX AND ENHANCED PHOTOLUMINESCENCE BY AN ENERGY TRANSFER FROM ZnO NANOPARTICLES TO PbS NANOPARTICLES

8.1. Introduction

Enhanced luminescence of nanoparticulate phosphors induced by an energy transfer from nanoparticle to another nanoparticle encapsulated in a SiO_2 matrix has been demonstrated for potential application in light emitting devices. Bang [1], Nogami et al [2] and Hayakawa et al [3] reported energy transfer between ZnO , Eu^{3+} and CdS, and SnO_2 nanoparticles, respectively, embedded in calcined SiO_2 gels. The findings stimulated the interest of many researchers worldwide. This chapter reports on the photoluminescence properties of different PbS concentrations in the SiO_2 matrix. Furthermore, it investigates the non-radiative energy transfer from the donor (ZnO) to the acceptor (PbS) both embedded in SiO_2 matrix.

8.2. Experimental

The solution of SiO_2:PbS was prepared by a sol-gel process as discussed in the previous chapters. In this study, ZnO nanoparticles were prepared by dissolving 0.46 g of zinc acetate [$Zn(CH_3COO)_2$] in 30 mL of ethanol (EtOH) by vigorous stirring at 80 ^{o}C for 1 hour. The resulting transparent solution was cooled in ice water. A 0.22 g of NaOH was dissolved in 10 mL of EtOH in an ultrasonic bath and was also cooled in ice water. The NaOH solution was then added drop-wisely to the transparent solution using vigorous stirring in ice water. Oxides are formed during hydrolysis and condensation of the dissolved species according to the following overall reaction:

$$Zn(CH_3COO)_2 + 2NaOH \rightarrow ZnO + 2CH_3COO^- + 2Na^+ + H_2O(\uparrow)$$

A flow diagram for the preparation of ZnO nanoparticles is shown in figure 8.1.

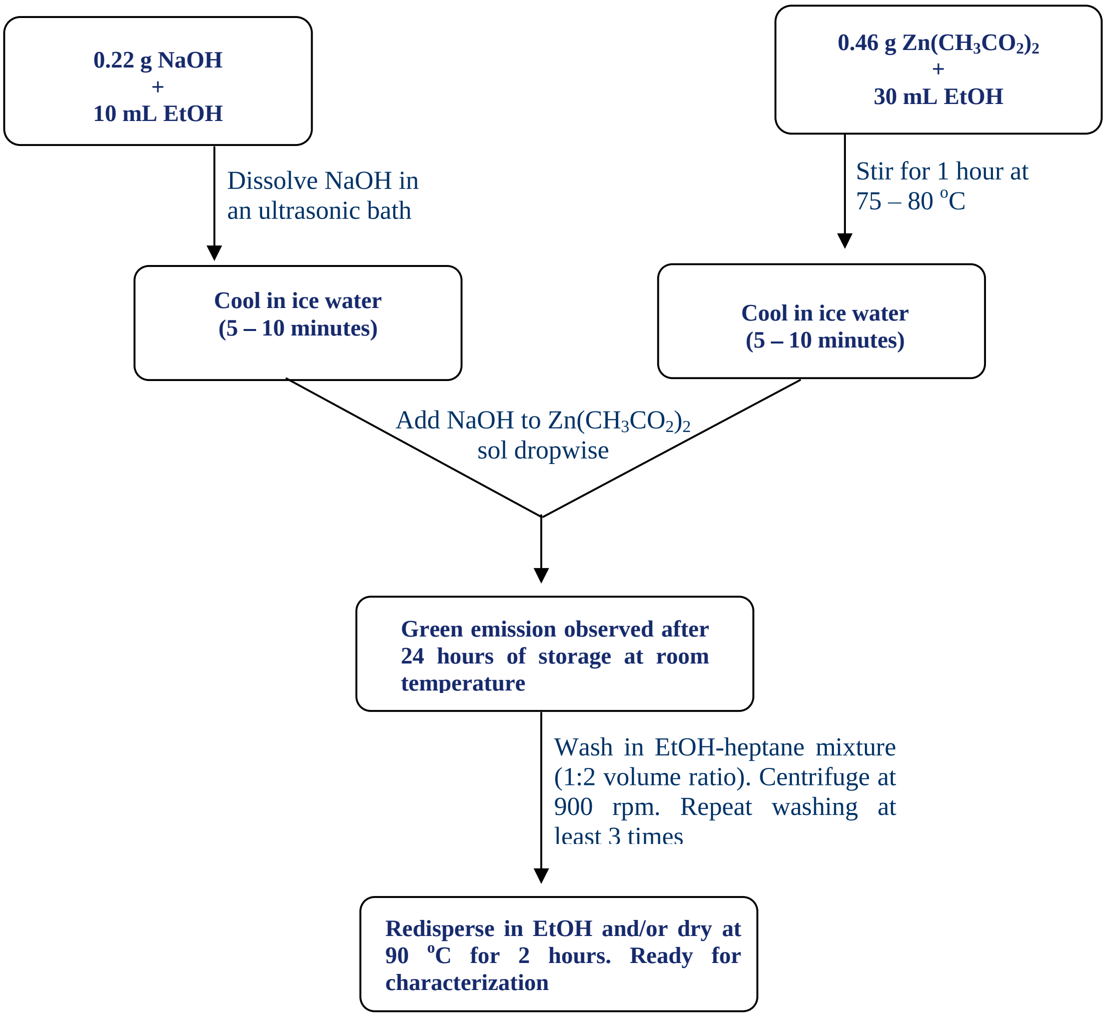

Figure 8.1. A flow diagram for the sol-gel preparation of ZnO nanoparticles.

The unwanted CH_3COO^- and Na^+ ions were removed by washing the gels repeatedly in a mixture of ethanol and heptane (volume ratio of 1:2). The ZnO nanoparticles were either precipitated by centrifuging and dried at 90 ^{o}C for 2 hours or suspended in EtOH. The resulting ZnO nanoparticles suspended in EtOH were added to SiO_2:PbS solution and stirred for 1 hour to form ZnO:SiO_2:PbS nanocomposite. The solution was then transferred to petri dishes and stored at room temperature to dry. The dried gels were crushed into powders and annealed at 200 ^{o}C in air for 2 hours.

8.3. Results and discussion

Figures 8.2 and 8.3 show the SEM photographs of calcined ZnO:SiO_2:PbS and ZnO nanoparticle powders, respectively. The ZnO:SiO_2:PbS photograph, figure 8.2, shows that most of the particles were multi-faceted and micron sized due to agglomerated composite-particles. In figure 8.3, agglomerated particles with different shapes and sizes are shown. Nano-sized particles on the surface of the bigger agglomerated particles are apparent. There is no obvious difference between the SEM photographs of ZnO:SiO_2:PbS and SiO_2:PbS, (figure 4.7). The chemical composition of the ZnO:SiO_2:PbS nanocomposite is shown in figure 8.4. The spectrum confirms the presence of Zn in the composite and shows the low peak intensities of the elements Pb, S and Zn in the powder sample and this is ascribed to their relatively low concentrations. In this nanocomposite, SiO_2 is a host, PbS an activator and ZnO is an embedded sensitizer.

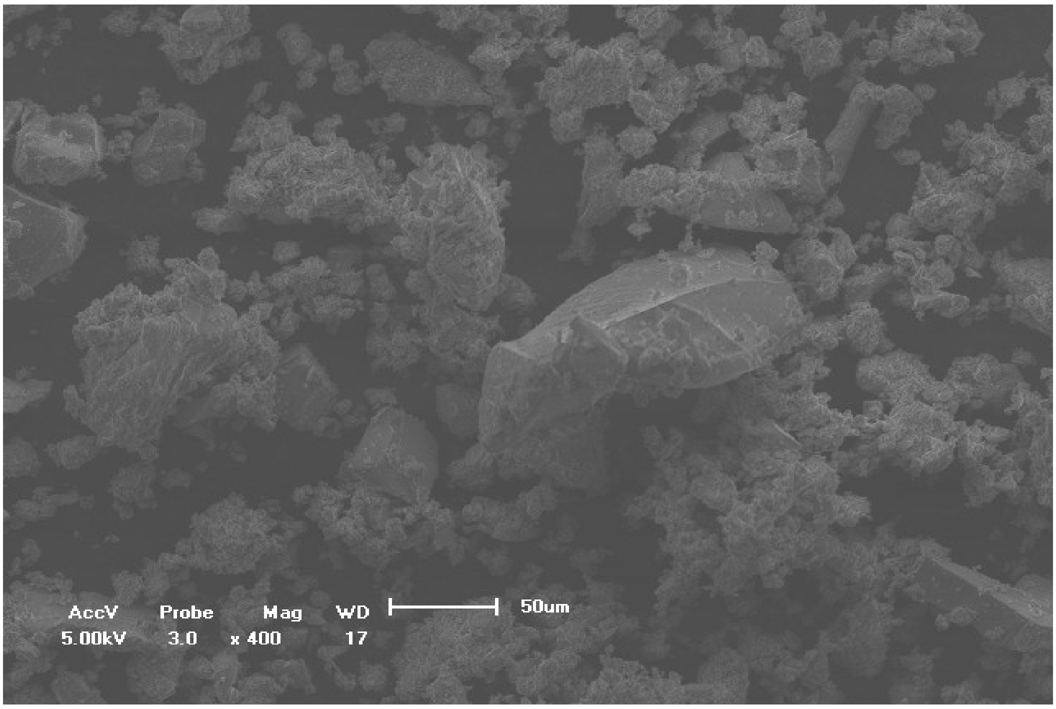

Figure 8.2. The SEM photograph of the annealed ZnO:SiO_2:PbS powder phosphor.

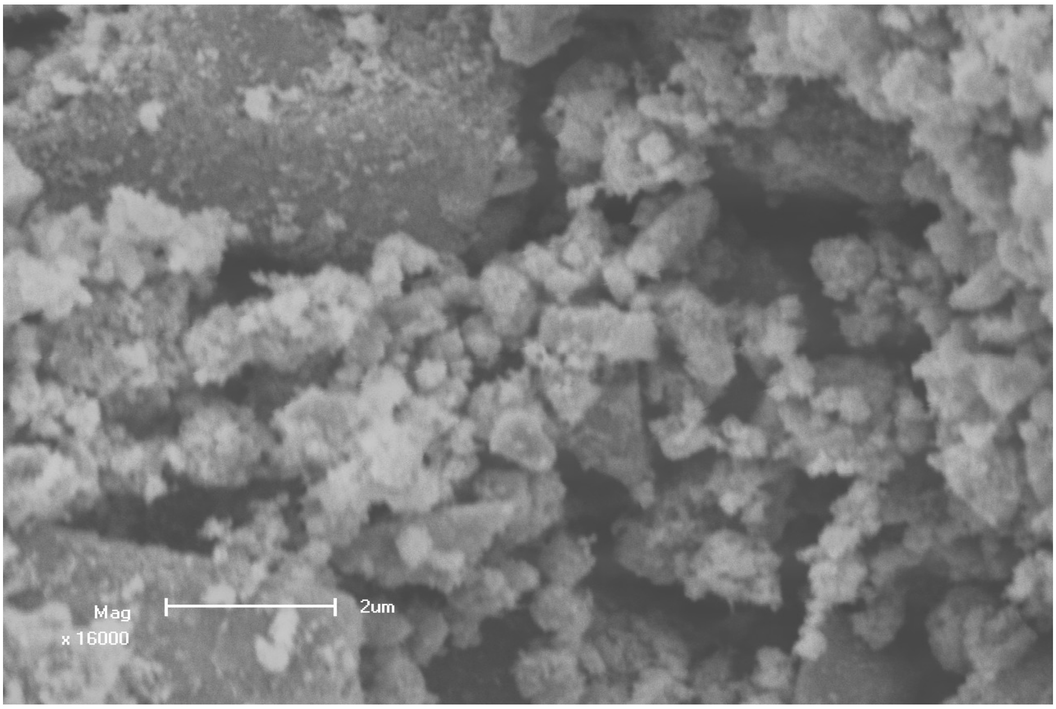

Figure 8.3. The SEM photograph of dried and powdered ZnO nanoparticles.

Figure 8.5 shows the photoluminescence (PL) emission spectra of SiO_2:PbS nanoparticle phosphors with different concentrations of PbS varied from 0.134 to 0.5 mol%. Spectra (1), (2) and (3) show the PL intensities of 0.134, 0.21 and 0.5 mol% PbS, respectively. With an increase in PbS concentration, the shapes and positions of the emission peaks show no obvious changes. The PL emission intensity of SiO_2:PbS phosphor increases with the increase in the mole concentration of PbS and reached the maximum at the concentration of 0.21mol%. Further increase in the PbS concentration (beyond 0.21mol%) resulted in the decrease in the PL intensity. This suggests that the emission center of PbS is quenched at high concentrations. The decrease in PL intensity is associated with a decrease in the transparence of the doped samples [4]. When the mole concentration of PbS is >0.21%, the doped sample is almost opaque. Similar results on the concentration quenching of PbS in SiO_2:PbS phosphor were reported by Yang et al [4]. Jiang et al [5] reported the concentration quenching of Eu^{2+} in $Ca_2MgSi_2O_7:Eu^{2+}$ phosphor. In their study, they observed an increase in the PL emission intensity with an increase in the concentration of Eu^{2+} until it goes beyond about 2.5%, whereby the emission intensity began to decrease. Similarly, Wang et al [6] also reported on the concentration quenching of Eu^{2+} in $4SrO \cdot 7Al_2O_3:Eu^{2+}$ phosphor. The concentration at which the emission intensity begins to decrease is termed critical concentration.

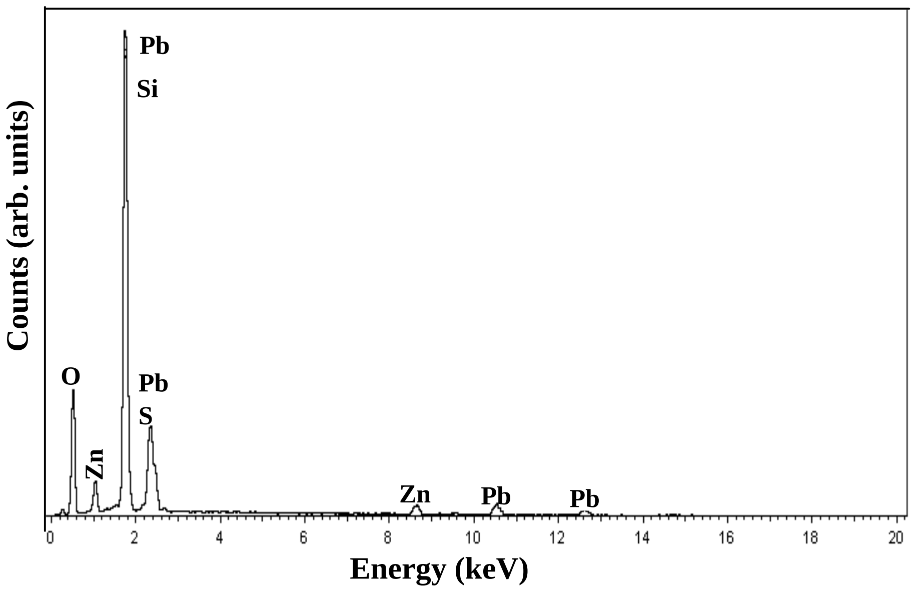

Figure 8.4. EDS spectrum for chemical composition of the as prepared ZnO:SiO_2:PbS powder sample.

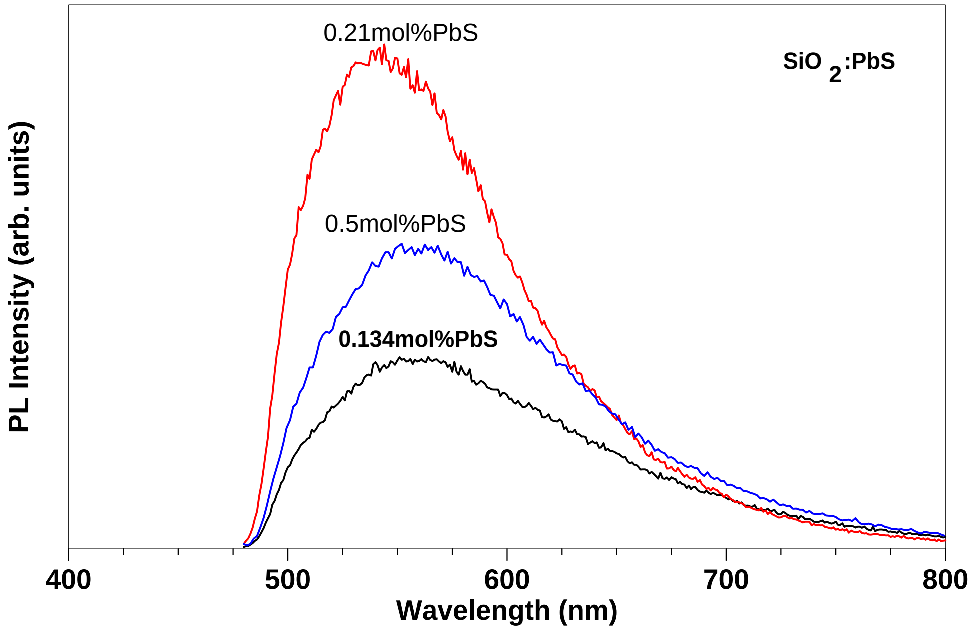

Figure 8.5. PL emission spectra of the different molar concentrations of PbS doped silica powder samples.

SiO_2:PbS shows a weak emission peak at ~ 560 nm, and due to energy transfer from ZnO to PbS, the emission from SiO_2:PbS is greatly enhanced by the embedded ZnO nanoparticles. Figure 8.6 compares the PL emission spectra of SiO_2:PbS powder phosphors with and without ZnO nanoparticles, both calcined in air at 200 ^oC for 2 hours. The emission peak of ZnO:SiO_2:PbS is being ~5 times more intense than the SiO_2:PbS sample. The spectra show no obvious change in peak positions and shapes, and this suggests that the measured PL emission in both cases is from the SiO_2:PbS. Bang et al [7] reported that the green emission from ZnO nanoparticles was completely suppressed when embedded in SiO_2 doped with Eu^{3+} ex situ sol-gel process. They attributed this to the non-radiative energy transfer from the ZnO nanoparticles to the Eu^{3+} ions in SiO_2 matrix, and we believe that the same happened in this study.

Energy transfer rates are known to be proportional to the spectral overlap and interactions between donor and acceptor sites of species. The strength of interaction is determined by the intensity of an optical transition and it is larger for allowed (i.e. broad-band) compared to forbidden (i.e. narrow line) transitions [7]. So we believe that the energy transfer from ZnO nanoparticles embedded in SiO_2:PbS occurs from an allowed broad-band absorption for the ZnO donor to an allowed absorbing acceptor (PbS). Bang et al further reported that energy transfer rates are larger for band-to-band processes due to the large spectral overlap. Energy transfer between semiconductor nanoparticles (ZnS or CdS) and Eu^{3+} ions in sol-gel derived thin films was also reported by Ehrhart et al [8].

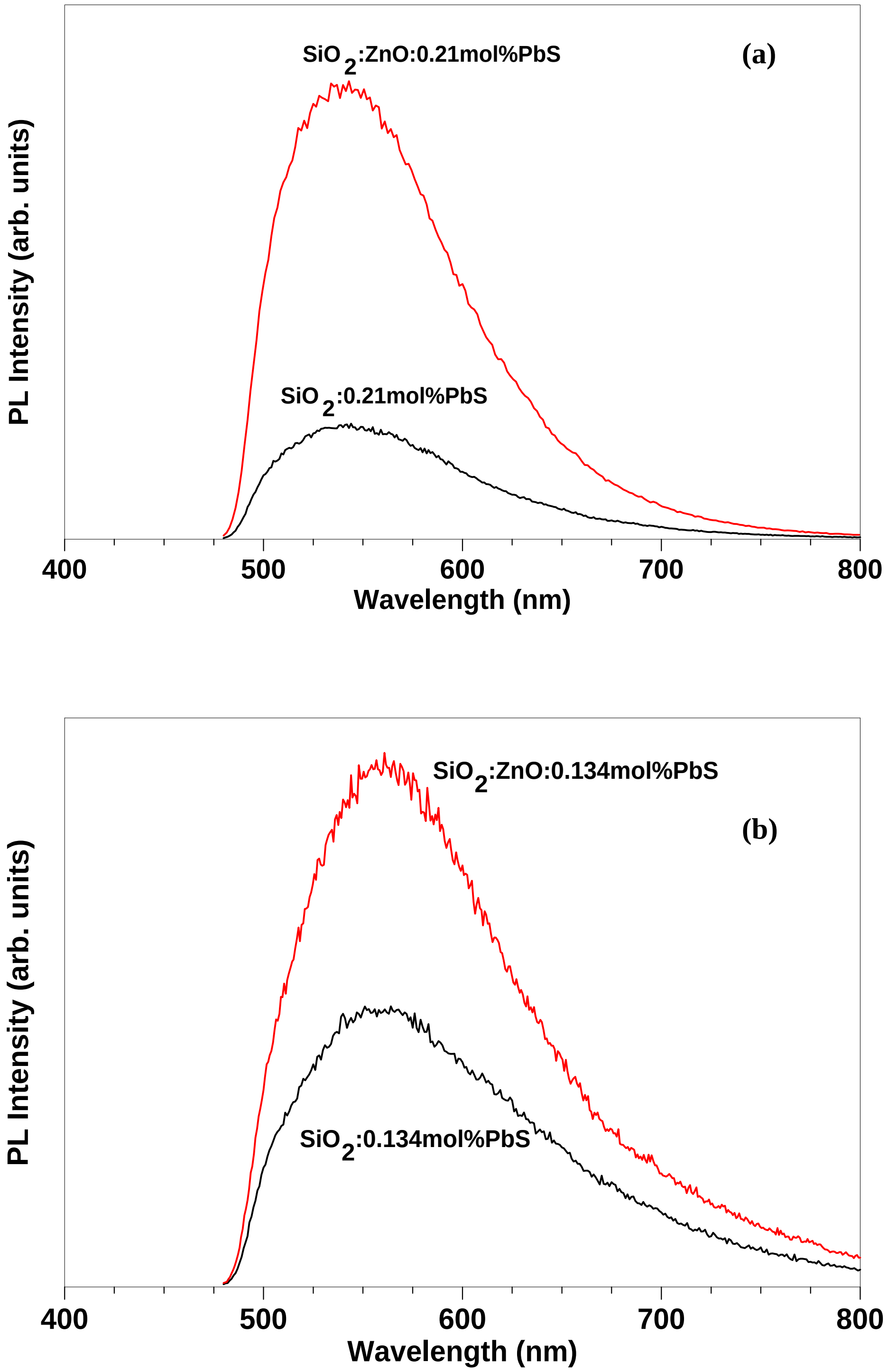

Figure 8.6. PL emission spectra of (a) SiO_2:0.21mol%PbS and ZnO:SiO_2:0.21mol%PbS powder phosphors, and (b) SiO_2:0.134mol%PbS and ZnO:SiO_2:0.134mol%PbS powder phosphors.

Figure 8.7 shows the normalized PL emission peaks of ZnO nanoparticles, SiO_2:PbS and ZnO:SiO_2:PbS. A broad ZnO PL emission peak is observed to be at ~580 nm and a broad PL emission peaking at ~550 nm from SiO_2:PbS was also observed. From this figure, it is apparent that the positions and shapes of the SiO_2:PbS and ZnO:SiO_2:PbS spectra are the same, which proves the fact that the energy was transferred from ZnO nanoparticles to PbS.

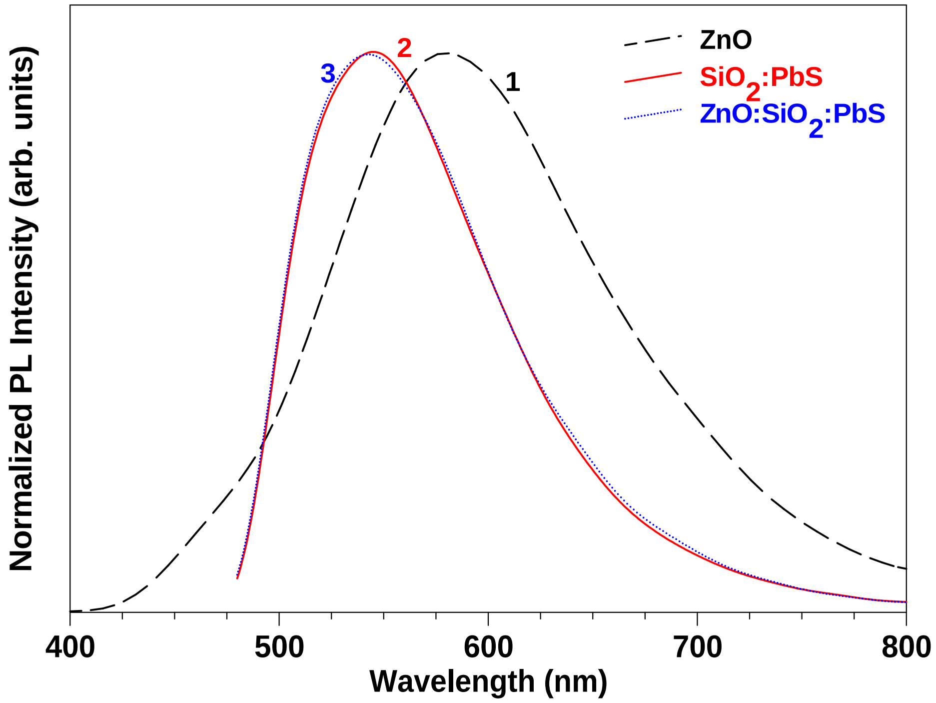

Figure 8.7. Normalized PL emission intensities of (1) ZnO dried powder, (2) SiO_2:PbS and (3) ZnO:SiO_2:PbS powder samples.

Figure 8.8 shows the PL emission peaks of ZnO:SiO_2:PbS for different concentrations of PbS. The increase in PbS concentration resulted in an increase in PL intensity. Due to concentration quenching of embedded PbS nanoparticles, the further increase in PbS concentration (>0.21mol%) resulted in a considerable decrease in the PL intensity of the ZnO:SiO_2:PbS. Energy transfer from ZnO (donor) to PbS (acceptor) will dominate over emission from ZnO when $R < R_c$, where R is the distance between donor ZnO nanoparticle and an acceptor PbS nanoparticle, and R_c is the critical distance at which ZnO emission dominates over energy transfer [7].

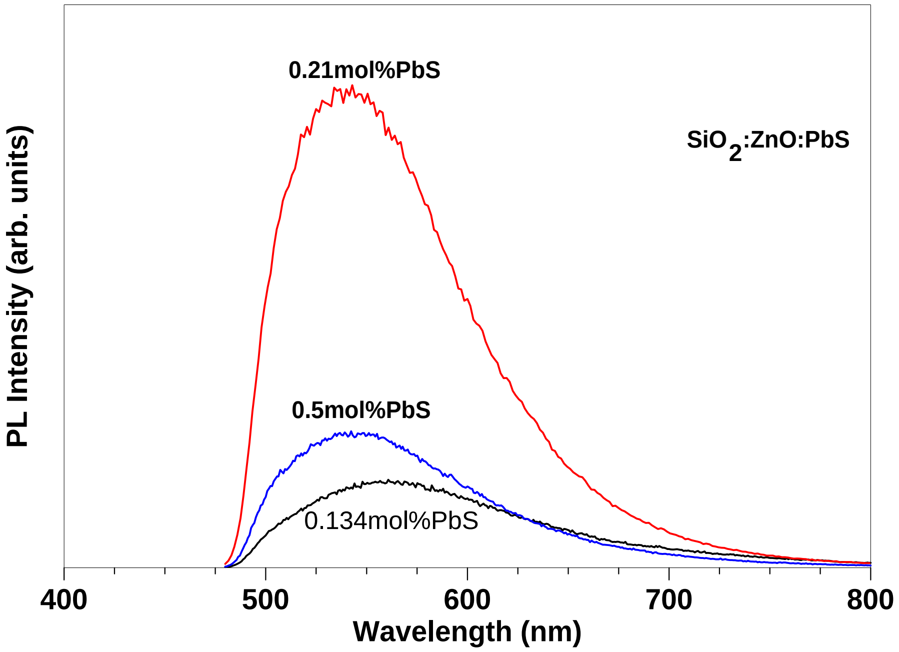

Figure 8.8. PL emission spectra from different molar concentrations of PbS doped SiO_2 powder samples with ZnO nanoparticles and calcined in air at 200 °C for 2 hours.

A possible energy transfer mechanism that could lead to enhanced luminescence is suggested in figure 8.9. Defects states in the band-gap of ZnO are filled by band-gap absorption and relaxation to the defects states on ZnO. Subsequently the energy is transferred resonantly or by phonon-mediated processes to the P_e and S_e states of PbS via internal photoemission from ZnO and complete photocapture by PbS, resulting in enhanced PbS luminescence. Energy transfer from ZnO nanoparticles was observed by Bang et al [7] in their study of enhanced luminescence of $SiO_2:Eu^{3+}$ by energy transfer from ZnO nanoparticles. Similar results on the energy transfer from ZnO nanoparticles to Eu^{3+} and Ce^{3+} ions in SiO_2 matrix were also reported by Ntwaeaborwa et al [9,10]. Kim et al [11] also reported on the energy transfer among three luminescent centers in full-color emitting $ZnGa_2O_4:Mn^{2+},Cr^{3+}$ phosphors. In their study, they observed a strongest energy transfer to be from Ga-O (blue) to Cr^{3+} (red), second strongest to be Ga-O (blue) to Mn^{2+} (green) and the weakest to be from Mn^{2+} (green) to Cr^{3+} (red). They attributed this phenomenon to the spectral overlap between the energy donors (Ga-O) and the energy acceptors of Mn^{2+} and Cr^{3+} and the absorption cross-section of the energy acceptors, and the decay time of the energy donor.

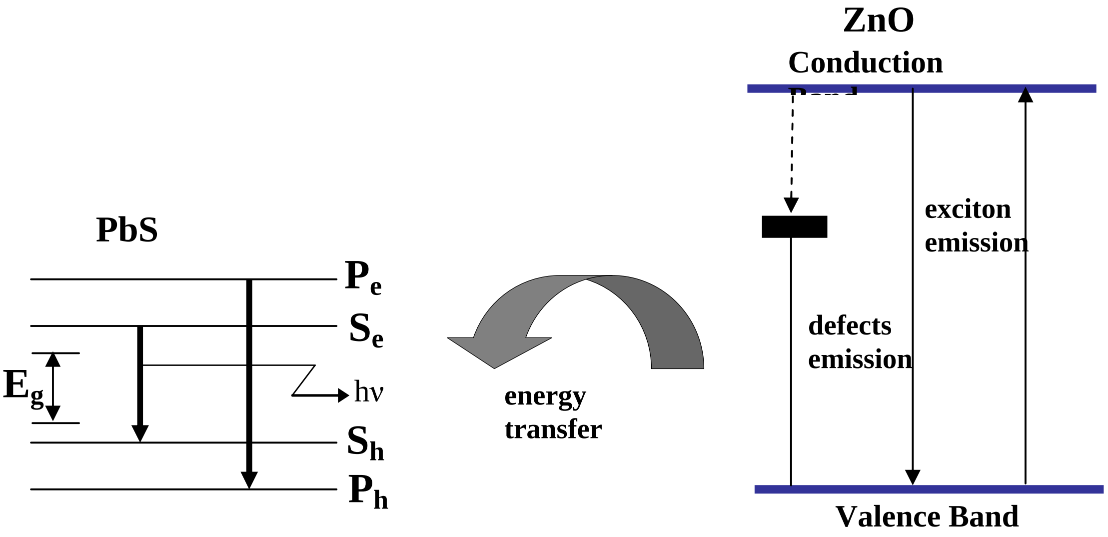

Figure 8.9. Possible mechanism for energy capture by ZnO nanoparticle and transfer to SiO_2:PbS for enhanced luminescence.

However, a broad emission peak at ~ 520 nm associated with transitions in Pb^{2+} ions in either ZnS:Pb^{2+} [12,13] or BaFBr:Pb^{2+} [14] matrix was observed. Hence, there is a possibility that complex Pb-glass may have formed during the preparation of our samples, and the observed emission from either SiO_2:PbS or ZnO:SiO_2:PbS could be associated with the transitions in Pb^{+} ions. However, further investigations are needed in order to fully understand the whole luminescent mechanism.

8.4. Conclusion

The increase in the PbS concentration resulted in a decrease in PL emission intensity due to concentration quenching. The critical quenching concentration of PbS in SiO_2:PbS phosphor is determined as 0.21mol%. ZnO nanoparticles were successfully incorporated into the SiO_2:PbS nanocomposite and the enhancement in the PL intensity due to the energy transfer from ZnO nanoparticles to PbS nanoparticles was observed.

References

[1] J. Bang, Effects of excitation density and energy transfer on cathodoluminescence from powder phosphors with and without embedded nanoparticles PhD Dissertation, University of Florida, USA (2004

[2] M. Nogami, T. Enomoto and T. Hayakawa, *J. Lumin*., **97** (2002) 147.

[3] T. Hayakawa, T. Selvan and M. Nogami, *J. Sol-Gel Sci. Technol*., **19** (2000) 779.

[4] P. Yang, C.F. Song, M.K. Lu, X. Yin, G.J. Zhou, D.R. Yuan, *Chemical Physics Letters*, **345**, (2001) 429.

[5] L. Jiang, C. Chang, D. Mao, C. Feng, *Materials Science and Engineering,* B ***103***, (2003) 271.

[6] D. Wang, Y. Li, Q. Yin, M. Wang, *Journal of Electrochemical Society*, **152** (2005) H15.

[7] J. Bang, H. Yang, P. Holloway, *Journal of Chemical Physics*, **123** (2005) 1.

[8] G. Ehrhart, B. Capoen, O. Robbe, F. Beclin, Ph. Boy, S. Turrell, M. Bouazaoui, *Optical Materials*, in press.

[9] O.M. Ntwaeaborwa, H.C. Swart, R.E. Kroon, P.H. Holloway, J.R. Botha, *Journal of Physics and Chemistry of Solids*, **67** (2006) 1749.

[10] O.M. Ntwaeaborwa, H.C. Swart, R.E. Kroon, J.R. Botha, J.M. Ngaruiya, P.H. Holloway, in press.

[11] Jong S. Kim, Jin S. Kim, T.W. Kim, H.L. Park, Y.G. Kim, S.K. Chang, S.D. Han, *Solid State Communication*, **131** (2004) 493.

[12] Y. Uehara, *J. Chem. Phys*., **51** (10) (1969) 4385.

[13] A.A. Bol, A. Meijerink, *Phys. Stat. Sol (b)*, **224** (2001) 173.

[14] H.F. Folkerts, A. Dijken, G. Blasse, *J. Phys.: Condens Matter*, **7** (1995) 10049.

CHAPTER 9

SUMMARY AND CONCLUSION

Conclusion

This thesis report on the sol-gel preparation of PbS nanoparticles incorporated in SiO_2 matrix, their cathodoluminescence degradation, photoluminescence properties of SiO_2 surface passivated PbS nanoparticles, pulsed laser deposited SiO_2:PbS thin luminescent films and the energy transfer from ZnO nanoparticles to PbS nanoparticles.

Luminescent polyhedron PbS nanoparticles with sizes ranging from 10 to 50 nm inside the SiO_2 matrix were successfully synthesized. The cubic crystal structure of the PbS particles in the matrix was confirmed by the x-ray diffraction and electron diffraction patterns. Broader XRD peak widths of the PbS nanoparticles due to size effect were observed. Chemical composition analysis confirmed the presence of the PbS in the SiO_2 matrix.

The prolonged electron exposure of SiO_2:PbS resulted in SiO_2 being reduced to $SiO_x(0<x< 2)$ by the desorption of oxygen from the surface during electron bombardment and the surface was left rich in elemental silicon. The rate of degradation of CL intensity decreased with an increase in the oxygen pressure. The decrease in CL intensity was ascribed to the formation of a less efficient SiO_x $(0<x< 2)$ layer on the surface. The reaction on the surface was observed to be a combination of the dissociation of the SiO_2 by the e-beam and the recombination of the dissociated Si with the O_2 in the chamber. A combination of SiO_2, SiO, SiO_x and elemental Si was observed in the degraded powder samples. $PbSO_4$ was also formed on the surface during electron bombardment.

The emission wavelength of PbS nanoparticles was blue-shifted (560 nm) from the bulk PbS emission wavelength (~ 3200 nm). Strong emission peaks of SiO_2 at 450 nm and PbS at 593 nm and 514 nm were differentiated. The photoluminescence emission wavelength was blue-shifted from the cathodoluminescence emission wavelength due sample local heating and different excitation cross sections for the two techniques.

The effect of the substrate temperature on the grain growth and PL intensity in SiO_2:PbS thin films deposited on Si(100) by the PLD technique was investigated. The SEM data showed the agglomeration of spherical nanoparticles whose diameters increased with deposition temperature. The red shifting of the emission wavelengths of the films from those of the powders was observed in the PL spectra. The PL intensity increased with increase of the substrate temperatures.

The increase in the PbS concentration resulted in a decrease in PL emission intensity due to concentration quenching. The critical quenching concentration of PbS in SiO_2:PbS phosphor was determined as 0.21mol%. ZnO nanoparticles were successfully incorporated into the SiO_2:PbS nanocomposite and the enhancement in the PL intensity due to the energy transfer from ZnO nanoparticles to PbS nanoparticles was observed.

Future Work

It is reported that luminescence properties of PbS can be affected by host materials and nanocrystal stoichiometry, depending on the reaction conditions. Similarly sized PbS nanocrystals with different stoichiometries can have dramatically different optical properties. Therefore, further investigations to understand the luminescence properties of this phosphor are very important. It is equally important to investigate the effect of the size and size distribution (narrow and broad), and the shape of a particle on the luminescence properties of the PbS phosphors. Furthermore, it would be interesting to investigate the effect of the different host materials as well as the different methods of synthesis.

To fully understand the red or blue shift of the emission wavelength due to different excitation sources (PL and CL), further investigations are needed. The factors leading to the red shift of the PL emission wavelength of the SiO_2:PbS thin films from that of the powders also need further investigations. The enhancement in the luminescence intensity of the phosphors is very important for their applications and energy transfer from one nanoparticle to another nanoparticle is one way of doing this. So the energy transfer from ZnO nanoparticles to PbS nanoparticles is one aspect that needs to be explored further in future.

Publications

- M.S. Dhlamini, H.C. Swart, J.J. Terblans and C.J. Terblanche, Surface cleaning of a commercially pure Ti, Ti6Al4V and Ti3Al8V6Cr4Zr4Mo alloys by linear heating, Surf. Interface Anal. **38** (2006) 339-342.

- M.S. Dhlamini, H.C. Swart, J.J. Terblans and C.J. Terblanche, A comparative study of the impurity segregation from commercially pure Ti, Ti6Al4V and Ti3Al8V6Cr4Zr4Mo, Materials Science and Engineering B: Solid State Material for Advance Technology, **130** (2006) 210-214.

- Swart H.C., Terblans J.J., Coetsee E., Ntwaeaborwa O.M., Dhlamini M.S. and Holloway P.H., Review on electron stimulated surface chemical reaction (ESSCR) mechanism for phosphor degradation, American J. Vac. Sci. Technol. **A25(4)** (2007) 917 – 921.

- M.S. Dhlamini, J.J. Terblans, O.M. Ntwaeaborwa and H.C. Swart, Synthesis and degradation of PbS nanoparticles embedded in SiO_2, (SiO_2:PbS), Surface Review and Letters, **14(4)** (2007) 697-701.

- M.S. Dhlamini, J.J. Terblans, O.M. Ntwaeaborwa and H.C. Swart, Preparations and luminescent properties of PbS nanoparticle phosphors incorporated in a SiO_2 matrix , Phys. Stat. Sol., (c), **5(2)**, (2008) 598 - 601

- O.M. Ntwaeaborwa, M.S. Dhlamini, R. Harris, J.R. Botha, U. Buttner and H.C. Swart, Characterization of sol-gel SiO_2:Ce,Tb powder and pulsed laser deposited thin film phosphors, Phys. Stat. Sol., (c), **5(2)**, (2008) 602- 605

- J.J. Dolo, H.C. Swart, J.J. Terblans, E. Coetzee, M.S. Dhlamini, O.M. Ntwaeaborwa and B.F. Dejene, Degradation of commercial Gd_2O_2S phosphor, Phys. Stat. Sol., (c), **5(2)**, (2008) 594- 597

- M.S. Dhlamini**,** J.J. Terblans, R.E. Kroon, O.M. Ntwaeaborwa, J.M. Ngaruiya, J.R. Botha and H.C. Swart, Photoluminescence properties of SiO_2 surface passivated PbS nanoparticles, South African Journal of Science, in press.

- M.S. Dhlamini**,** J.J. Terblans, O.M. Ntwaeaborwa, J.M. Ngaruiya, K.T. Hillie, J.R. Botha and H.C. Swart, Photoluminescence properties of powder and pulsed laser deposited PbS nanoparticles in SiO_2, Journal of Luminescence, in press.

- O.M. Ntwaeaborwa, M.S. Dhlamini, J.J. Terblans, H.C. Swart, The effects of phonon-mediated energy transfer from ZnO nanoparticles to SiO2:PbS Book of extended abstracts - 14th International Workshop on Inorganic and Organic Electroluminescence & 2008 International Conference on the Science and Technology of Emissive Displays and Lighting, submitted.

- H.C. Swart, J.J. Terblans, O.M. Ntwaeaborwa, E Coetzee, B.M. Mothudi and M.S. Dhlamini, Photon emission mechanisms of different phosphors, Nucl. Inst. and methods in physics research section B: Beam interactions with materials and atoms, submitted August 2008.

- H.C. Swart, J.J. Terblans, O.M. Ntwaeaborwa, E Coetzee and M.S. Dhlamini, Photon emission mechanisms of different phosphors, 23rd ICACS (International Conference on Atomic Collisions in Solids), Phalaborwa, Limpopo province of South Africa, submitted August 2008.

International Conferences

- Conference on Photo-responsive Materials: Kariega (South Africa) – May 2007
  Preparations and luminescent properties of PbS nanoparticle phosphors
  incorporated in SiO_2 matrix
  M.S. Dhlamini, J.J. Terblans, O.M. Ntwaeaborwa and H.C. Swart

- 14th International Conference on Solid Films and Surfaces, Trinity College, Dublin, Ireland
  Sol-gel synthesis and luminescent properties of nanoparticulate ZrO_2:PbS powder phosphor
  M.S. Dhlamini, O.M. Ntwaeaborwa, J.M. Ngaruiya, J.J. Terblans and H.C. Swart

National Conferences

- 52 nd Conference of South African Institute of Physics – Johannesburg (RSA) – July 2007.
  (1) Photoluminescence properties of SiO_2 surface passivated PbS nanoparticles**.**
  M.S. Dhlamini, J.J. Terblans, O.M. Ntwaeaborwa, H.D. Joubert, J.M. Ngaruiya, J.R. Botha and H.C. Swart

  (2) Luminescence studies of pulsed laser deposited PbS nanoparticles embedded in SiO2
  M.S. Dhlamini, J.J. Terblans, O.M. Ntwaeaborwa, H.D. Joubert, K.T. Hillie, J.M. Ngaruiya, J.R. Botha and H.C. Swart

- 51st Conference of South African Institute of Physics – Western Cape (RSA) – July 2006.
  Synthesis and degradation of the PbS nanoparticle phosphors embedded in SiO2, (SiO2:PbS).
  M.S. Dhlamini, H.C. Swart, J.J. Terblans and O.M. Ntwaeaborwa

- 50th Conference of South African Institute of Physics – Pretoria (RSA) – July 2005
  Surface cleaning of a commercially pure Ti, Ti6Al4V and Ti3Al8V6Cr4Zr4Mo alloys by linear heating
  MS Dhlamini, HC Swart, JJ Terblans and CJ Terblanche

- 49th Conference of South African Institute of Physics – Bloemfontein (RSA) – July 2004
  Oxidation of commercially pure Ti and its effects on the surface temperature of the material
  <u>MS Dhlamini</u>, JJ Terblans, CJ Terblanche and HC Swart

- 48th Conference of South African Institute of Physics – Stellenbosch (RSA) – July 2003
  The effect of oxidation on the surface temperature of pure Ti
  <u>MS Dhlamini</u>, JJ Terblans, CJ Terblanche and HC Swart